TECHNISCHE UNIVERSITÄT WIEN
Vienna | Austria

HEPHY
INSTITUT FÜR HOCHENERGIEPHYSIK

Dissertation

# Image reconstruction for ion computed tomography

Ausgeführt zum Zwecke der Erlangung des akademischen Grades einer Doktorin der technischen Wissenschaften unter der Leitung von

**Ass.Prof. Dipl.-Ing. Dr.techn. Albert Hirtl**
**Univ.Lektor Dipl.-Ing. Dr.techn. Thomas Bergauer**

am
Institut für Hochenergiephysik
der Österreichischen Akademie der Wissenschaften
und am
Atominstitut
der Technischen Universität Wien

eingereicht an der
Technischen Universität Wien
Fakultät für Physik

von
**Dipl.-Ing. Stefanie Kaser BSc.**
[redacted]

Unterschrift Betreuer

Unterschrift Studentin

Wien, am 10. Oktober 2022

*Droit devant soi on ne peut pas aller bien loin.*
Straight ahead you can't go very far.

[Antoine de Saint-Exupéry, Le Petit Prince]

# Kurzfassung

Ionentherapie ist eine verbreitete Methode der Krebsbehandlung, bei welcher tief sitzende maligne Tumore bestrahlt werden. Im Gegensatz zu Röntgenstrahlen erreicht die Energiedeposition von Ionenstrahlen pro Wegstrecke ihr Maximum am Ende der Eindringtiefe in ein Material. Dieses Maximum, welches auch Bragg-Peak genannt wird, erlaubt es, eine hohe Strahlendosis im Tumor zu erzielen, während das umliegende gesunde Gewebe geschont wird. Um den Bestrahlungsplan zu erstellen, muss die Lage des Bragg-Peaks daher genau bekannt sein. Deshalb muss das Bremsvermögen, also die Energiedeposition pro Wegstrecke von Ionen in den bestrahlten Gewebetypen, bereits aus vorangehenden Messungen mit hoher Genauigkeit bestimmt werden. Üblicherweise wird hierfür eine Computertomografie (CT) basierend auf Röntgenstrahlen aufgenommen, welche ein Bild in Hounsfield-Einheiten ergibt. Letztere basieren auf den linearen Absorptionskoeffizienten der durchstrahlen Gewebetypen für Röntgenstrahlen. Um einen Bestrahlungsplan für die Ionentherapie zu erstellen, müssen ebendiese Hounsfield-Einheiten in Bremsvermögen umgewandelt werden, wofür eine Kalibrierkurve verwendet wird. Diese Umwandlung ist jedoch einer der Hauptgründe für Unsicherheiten im Bestrahlungsplan.

Ionen-CT (iCT) bietet hingegen die Möglichkeit, das Bremsvermögen der bestrahlten Materialien direkt zu messen und hat daher das Potential, die Unsicherheiten im Bestrahlungsplan zu reduzieren. Allerdings wird der Pfad von Ionen in Materie durch mehrfache Coulomb-Streuung beeinflusst, weshalb ihre Trajektorie nicht als gerade Linie angenommen werden kann. Wird in der Bildrekonstruktion für den iCT-Scan ein herkömmlicher Algorithmus aus der Röntgenstrahlen-CT ohne Adaption verwendet, so führt das zu verringerter Ortsauflösung und reduzierter Genauigkeit des Bremsvermögens im rekonstruierten dreidimensionalen Bild.

Aus diesem Grund besteht ein möglicher Aufbau für die iCT aus mehreren ortsauflösenden Detektoren (Tracker-Modulen), um Eintritts- und Austrittspunkt sowie -richtung der einzelnen Teilchen des Ionenstrahls in das Objekt (Patient oder Phantom) abzuschätzen. Zudem beinhaltet der Aufbau ein Kalorimeter, um die Energie der Teilchen zu messen. Dieser Aufbau wird um den Patienten oder das Phantom rotiert und Messungen bei unterschiedlichen Winkeln aufgenommen. Die Messung der Tracker-Module wird verwendet, um die Ionenpfade abzuschätzen und diese Abschätzung in der nachfolgenden Bildrekonstruktion zu verwenden. Die beste Approximation von Ionenpfaden ist hierbei durch den "most-likely-path (MLP)" Algorithmus oder einen optimierten kubischen Spline gegeben.

Das Institut für Hochenergiephysik (HEPHY) sowie die Technische Universität Wien (TU Wien) haben einen iCT Demonstrator aus den bereits diskutierten Bestandteilen in Betrieb genommen. Ziel dieser Arbeit war es, einen Workflow für die Bildrekonstruktion für den Demonstrator zu erstellen und diesen mit gemessenen und simulierten Daten zu testen. Zudem sollte dieser Rekonstruktionsablauf durch Verwendung von Phantomen mit klinisch relevanter Größe in Bezug auf Ortsauflösung und Genauigkeit der Bestimmung des Bremsvermögens verbessert werden. Hierfür wurde ein iCT Aufbau in Geant4 Monte Carlo

Simulationen modelliert und die daraus generierten Simulationsdaten als Eingangsdatensatz für die Bildrekonstruktion verwendet. Für diesen Schritt wurde die Anwendbarkeit des CUDA-basierten Röntgen-CT Rekontruktionsframeworks TIGRE für die Ionenbildgebung erstmalig untersucht. Verschiedene Ansätze zur Abschätzung der Ionenpfade wurden hierbei genutzt und die resultierende Genauigkeit verglichen. Zudem werden die notwendigen Rekonstruktionszeiten zur Erstellung eines Bildes analysiert. Letztere stellen einen essenziellen Faktor bei der potenziellen klinischen Anwendung von iCT dar.

Des Weiteren wurden mit dem Demonstrator andere potentielle Bildgebungsmodalitäten mit Ionen untersucht. Hierfür wurden Radiographien, welche auf elastischer und inelastischer Streuung von Ionen mit den Atomkernen des untersuchten Materials beruhen, mit dem System aufgenommen und analysiert.

# Abstract

Ion beam therapy is a well-established method to treat deep-seated tumors in cancer therapy. In contrast to x-rays, the energy deposition of ions in matter shows a characteristic maximum at the end of their range in a material. This maximum in dose deposition, referred to as Bragg-peak, allows for a high dose in the tumorous area while healthy tissue can be spared. For treatment planning, the location of the Bragg peak has to be known with high precision. Therefore, the stopping power of the irradiated materials, i.e. the energy deposition of a particle per unit path length, has to be extracted from prior measurements. Usually, an x-ray CT scan is generated, which results in a 3D image given in Hounsfield units, defined by the linear attenuation coefficients of the materials. For ion beam therapy, these values have to be converted to stopping power values of the materials via a calibration curve. However, this conversion is a main source of range errors in the treatment planning.

Ion computed tomography allows to directly measure the stopping power of a material. Therefore, this imaging modality offers the potential to significantly reduce range errors for treatment planning. However, ions are affected by multiple Coulomb scattering and do not pass through a material in a straight line. Assuming a straight-line path and using conventional reconstruction techniques from x-ray CT without adaption therefore leads to significant limitations in spatial resolution and stopping power accuracy in the reconstructed 3D image.

To address this problem, a potential ion CT apparatus consists of position-resolving detector modules (tracking modules), to measure the entry and exit position and direction of each particle into the object to be imaged (phantom or patient) as well as a calorimeter to measure the particle's residual energy. This setup is rotated around the patient or phantom and measurements are taken at multiple angles. From the tracking measurement, a path estimate inside the object is made for each ion and used in the subsequent reconstruction process. Here, an optimized cubic spline and a most likely path estimate have already been shown to generate the most accurate results.

An ion CT demonstrator consisting of the already addressed elements is operated by the Institute of High Energy Physics (HEPHY) and the Technische Universität Wien (TU Wien). This thesis aimed at establishing a full reconstruction workflow for the demonstrator and testing it with simulated and measured data. Furthermore, this thesis aimed at investigating and improving the reconstruction workflow with phantoms of clinically relevant size regarding spatial resolution and stopping power accuracy. Therefore, an ion CT setup was modelled in Geant4 Monte Carlo simulations and the simulated data were taken as input for the subsequent reconstruction. For the reconstruction itself, possibilities to use the CUDA-based x-ray CT reconstruction framework TIGRE for ion CT were investigated for the first time. Different path estimates were used in the reconstruction in order to compare the accuracy of the reconstruction result as well as the reconstruction time, which is a crucial factor when it comes to clinical application.

Additionally, the demonstrator system was used to investigate other potential ion imaging modalities. Therefore, radiographic images based on elastic and inelastic scattering of ions with the atomic nuclei of the target material were recorded and analysed.

# Danksagungen

Zu Beginn möchte ich meinen Dank der österreichischen Forschungsförderungsgesellschaft aussprechen, welche dieses Projekt (Nr. 875854) finanziert und somit möglich gemacht hat.

Ich möchte mich bei den Betreuern meiner Dissertation, Albert Hirtl und Thomas Bergauer, bedanken. Lieber Albert, danke, dass Du Dir stets Zeit genommen hast, um mir Feedback zu meiner Arbeit zu geben und immer ein offenes Ohr für mich hattest. Lieber Thomas, danke, dass Du mich zu dieser PhD-Stelle motiviert hast, die ich ohne Dein Zutun und ohne Deine Organisation niemals hätte beginnen können. Danke, dass Du mich in Folge bei meiner Arbeit unterstützt hast. Ich bin dankbar, dass ich die Möglichkeit hatte, meine Forschungsresultate bei Seminaren und Konferenzen zu präsentieren, obwohl es durch die Corona-Pandemie leider lange Zeit nicht möglich war, persönlich daran teilzunehmen. Ich möchte mich hierbei vor allem bei Euch beiden bedanken, da Ihr mich dazu ermutigt habt, Konferenzbeiträge einzureichen und diese durch Eure fachliche Kritik verbessert habt.

Ich möchte mich bei dem Institutsleiter des HEPHY, Jochen Schieck, bedanken. Durch meine Anstellung am Institut hatte ich die Möglichkeit, drei Jahre lang von einem exzellenten wissenschaftlichen Umfeld zu profitieren. Vielen Dank an Simone Krüger und Barbara Weber für die organisatorische Unterstützung in den letzten Jahren und die gemeinsamen Treffen der "HEPHY-Frauen". Je voudrais dire un grand merci à Nathalie, qui m'a aidée à améliorer mes connaissances de la belle langue française. Merci d'avoir investi de ton temps pour pratiquer si souvent avec moi. C'était toujours un grand plaisir de discuter avec toi.

Weiters möchte ich mich bei Alexander Burker bedanken, welcher mich bereits bei meiner ersten Projektarbeit in der pCT Gruppe unterstützt hat. Durch Deine herausragenden Programmierkenntnisse und die daraus entstandenen Codebausteine hast Du in vielen Bereichen einen Grundstein für die Arbeit unserer Gruppe gelegt.

Danke, lieber Felix Ulrich-Pur, für Deinen Beitrag zu dieser Arbeit, welcher sich hier nur schwer in ein paar wenigen Worten zusammenfassen lässt. Es war mir eine riesige Freude und Bereicherung, mit Dir im Team zu arbeiten. Ich danke Dir nicht nur für die zahlreichen fachlichen Gespräche, die wir geführt haben, sondern allem voran für Deine Freundschaft.

Ich möchte mich bei den (ehemaligen) Mitarbeitern der Detector Development Gruppe am HEPHY, insbesondere Dominic Blöch, Viktoria Hinger, Peter Paulitsch, Patrick Sieberer und Vera Teufelhart, bedanken, mit welchen ich schon zu Beginn meines Doktorats die Mittagspausen verbracht und dabei zahlreiche interessante Gespräche geführt habe. Weiters gilt mein Dank Christian Irmler und Florian Pitters, welche durch ihr Feedback und ihre Beiträge wesentlich zum Erfolg dieser Arbeit beigetragen haben.

Zudem möchte ich mich bei meinen Bürokollegen Philipp Gaggl, Andreas Gsponer und Simon Waid bedanken. Danke, dass Ihr meinen Arbeitsalltag (und das "darüber hinaus") so sehr bereichert habt. Danke Simon, dass ich mit Dir immer so offen sprechen konnte und Du diese Dissertation durch Deine Kommentare verbessert hast. Danke, Maximilian Babeluk, Kostas Damanakis, Veronika Kraus und Moritz Wiehe für gemeinsame Konferenzen,

Mittagessen und die lustigen Abende, die wir in meiner Zeit am HEPHY verbracht haben.

Ich danke den Studenten, die mich im Laufe meines Doktorats unterstützt haben. Besonders möchte ich mich bei Benjamin Kirchmayer bedanken, welcher durch seine Diplomarbeit auch einen entscheidenden Beitrag zu der Codeerweiterung der TIGRE-Toolbox für Ionenbildgebung geleistet hat.

I would like to express my gratitude towards Wolfgang Birkfellner, Dietmar Georg and Sepideh Hatamikia from the Medical University of Vienna. Thank you for helping me getting started with the TIGRE toolbox and for your valuable contributions to my research. In addition, thank you for supporting and motivating me to present my work at conferences and seminars. Furthermore, I would like to thank Ander Biguri from the University of Cambridge for the time he invested in discussions with me and for his support and feedback to our code contribution to the TIGRE toolbox.

Je voudrais exprimer ma gratitude à Simon Rit, Nils Krah et Feriel Khellaf. Au début de mon doctorat, vous m'avez donné un aperçu détaillé de votre reconstruction d'images. Merci de m'avoir accueillie chez CREATIS et d'avoir facilité mon entrée dans l'imagerie ionique.

Ich möchte Florian Roth danken, mit dem ich immer wieder erstaunt festgestellt habe, dass Satellitenbildgebung und Ionenbildgebung tatsächlich einige Gemeinsamkeiten aufweisen. Danke, dass du mich nun schon so viele Jahre meines Lebens und durch alle Schwierigkeiten begleitest. Ohne Dich wäre mein Weg ein anderer gewesen.

Ich möchte mich bei meinen Freunden für ihre Unterstützung in den vergangenen Jahren bedanken. Insbesondere gilt mein Dank Michael Borkowski, Felicia Brauner und Thomas Knoll, Marlene Bruns und Christoph Schulz, Valentina Bruns und ihrem Energiebündel in Dalmatinerform, Claudia Mayr und Lisa Pertich. Liebe Lisa, besonders bei Dir möchte ich mich für unsere jahrelange innige Freundschaft, die mir immer Halt gegeben hat, und all unsere gemeinsamen Erlebnisse bedanken. Ein großes Dankeschön gilt Katharina Hofbauer, welche mir fast wöchentlich zur Seite (Saite ☺) gestanden ist und mich (Harfen-)musikalisch durch die schönen und schwierigen Phasen eines Doktorats begleitet hat.

Zudem gilt mein Dank meiner Tante, Brigitte Anton, da sie mich immer in meinem Lebensweg bestärkt hat. Ich möchte meiner Schwester, Elisabeth danken - dafür, dass ich mich in schwierigen Zeiten immer auf Dich verlassen kann. Zudem gilt mein Dank meinen Eltern, Helmut und Sabina, die mir mein Studium überhaupt erst ermöglicht haben.

Ich bli-<br>cke<br>voller Dank-<br>barkeit auf die<br>vergangenen Jahre zurück. Ich<br>wurde von großartigen Menschen be-<br>gleitet und unterstützt, von denen<br>ich hoffentlich niemanden in diesen<br>Danksagungen vergessen habe.<br>Ich wünsche Euch allen<br>von Herzen alles Gute<br>für Euren weit-<br>eren Weg.<br>♡

# Contents

# CHAPTER 1

# Introduction

The idea of imaging using ion beams had existed since the 1960ies [1, 2], when radiographic imaging was investigated with a proton source. However, additional challenges appeared with this imaging technique compared to the imaging with x-rays, which has been investigated since the middle of the 1890ies [3]: from the technical perspective, ion imaging requires an accelerator complex (cyclotron or synchrotron) to produce and deliver beams at the desired intensity and energy. Furthermore, from the physical perspective, the interaction types of x-rays and ions with matter are fundamentally different: imaging with x-rays is based on the beam's attenuation in a material, following the well-known Lambert-Beer's law [4, 5]. The beam is hereby expected to pass in a straight line through the patient tissues while its intensity decreases exponentially. For ion imaging, on the other hand, the energy loss of the ions follows the Bethe-Bloch equation [6, 7]. This energy loss is the contrast-generating quantity for images obtained with this modality. However, ions do not pass through the patient tissues in straight lines due to multiple Coulomb scattering [8]. If the specific and non-straight ion paths are not taken into account for the creation process of the image, a blurry ion radiography (iRad) or ion computed tomography (iCT) is the result.

Despite these challenges, ion imaging regained interest in the early 2000s [9, 10] when ion beam therapy became more popular as a form of cancer treatment. For accurate treatment planning, a map of the patient tissues is essential. Precisely, this means that each tissue's stopping power (SP), i.e., the ion's energy loss per unit path in the material, needs to be known with high precision and spatial resolution. Therefore, usually, an x-ray computed tomography (CT) scan is measured beforehand and used to perform the treatment planning. The CT scan is given in Hounsfield units (HUs), which depend on the linear attenuation coefficient of x-rays within a material. These HUs have to be converted to SP values for treatment planning. However, this conversion via a calibration curve [11] is not exact and leads to range uncertainties, resulting in a higher dose for the patient.

To prevent these range errors, the planning CT scan could be directly measured with ions, which would return the SPs of the materials without the need for further conversion. This reveals the potential of ion imaging to improve treatment planning for ion beam therapy [12]. To handle the effects of multiple Coulomb scattering in the resulting image, a single particle tracking setup as described in Schulte et al. [9] can be used.

Following this introduction, the physical and mathematical principles of ion imaging are discussed in chapter 2. The primary aim of this thesis was to develop an image reconstruction workflow for the data obtained with an iCT demonstrator that was built and tested by HEPHY and TU Wien. The software frameworks used are introduced in chapter 3, while chapter 4 describes the iCT demonstrator itself. The experiments with the demonstrator

were conducted at the MedAustron facility in Wiener Neustadt, Austria. The results of a full proton computed tomography (pCT) scan are found in chapter 5. In addition, different radiographic imaging modalities (proton energy loss, scattering and attenuation radiography) were investigated with the demonstrator system in the scope of this thesis. The size of the phantoms that can be imaged with the iCT demonstrator is limited by the size of the upstream and downstream trackers. Therefore, larger phantoms were investigated using Monte Carlo simulations for data generation.

The originally developed workflow for the iCT demonstrator, which uses the open-source tomographic iterative GPU-based reconstruction (TIGRE) toolbox, was refined for these phantom sizes. While this preliminary workflow was based on a straight line (SL) estimate for the ion paths, an extension was written for the TIGRE toolbox in order to incorporate a more sophisticated path estimate in the reconstruction process. Reconstruction results based on this code extension are shown and discussed in chapter 5.

While this thesis mainly focuses on imaging with protons, the principles can also be extended to other ion species and is demonstrated for helium ions in this work. Due to their higher mass compared to protons, these ions are expected to pass in more straight paths through matter. However, they can break up in fragments, which should be filtered from the data set [13].

# CHAPTER 2

# Physical and mathematical background

In this chapter, an introduction to the physical mechanisms contributing to ion imaging and ion beam therapy is given. To understand the physical and mathematical concepts underlying these techniques, the interaction mechanisms of ions and matter are discussed in section 2.1. In section 2.2, ion beam therapy and treatment facilities are introduced as the main driver for implementing ion imaging in the clinic. Section 2.3 discusses the technical and mathematical concepts of imaging with ions.

## 2.1 Interactions of ions and matter

The interaction mechanisms of ions and matter are the underlying principles of ion imaging and ion beam therapy. For ion beam therapy, the energy loss of ions within a tumorous area destroys the DNA of the malignant cancer cells (see section 2.2). For ion imaging, the interactions in the patient tissues define the projection value (based on energy loss) of an ion in the ion computed tomography (iCT) scan, which finally yields the contrast in the resulting image. In addition, the interactions of an ion with detector materials allow measuring the particle's properties, such as its residual energy or its track. In this section, the prominent interactions of ions with matter are discussed. This includes the inelastic Coulomb scattering with atomic electrons of the target (section 2.1.1), elastic Coulomb scattering with the atomic nuclei (section 2.1.2) and inelastic scattering with the atomic nuclei (section 2.1.3).

### 2.1.1 Bethe equation

In a first-order approximation, ions pass through a material on a straight line and continuously lose energy by inelastic Coulomb scattering with the electrons of the target atoms [8]. This process, which liberates the electron from its shell through energy transfer, is displayed for a proton in figure 2.1.1. The proton path remains almost unchanged in this interaction, due to the high proton mass compared to the small electron mass ($m_\mathrm{p} >> m_\mathrm{e}$) [14].

Following the description of Demtröder [14], this process can be understood for ions, in general, using a simplified model: an ion with charge $Z_1 \cdot e$ (where $Z_1$ stands for the charge number and $e$ for the electron charge) enters the electronic shell of a target atom. If the ion's kinetic energy is larger than the binding energy of an electron, it has the potential to remove it from the shell in an inelastic collision. If the ion's kinetic energy is much higher than the binding energy, the fraction of transferred energy relative to the ion's initial energy is small. Hence, the impact on the ion path is negligible, and the electron can be regarded as quasi-free. This is the case for ion imaging, where the target atoms' ionization energies lie

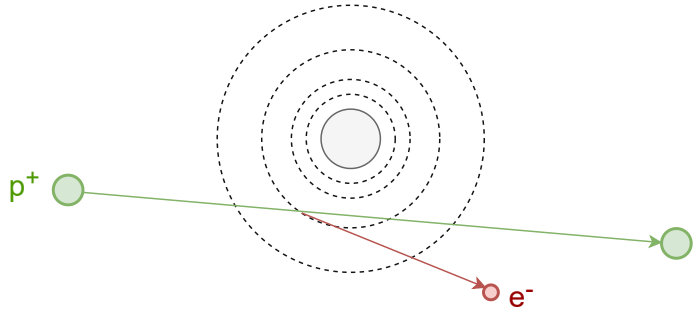


Figure 2.1.1: Inelastic Coulomb scattering of a proton with an electron. Figure based on Newhauser and Zhang [8].

in the order of a few keV (e.g., for water, an ionization energy between 75 eV and 80.8 eV is typically assumed [15]) while the projectile energies lie in the order of MeV (e.g., 200 MeV in Plautz et al. [16]).

The size of the transferred energy is defined by the Coulomb force,

$$\vec{F_C} = \frac{Z_1 e^2}{4\pi\varepsilon_0 r^2}\hat{r}, \tag{2.1.1}$$

which acts between the target atom and the incident ion. The numerator is obtained from the product of the ion charge $Z_1 \cdot e$ and the electron charge $e$, while the denominator is composed of the vacuum permittivity $\epsilon_0$ and the distance between the scattering particles $r$. Using equation (2.1.1), the transferred energy on one electron can be calculated as [14]

$$\Delta\epsilon = \frac{1}{8\pi^2\epsilon_0^2 m_e}\left(\frac{Z_1 e^2}{vb}\right)^2, \tag{2.1.2}$$

where $v$ is the ion's velocity and $b$ refers to the impact parameter. To describe the interaction with all target electrons, integration over all impact parameters, which depend on $v$ and the binding energies of the atomic electrons, would be necessary. This shows the limitations of the simplified model [14].

Bethe [6] and Bloch [7] also considered relativistic energies in calculating an ion's energy loss in a material. The energy loss per unit path, referred to as stopping power (SP) $S$, can be extended by multiple correction terms for better accuracy and can be written as [8]

$$S = -\frac{dE}{dx} = 4\pi\rho N_A r_e^2 mc^2 \frac{Z}{A}\frac{z^2}{\beta^2}\cdot\left[\ln\frac{2mc^2\beta^2\gamma^2}{I^2} - \beta^2 - \frac{\delta}{2} - \frac{C}{Z}\right]. \tag{2.1.3}$$

Here, the target material's properties are described by the material density $\rho$, the mean excitation potential $I$, the atomic number $Z$ and the atomic weight $A$. Other constants in equation (2.1.3) are given by Avogadro's number $N_A$, the classical electron radius $r_e$ and the mass energy of an electron $mc^2$. The projectile is again defined by its charge $z = Z_1 \cdot e$ and its velocity $\beta$. The calculation further includes a shell correction term $\frac{\delta}{2}$ and a density correction term $\frac{C}{Z}$ [8].

According to Berger et al. [17], the classical shell correction term can be written as the sum of all contributions from single shells $\nu$ ($\nu$ = K, L, M,...)

$$C = \sum C_\nu(\theta_\nu, \eta_\nu), \theta = \frac{J_\nu}{\epsilon_\nu}, \eta_\nu = \frac{\beta^2}{\alpha^2 Z_\nu^2}. \tag{2.1.4}$$

$\theta$ refers to the ratio of the shell's ionization energy $J_\nu$ and its Bohr ionization energy $\epsilon_\nu$, while $\eta$ depends on the projectile's velocity $\beta$, the shell's charge number $Z_\nu$ and the fine structure constant $\alpha$ [17]. The shell correction term is especially important for low energies, where the ion's kinetic energy is close to the binding energy of the atomic electrons [8].

In contrast to that, the density correction term $\delta$ becomes more important for ion beams at high energies. The term describes the decreased energy loss of the incident particles due to the dielectric polarization of the medium [18]. As this polarization depends on the ions' velocity, the term can be given in dependence of the variable $X = \log_{10}(\gamma\beta)$ [18] and reads for various ranges of $X$

$$\begin{aligned} \delta(X) &= 0 && \text{if } X < X_0, \\ \delta(X) &= 4.606X + C + a(X_1 - X)^m && \text{if } X_0 \le X < X_1, \\ \delta(X) &= 4.606X + C && \text{if } X \ge X_1. \end{aligned} \tag{2.1.5}$$

The material-dependent constants $C$, $a$ and $m$ can be calculated as [18]

$$\begin{aligned} C &= -2\ln\left(\frac{I}{h\nu_p}\right) - 1 \\ a &= (-C - 4.606X_0)/(X_1 - X_0)^m \\ m &= \frac{X_1 - X_0}{\log(1.649I/h\nu_p) - X_0}, \end{aligned} \tag{2.1.6}$$

with the material's ionization potential $I$, its plasma energy $h\nu_p$ and $X_0$ and $X_1$, which depend on the physical state of the material (condensed or gaseous), the value of $C$ and the incident ion's energy [18].

The SP of the investigated material, $S_\mathrm{m}$, is often divided by the SP of water, $S_\mathrm{w}$, at the same energy, which is called relative stopping power (RSP),

$$\mathrm{RSP} = S_\mathrm{m}(E)/S_\mathrm{w}(E), \tag{2.1.7}$$

as this quantity is almost independent of the ion beam energy over a large range of energies [19]. Dividing the SP by the material's density $\rho$ is referred to as the mass SP.

### 2.1.2 Multiple Coulomb scattering

If the mass of the target atoms' nuclei is large compared to the mass of the incoming ion, almost no kinetic energy is transferred (elastic scattering) [8]. However, the path of the ion is deflected in the collision, as it is displayed for a proton in figure 2.1.2. Multiple of these interactions lead to a zigzag path of the ion though the medium; deviating from the first-order straight-line assumption, which only takes the energy loss with the target electrons into account (section 2.1.1).

This effect is referred to as multiple Coulomb scattering (MCS) and is one of the main challenges in ion imaging (see section 2.3.2). For a mono-energetic parallel proton beam in thin objects, the exit angular distribution (described by the standard deviation $\theta_0$) can be assumed as [20]

$$\theta_0(l, E) = \frac{13.6}{\beta p} z \sqrt{\frac{l}{X_0}} \left[1 + 0.038 \cdot \ln\left(\frac{l}{X_0}\right)\right] \quad \text{for } l << X_0, \tag{2.1.8}$$

which is referred to as Highland formula. Here, $X_0$ refers to the radiation length of the target material and $l$ the proton path length in the material, while $\beta p$ represents the product of the incident particles' velocity and momentum. For thicker objects, an integration of equation (2.1.8) is necessary to consider the energy loss within the object and its influence on the final angular distribution. The radiation length of a material is defined as the depth in which the energy of an electron has decreased to $1/e$ of its original value due to bremsstrahlung and can be approximately estimated using the empirical expression [21]

$$X_0 = \frac{716.4 \cdot A}{Z(Z+1) \cdot \ln(\frac{287}{\sqrt{Z}})}, \tag{2.1.9}$$

with mas number $Z$ and charge number $A$ of the target material. For a material with mass $W_0$, which is composed of $i$ different elements, the combined radiation length can be approximated as [21]

$$W_0/X_0 = \sum_i W_i/X_i. \tag{2.1.10}$$

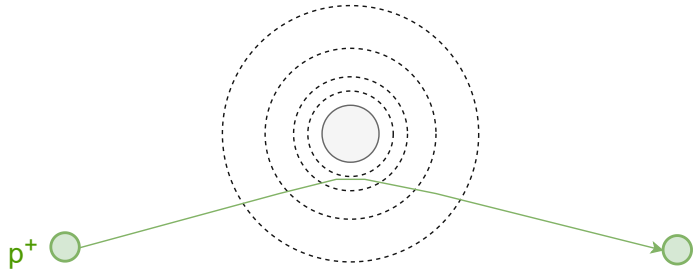


Figure 2.1.2: Elastic scattering of an incident proton with an atomic nucleus. Figure based on Newhauser and Zhang [8].

### 2.1.3 Inelastic nuclear interactions

Due to inelastic collisions with the atomic nuclei of the target, the initial fluence $\phi$ of the primary ion beam with energy $E$ is decreased along the path $l$, depending on the linear inelastic nuclear cross-section $\kappa(x, y, z, E)$ at a position $(x, y, z)$ in the target and can be written as [21, 22]

$$\phi(l) = \phi_0 \cdot \exp\left(-\int_l \kappa(x, y, z, E) dl\right). \tag{2.1.11}$$

As a consequence of such interactions, secondary particles can be released: these particles are either fragments from the target nuclei (secondary protons, neutrons or a recoil nucleus) or fragments of the incident ion itself (for ions heavier than protons). Recoil nuclei deposit their energy locally [21], whereas other fragments [13] may be further transported and even leave the target material.

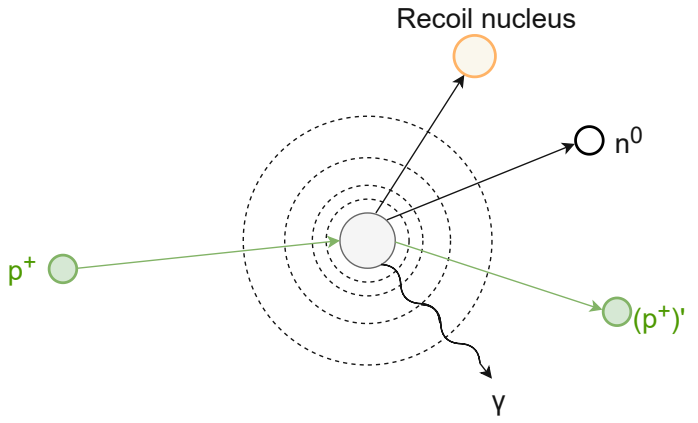


Figure 2.1.3: Non-elastic scattering of a proton with an atomic nucleus. Figure based on Newhauser and Zhang [8].

### 2.1.4 Ion range and range straggling in matter

The ion range is a quantity closely related to the SP. It is used to describe the depth in an absorber, where half of the initial ions have come to rest [8]. Mathematically, the range of an ion beam with initial energy $E_{\text{init}}$ per nucleon can be written as

$$R(E_{\text{init}}) = \int_0^{E_{\text{init}}} \frac{dE}{dE/dx} = \int_0^{E_{\text{init}}} \frac{dE}{S(E)}. \tag{2.1.12}$$

This equation can be solved numerically by approximating the integral with a sum

$$R(E_{\text{init}}) \approx \sum_0^{E_{\text{init}}} S(E)^{-1} \Delta E. \tag{2.1.13}$$

Actually, the definition in equation (2.1.13) returns the average path length (not the range) of ions within an absorber. However, on average, an ion's path is nearly equal to its projected path/range, which is why equation (2.1.13) is nevertheless a good approximation for the range for most use cases [8].

A numerical calculation may be computationally extensive and therefore not fitting for all applications [8]. For this reason, multiple analytical models were developed to calculate ion ranges in matter [23–25] which started from the idea of a simple SP definition [26] known as the Bragg-Kleeman rule

$$S(E) = -\frac{E^{1-p}}{\alpha p}, \tag{2.1.14}$$

with material- and ion-specific parameters $\alpha$ and $p$, which were fitted for protons, helium and carbon ions in Zhang et al. [27]. The relation between SP and range as given in equation (2.1.12) allows calculating the range from this rule by simple analytical integration yielding

$$R(E_{\text{init}}) = \alpha E_{\text{init}}^{p}. \tag{2.1.15}$$

Another example for an analytical model for the range calculation is the Donahue formula [24], which can be seen as a refinement of equation (2.1.15). In their approach, the range is defined as

$$R(E_{\text{init}}) = \frac{1}{\kappa}\left[\beta E_{\text{init}}^{q} + \alpha E_{\text{init}}^{p} + \frac{h}{g}\left(\exp\left(-gE_{\text{init}}\right) + gE_{\text{init}} - 1\right)\right]u, \tag{2.1.16}$$

where $\kappa$ is a constant, $u$ is the atomic mass number of the projectile and $\alpha$, $\beta$, $g$, $h$, $p$, and $q$ are material-dependent parameters which allow for a more accurate estimation of ion ranges and a validity of the model over a higher energy range than the two-parameter Bragg model [26].

The range can only be seen as an average quantity characterizing an ion beam at a certain energy. Regarding single ions, however, the energy loss in a medium cannot be regarded as continuous and along a straight line. These actual deviations in the energy loss are referred to as range straggling or energy straggling [8].

In figure 2.1.4, the energy loss of the single ions within a 200 MeV proton beam in various water absorbers is shown in respective histograms. For thick absorbers (many individual collisions possible), the energy loss distribution is symmetric, with an average value $\Delta E_{\text{avg}}$ of zero. This distribution can be approximated by a Gaussian fit [28] which can be written as [8]

$$f(\Delta E)\mathrm{d}\Delta E = \frac{1}{\sigma_{\Delta E}\sqrt{2\pi}} \exp \frac{-(\Delta E - \bar{\Delta E})^2}{2\sigma_{\Delta E}^2}, \tag{2.1.17}$$

where the variance $\sigma_{\Delta E}$ for non-relativistic ions is directly proportional to the absorber thickness $x$ and material density $\rho$. This approximation for energy straggling assumes that the absorber is composed of unbound electrons and the velocity of the incident ion does not strongly decrease within the absorber [8].

In thin absorbers (i.e., the total energy loss is small compared to the initial beam energy), the energy loss in the absorber defined by a few interactions only. As the energy loss due to one such interaction can be large, the distribution becomes asymmetric: as seen in figure 2.1.4, the maximum value of the probability distribution shifts to the left and the distribution develops a long tail to the right side. These distributions can be best described with Vavilov's [29] or Landau's [30] theory. If the number of interactions in the absorber increase (thick absorber), the distribution becomes Gaussian-shaped (central-limit-theorem).

In the latter, the range straggling is described as a function depending on the approximate mean energy loss $\xi$ and the deviation from the mean energy loss $\phi_L$ [8]

$$f(\Delta E, \rho x)\mathrm{d}\Delta E = \frac{1}{\xi}\phi_L, \tag{2.1.18}$$

where $\phi_L = \phi_L(\lambda_L)$ depends on the Landau length $\lambda_L$ and is written as

$$\phi_L = \frac{1}{\pi}\int_0^\infty \exp\left(-y(\ln y - \lambda_L)\right)\sin(\pi y)\mathrm{d}y. \tag{2.1.19}$$

Vavilov's theory corresponds to a generalization of Landau's theory, which is computationally more expensive [8].

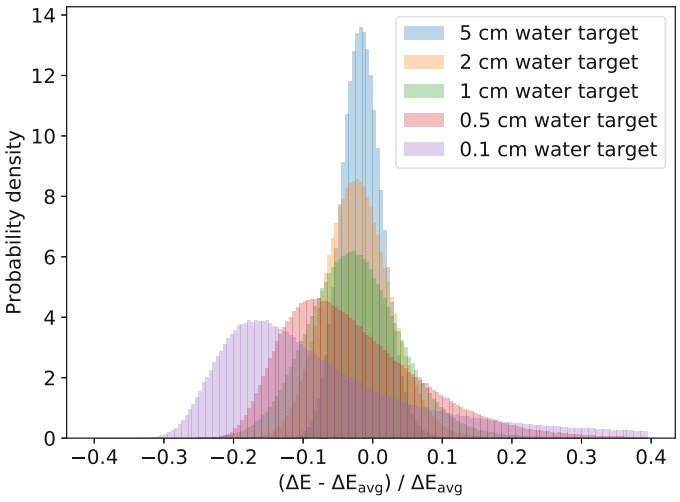


Figure 2.1.4: Energy loss probability density for a 200 MeV proton beam in various water absorbers. As in Newhauser and Zhang [8], the distribution was normalized on both axes: the ordinate is normalized to the average energy loss value $\Delta E_{\mathrm{avg}}$, whereas the probability density was normalized such that the integral over the distribution equals one. Data were created with Monte Carlo simulations using the Geant4 application for tomographic emission (GATE) [31] and $10^6$ primary particles.

## 2.2 Ion beam therapy

According to the World Health Organization (WHO), cancer is one of the main reasons for worldwide death cases, causing approximately one in six deaths in 2020 (a total of 10 million death cases and a total of 19.3 million new cases) [32, 33]. Although Europe only accounts for 9.7% of the world's population, it makes up 22.8% of the cancer cases and 19.6% of the

cancer deaths [34]. While America accounts for 20.9% of cancer cases and 14.2% of cancer deaths, the situation in Asia and Africa is reversed: both regions hold a higher fraction of worldwide cancer deaths (Asia: 58.3%, Africa: 7.2%) than of the actual cancer cases (Asia: 49.3%, Africa: 5.7%) [34].

To reduce the number of cancer deaths, regular medical check-ups and an adequate treatment are key factors. For most cancers, a combination of chemotherapy, surgery and radiotherapy is suitable: until 2015, approximately two thirds of cancer patients received a form of radiotherapy (x-ray, gamma knife, brachytherapy, ion beam therapy or other) [35]. While approximately 80% of the radiotherapy patients received treatment with x-rays, only 0.8% were treated with ions [35]. However, this number was and is steadily increasing: until 2014, 137 000 patients were treated with ions, which has increased to approximately 290'000 until 2020 (≈250'000 with protons, ≈40'000 with carbon ions and ≈3'500 with helium ions and others) [36].

For ion beam therapy, the physical principles introduced in section 2.1 are exploited. While x-ray beams deposit a high dose at the first few centimeters after entering a patient, the ion energy deposition per unit path is given by equation (2.1.3) and shows inverse proportionality to the squared ion velocity. Therefore, an ion beam deposits the maximum dose per unit path length shortly before most ions have come to rest. This principle is demonstrated in figure 2.2.1: for the (red) x-ray beam, an exponential decrease follows after the first dose build-up within approximately 50 mm. The build-up results from the release of secondary electrons by the x-rays which then again damage the cells on their path (photons are indirectly ionizing radiation) [21]. This build-up process continues until an equilibrium is reached, while on the other hand, the beam is continuously attenuated following Lambert-Beer's exponential law [4, 21] (see section 2.3.1). In contrast to that, the dose for protons, helium ions and carbon ions (blue, orange and green curves) steadily increases until it has reached its maximum at approximately 250 mm for the given energies. After the maximum value, which is referred to as Bragg-peak, the dose almost immediately falls to a low value. Here, some differences between protons and other ions can be observed: for protons, the dose falls close to zero directly after the Bragg-peak, whereas the distributions for helium and carbon ions show a tail with increased dose after the maximum. This tail results from the fragmentation of the target atoms and primary ions.

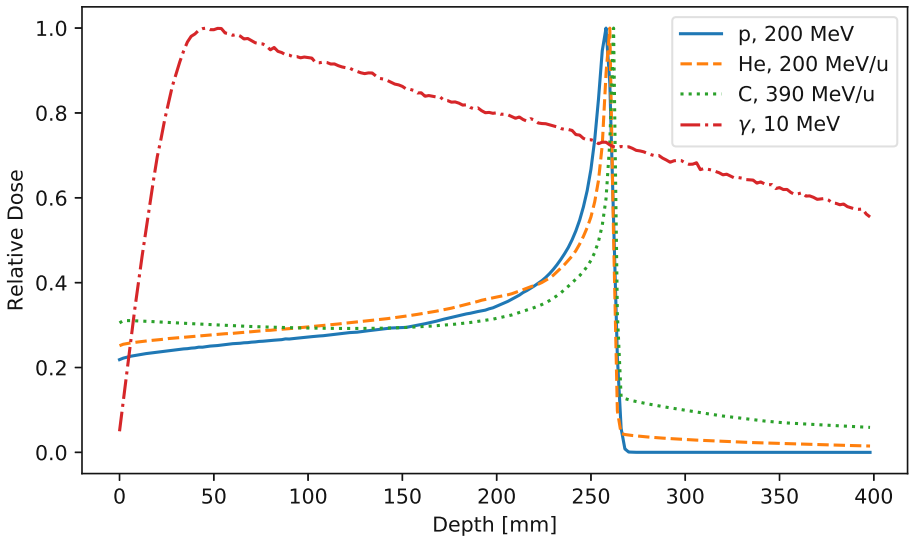


Figure 2.2.1: Depth dose for photons, protons, helium ions and carbon ions in a 40 cm water target. The curves were normalized to their maximum value for better comparison. For each particle species, $10^6$ primaries were used in a GATE [31] Monte Carlo simulation to generate the dose profiles.

The shape of an ion beam's energy deposition in matter is suitable for treating deep-seated tumours, where a high dose is desirable in the region of malignant cells. At the same time, the healthy tissue surrounding the tumour should be spared as far as possible. For demonstration purposes, figure 2.2.2 shows the dose distribution of two rectangular photon beams (left), two rectangular proton beams (middle) and two rectangular carbon ion beams (right) targeting a tumour within a patient phantom. The beam shapes were optimized using the matRad [37] software. This example is only for demonstration purposes and does not represent an actual treatment plan. However, it shows the advantages of particle beam therapy over x-ray radiation therapy: for the photon beam, a high dose (red) can be observed in the area surrounding the tumour, whereas the proton and carbon ion beams only show a high dose in the tumorous area itself.

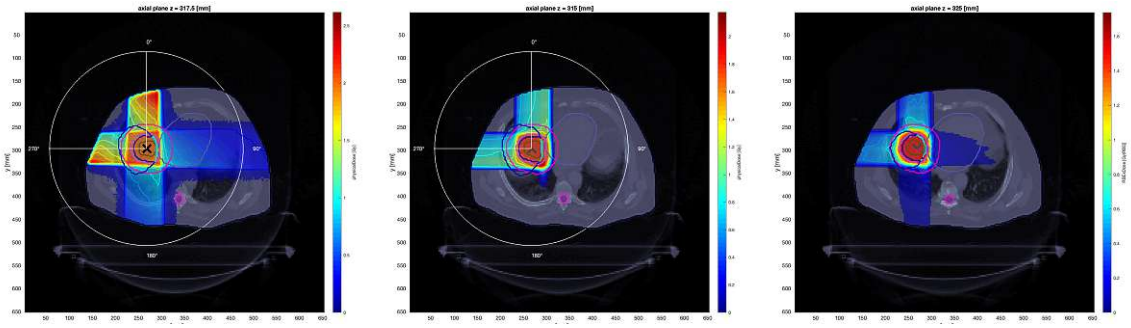

Figure 2.2.2: Dose distribution for two photon beams (left), two proton beams (middle) and two carbon ion beams (right) for a liver phantom (target is marked with an **X**). The dose distribution for this target (which is included as an example phantom in the software) was calculated using matRad [37]. The images do not represent a real treatment (plan) but are only intended to visually demonstrate the different behaviour of photon and ion beams in matter. In a realistic scenario, more than two photon beams would be used to target the tumour in order to keep the dose to the surrounding tissue at a lower level.

Furthermore, the photon beams do not get fully absorbed within the tumour. Hence, again in contrast to protons, a remaining dose can be observed behind the tumorous area. Due to the fragmentation tail, this is also the case for helium or carbon ions. In general, the example given in figure 2.2.2 shows that more beam directions (portals) will be used in x-ray therapy to achieve a high dose only in the tumour and a low dose in the surrounding area, while fewer beam directions will be needed for ion beam therapy.

The following sections discuss some aspects of ion beam therapy in more detail. Section 2.2.1 gives a short introduction to ion beam therapy treatment centres, while in section 2.2.2, more details on the treatment process are given. Section 2.2.3 introduces quantities that are typically used in ion beam therapy and imaging.

### 2.2.1 Treatment facilities

Figure 2.2.3 shows the ion-beam treatment facilities that are currently in operation. The available ion species are labelled in the image. Regarding the technology, the most used accelerator type for ion beam therapy is the (synchro-)cyclotron, followed by synchrotron facilities [38]. These accelerators belong to the category of circular accelerators, which use electric fields to further increase the velocity of charged particles with every round on the circular or spiral particle trajectory through the complex. The advantage of a cyclotron lies in the simplicity of its design, the reduced size compared to other technologies and low operating costs. However, the technology does not allow for energy modulation (external absorbers are necessary) [35]. Furthermore, while the accelerator makes up an essential part of the cost for a therapy centre, the expenses for beam line and gantry even exceed these costs [35]. In the following, a short overview of the principles of (synchro-)cyclotron and synchrotron

technologies is given. The text below represents a summary of the detailed discussion of Demtröder [14].

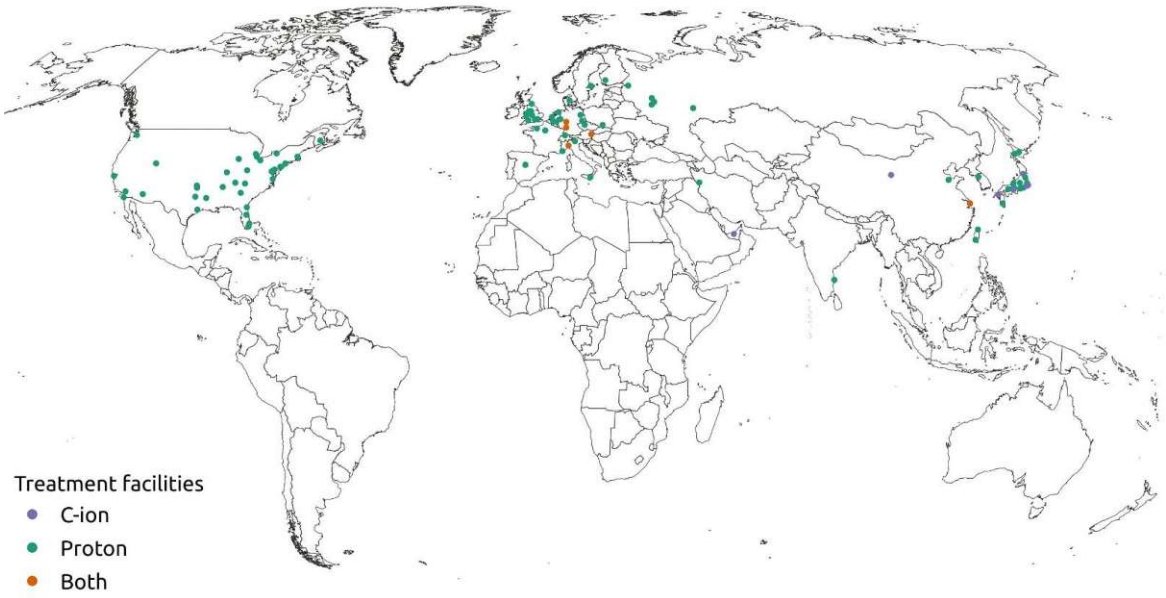


Figure 2.2.3: Operational treatment facilities for ion beam therapy. The figure was based on data from PTCOG [38] and was created with QGIS [39].

**(Synchro-)Cyclotron** A vacuum chamber consisting of two D-shaped parts is located between the poles of an electromagnet, and a high frequency voltage is applied between these two parts. Positive ions are emitted from an ion source between the chamber parts and accelerated towards the negatively charged chamber side. In the chamber, no electric field is present. Hence, the particle trajectories describe semicircles with a radius defined by the equilibrium of Lorentz force and centripetal force. As the circulation time can be assumed as constant at non-relativistic energies, the polarity of the chamber sides is reversed each time ions have passed through half a circle, leading to continuous acceleration. The semicircles describing the ion's trajectories show an increasing radius due to the increasing energy of the ions. If the ions arrive at the maximum radius (corresponding to the end of the magnetic field), they are extracted from the cyclotron.

At high energies, the circulation time changes due to the relativistic effects. After some circulations, the ions will therefore arrive at the gap between the chamber sides at the wrong frequency period, leading to a deceleration instead of further acceleration. To compensate this problem, the synchro-cyclotron reduces the high frequency so that it always stays in sync with the circulation time.

**Synchrotron** To achieve even higher energies (proton energies in the order of $10^3$ MeV), the cyclotron technology is not suitable, as the ion circulation radius increases proportionally to the kinetic energy of the particle. To reduce the radius, a higher magnetic field can be applied. However, this is not feasible at high energies for a cyclotron, where the magnet covers the whole circular area. At synchrotrons, ions are accelerated in a thin vacuum tube with a fixed radius. Along the circular geometry, multiple electromagnets cause a regional magnetic field which is steadily increasing to keep the ions on the requested path. Ions are injected tangentially into the synchrotron from a linear accelerator (LINAC).

### 2.2.2 Spread-out Bragg peak and biological effectiveness of ions

The preferable dose distribution of ion beams over photon beams has already been discussed in section 2.2. Multiple beam energies are used for particle therapy to achieve an evenly distributed high dose in the tumorous area. The principle is demonstrated in figure 2.2.4 for proton beams: the overlay of multiple proton beams with different beam energies (orange) results in the so-called spread-out Bragg peak (SOBP) (blue). While in the example, an overlay of five different beam energies is shown, an overlay of more beam energies, as typically used in ion beam therapy, would lead to a uniform dose distribution within the tumorous area.

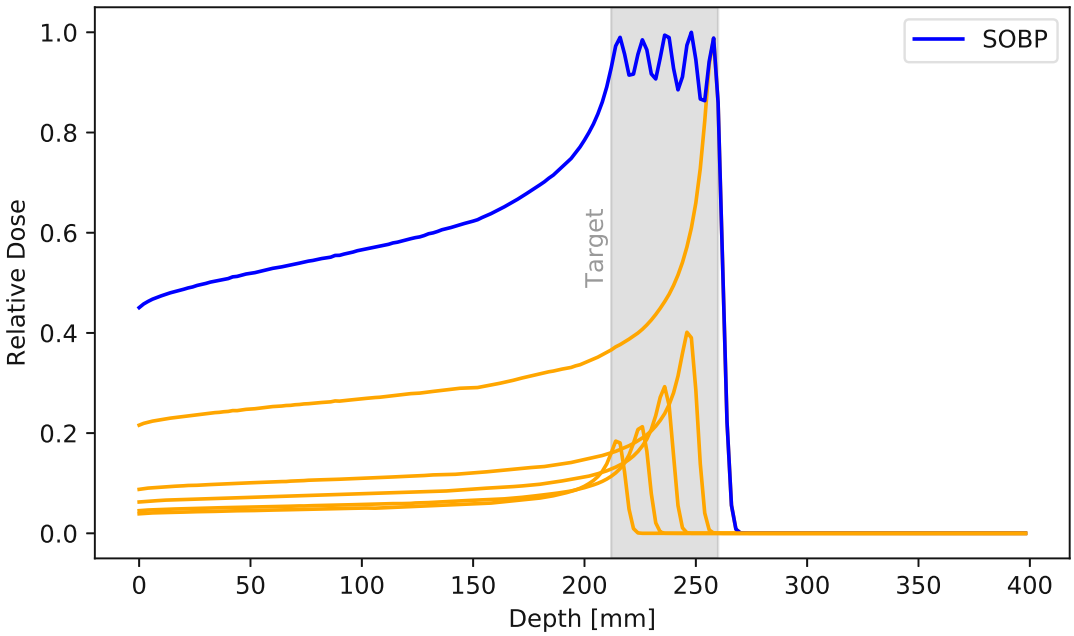


Figure 2.2.4: Spread-out Bragg peak (blue) resulting from multiple proton beams with energies ranging from 180 MeV to 200 MeV (orange). Using further beam energies and ripple filters [40, 41] would lead to a more even dose distribution in the tumorous area (grey).

However, the targeting of tumours with ion beams is not as straight forward as indicated in figure 2.2.4. Besides the favourable dose profile of ions over photon beams, the biological effectiveness, which has a major impact on the treatment plan, has to be discussed. The effect of radiation does not only depend on the physical dose, but also on the cell response to the incoming radiation [21]. This quantity is measured with the relative biological effectiveness (RBE)

$$\mathrm{RBE} = \frac{D_{\mathrm{ref}}}{D}\bigg|_{\text{same biological effect}} \tag{2.2.1}$$

which is the relation of a reference dose $D_{\mathrm{ref}}$ needed to achieve the same biological effect as with a certain dose $D$ of the radiation under investigation. As reference radiation, typically $\gamma$ radiation from $^{60}$C [42] or x-rays [43, 44] are used. With this definition, the RBE for protons was found to be between 1.1 and 1.6 [42, 45]. In proton therapy treatment planning, a fixed RBE of 1.1 is mostly used [46], although recent studies suggest considering a non-constant value to further improve the accuracy of treatment plans [47].

Compared to protons, helium ions (RBE up to 2.8 [45]) and carbon ions (3-5 [21, 42] or 2.1–3.3 [44]) show an even higher relative biological effectiveness. To account for this effect, the dose in ion beam therapy is usually given in Gy(RBE) to show that the dose was multiplied by the biological effectiveness. This was also done in figure 2.2.2, where SOBPs

were calculated in matRad [37] in a way that the RBE times the dose is maximized in the tumorous area.

One quantity that mainly influences the RBE is the linear (restricted) energy transfer (LET) [21]

$$\mathrm{LET}_\Delta = \frac{\mathrm{d}E_\Delta}{\mathrm{d}l}, \tag{2.2.2}$$

which is the energy transferred from the ion to a material (usually given in keV/$\mu$) while only interactions with an energy deposition smaller than $\Delta$ are considered. If $\Delta$ was set to infinity, the LET would correspond to the SP. Other factors influencing the RBE are dose level, ion species, LET spectrum, cell type and biological endpoint (chosen surviving fraction) [21].

### 2.2.3 Water-equivalent thickness and water-equivalent path length

Water shows similar material properties (e.g., similar density and effective $Z/A$ [8]) as human tissues and is therefore often used as reference material or tissue substitute in the clinical context. For characterizing the penetration depth of an ion beam or range calculations, the so-called water-equivalent thickness (WET) is therefore of interest.

According to the International Atomic Energy Agency (IAEA) [48], the WET, $t_\mathrm{w}$, can be approximated by the relation between the density of water $\rho_\mathrm{w}$ and of the material under investigation $\rho_\mathrm{m}$ as

$$t_\mathrm{w} = t_\mathrm{m}\frac{\rho_\mathrm{w}}{\rho_\mathrm{m}}c_\mathrm{m}. \tag{2.2.3}$$

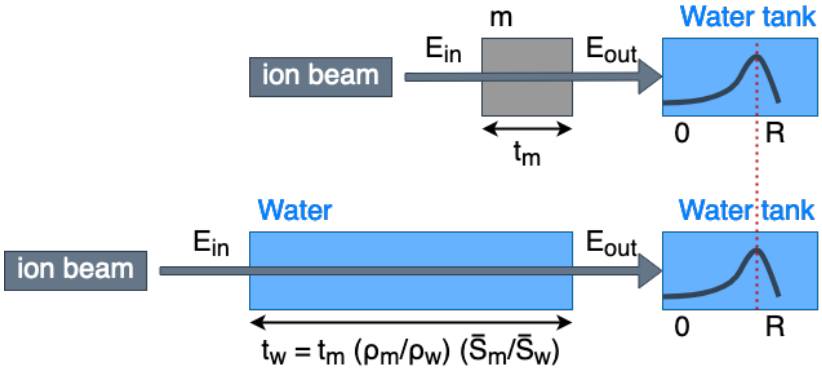


Figure 2.2.5: Schematic demonstration of the WET. An ion beam has a certain range $R$ in a water absorber after passing a material m with thickness $t_\mathrm{m}$. The same range can be observed after an ion beam with the same energy has passed through a water target with thickness $t_\mathrm{w}$. Figure based on Zhang and Newhauser [49].

Here, $c_\mathrm{m}$ represents a depth-scaling factor, which can be approximated by the relation of the beam range $R_\mathrm{w}$ in water and the range $R_\mathrm{m}$ in the material block, yielding for the WET

$$t_\mathrm{w} = t_\mathrm{m}\frac{R_\mathrm{w}}{R_\mathrm{m}}. \tag{2.2.4}$$

It is apparent that equations (2.2.3) and (2.2.4) are only valid for stopping-length objects, as the ranges correspond to a full energy loss of the ion beam [8]. For thin targets, the exact calculation of the WET is given in Zhang and Newhauser [49] as

$$t_\mathrm{w} = t_\mathrm{m}\frac{\rho_\mathrm{m}\bar{S}_\mathrm{m}}{\rho_\mathrm{w}\bar{S}_\mathrm{w}}, \tag{2.2.5}$$

where $\bar{S}_{\mathrm{w}}$ and $\bar{S}_{\mathrm{m}}$ are the mean mass SPs for ions in water and the material under investigation, which are defined as [49]

$$\bar{S} = \frac{\int_E S dE}{\int_E dE}. \tag{2.2.6}$$

The principle of the WET calculation for thin objects is demonstrated in figure 2.2.5: an ion beam passes through an absorber made of material m and with a thickness $t_{\mathrm{m}}$. In a subsequent water tank, the beam is fully slowed down and a residual beam range $R$ is measured. The WET corresponds to the thickness $t_{\mathrm{w}}$ of a water absorber which could be placed instead of the material block m to achieve the same residual range in the subsequent water tank [8].

In the context of ion imaging, the water-equivalent path length (WEPL) is an essential quantity as it corresponds to the measurement value for each ion, which is then again used as input for the image reconstruction process. Similar to the definition of the WET, this quantity refers to the water-equivalent of the actual proton path length and corresponds to the integral of the reciprocal SP of water over the ion's initial and residual energy ($E_{\mathrm{init}}$ and $E_{\mathrm{exit}}$, respectively) [21],

$$\mathrm{WEPL} = \int_{E_{\mathrm{init}}}^{E_{\mathrm{exit}}} S_{\mathrm{water}}^{-1} \mathrm{d}E. \tag{2.2.7}$$

## 2.3 Imaging for treatment planning

An adequate treatment plan is essential for performing ion beam therapy. For optimizing the dose profile in the patient tissues, the location of the tumor and the material properties have to be known with high accuracy. Therefore, a planning computed tomography (CT) is usually performed before the treatment. The image contrast in the resulting 3D image allows identifying the tumorous region, while the actual gray values give information on the tissue properties (linear attenuation coefficient in case of x-ray CT). In the following section, the principles of CT and the challenges in combination with ion beam therapy are discussed. Finally, as a possible solution to address these challenges, the basics of ion imaging are presented in section 2.3.2.

### 2.3.1 Computed tomography

The information in a CT image is obtained from the continuous attenuation of the incident x-ray beam following the exponential Lambert-Beer law [4, 5]

$$I = I_0 \exp(-\mu \mathrm{d}s), \tag{2.3.1}$$

with the initial beam intensity $I_0$, the linear attenuation coefficient $\mu$ and the path length $\mathrm{d}s$. Along one ray, the initial beam intensity will therefore decrease to a value $I$ depending on the different attenuation coefficients $\mu_1, ..., \mu_n$ [50] along this ray

$$I = I_0 \exp(-\mu_1 \mathrm{d}s) \cdot \exp(-\mu_2 \mathrm{d}s) \cdots \exp(-\mu_n \mathrm{d}s) \tag{2.3.2}$$

$$= I_0 \exp(-\sum_k \mu_k \mathrm{d}s) \tag{2.3.3}$$

$$\approx I_0 \exp(-\int \mu(s) \mathrm{d}s), \tag{2.3.4}$$

where each linear attenuation coefficient is actually composed of three parts [50],

$$\mu_n = \mu_{\mathrm{photo},n} + \mu_{\mathrm{Compton},n} + \mu_{\mathrm{pair},n}. \tag{2.3.5}$$

$\mu_{\text{photo},n}$ corresponds to the contribution of the photoelectric effect. This effect represents the full absorption of the energy of a photon by an electron from the electronic shells of the target atoms. The Compton effect ($\mu_{\text{Compton},n}$) corresponds to the partial energy transfer of a photon to an electron. For energies above 1.022 MeV, the pair production effect ($\mu_{\text{pair},n}$) becomes relevant. Here, a photon gets converted to an electron-positron pair when passing close to an atomic nucleus [50].

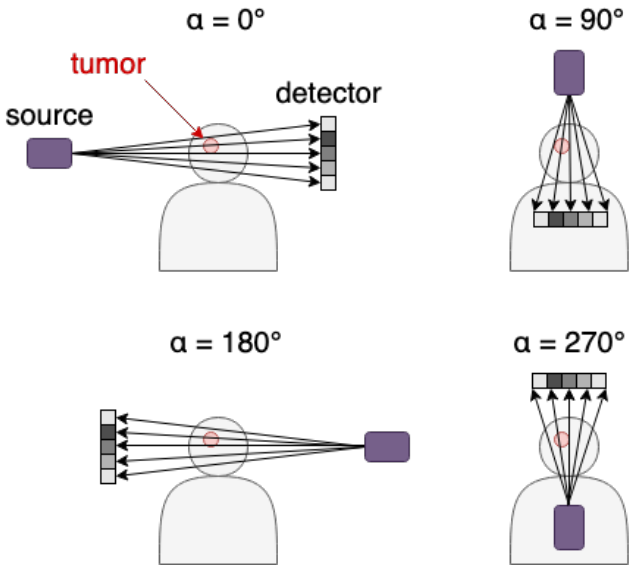


Figure 2.3.1: Principle of a CT scan: a source (x-ray tube) is rotated around the patient, and at several angles, measurements of the beam attenuation are taken with an array of x-ray detectors. In the given example, a cone beam (point source with an adequate opening angle) is displayed. The obtained attenuation profile not only depends on the patient geometry, but also on the beam angle. This fact allows reconstructing a 3D image from the obtained data. Figure based on Birkfellner [50].

The knowledge of $I/I_0$ is used in CT image reconstruction in order to obtain the attenuation coefficients of the penetrated tissues (for details, see section 2.5). The basic principle of a CT scan is presented in figure 2.3.1: the scanner system has to be rotated around a patient or object-to-be-imaged (phantom) in order to measure the attenuation profile at several angles. This allows to reconstruct a 3D image from the measured data, which correspond to integrals along various x-rays (see equation (2.3.4)). Usually, the values in the resulting image are expressed in so-called Hounsfield units (HUs) in the reconstructed image [50],

$$HU = \frac{\mu_{\text{m}} - \mu_{\text{w}}}{\mu_{\text{w}} - \mu_{\text{a}}} \cdot 1000, \tag{2.3.6}$$

with the linear attenuation coefficient of water $\mu_{\text{w}}$ and air $\mu_{\text{a}}$. With this definition, the scale has two fixed points: the HU of air equals −1000, whereas the value for water equals 0.

Here, one challenge for ion beam therapy becomes apparent: the HUs obtained from the CT image do not describe the ion beam behavior in the investigated tissues. A conversion from HUs to RSPs is therefore necessary. Such a conversion procedure between HUs and RSPs was described by [11], where patient tissues were replaced by appropriate substitutes in the experiment to investigate the relation between the two physical quantities. To account for the different chemical compositions of tissue substitutes and real tissues, measured HUs were corrected by the chemical composition of real tissues [11].

Although HUs and RSPs are strongly correlated (both of them are mainly influenced by the electron density of a material [21]), the conversion process remains one of the primary sources of range uncertainties in ion beam therapy treatment planning, leading to the need

for safety margins around the tumorous area [51]. These additionally irradiated areas become especially crucial when a tumor near a sensitive area (e.g., optical nerve) is irradiated [35].

### 2.3.2 Ion computed tomography

The concept of ion imaging was already investigated by Cormack [1] and Koehler [2] in the 1960ies. The imaging technique was then revived in the context of ion beam therapy treatment planning: the need to convert HUs to RSP values can be prevented when ions are directly used in the imaging process. Thus, the same particle species is used for the planning CT scan and the subsequent radiation therapy. However, other challenges arise in this context: although the general principles are similar to a conventional CT scan with x-rays, some essential differences between those two imaging modalities have to be considered due to the different interaction mechanisms of photons and ions in matter. While photon beams can be considered as straight lines in matter, this is not a good approximation for ion paths in matter as they are subject to MCS as discussed in section 2.1.2.

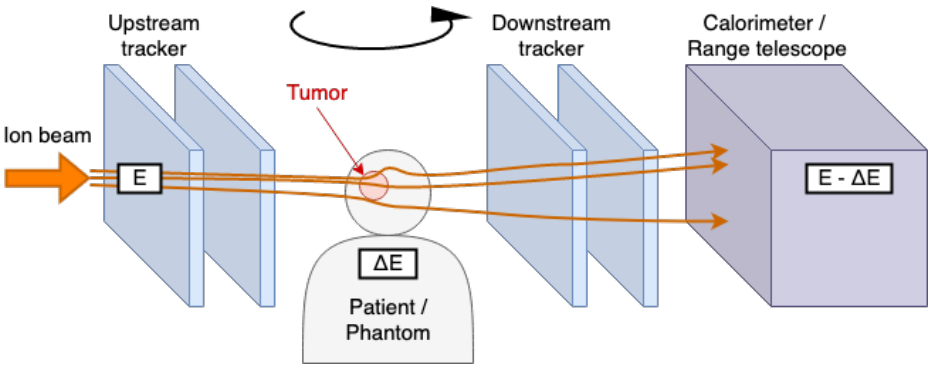


Figure 2.3.2: Principle of an iCT scan: An ion beam is directed through the patient. A cone beam or a parallel beam (pencil beam scanning) may be used. The single ions of the beam are detected with a tracking setup upstream and downstream of the patient. Finally, the residual energy (or range) is measured in a calorimeter or range telescope. As for conventional CT, the setup is rotated around the patient to take measurements at several angles.

In fact, these random scattering events lead to totally independent and different paths for each single ion. While on average, ions will still pass on a straight line through a medium, a substantial number of particles will show steep exit angles. If the ion data is simply binned in a rear detector (as it would be done for x-ray CT), this would lead to a blurry image in the reconstruction process.

Therefore, a potential iCT setup [9] (see figure 2.3.2) consists of two tracker modules (upstream and downstream of the patient or phantom) and a range telescope or calorimeter. With the trackers, the position and direction of every single ion is recorded before and after passing through the object-to-be-imaged. The range telescope or calorimeter records the energy loss of the ion, which is usually converted to the WEPL of the respective ion (see equation (2.2.7)). Instead of binned data, all those single-event data (referred to as list-mode data) have to be used in the image reconstruction process.

## 2.4 Path estimates for ion imaging

In order to account for MCS in ion imaging, a path estimate for each ion has to be made and incorporated in the image generation process. The most trivial approach is to approximate the path by a straight line (SL), which is sufficiently accurate for ions travelling through air surrounding a patient or phantom. However, in denser materials, this ion path estimate

becomes inaccurate due to the increased scattering and a blurry image will be obtained as ions will be assigned to wrong pixels or voxels.

Multiple sophisticated path estimates have therefore been developed for ion imaging [52–56]. Usually, the ion entrance and exit point to a patient or phantom are calculated by expanding the upstream and downstream detector hit positions to the object hull on a straight line following the measured direction of the particle. In the object hull (also referred to as convex hull), the sophisticated path estimate is used.

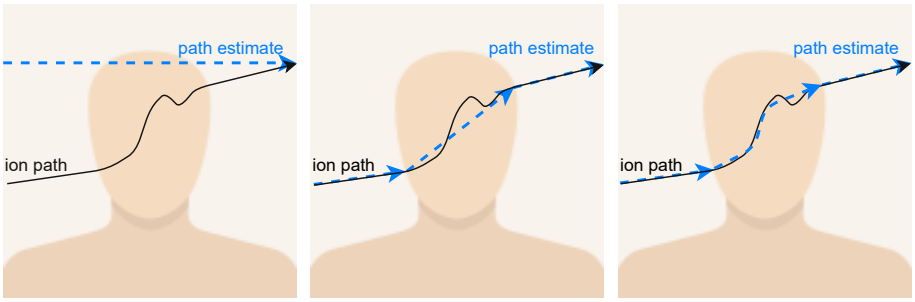


Figure 2.4.1: Sketch of various ion path estimates. Left: Simple straight-line approach, depending on the point-of-arrival only (corresponding to the method used in x-ray CT). Middle: Straight-line ion path estimate consisting of three segments (both position and direction measurements are used). Right: Curved ion path estimate (e.g.; most likely path or (optimized) cubic spline). In air, a straight-line path is used.

A few possibilities for an ion path estimate are shown in the sketch in figure 2.4.1. It is apparent that a SL approach is less accurate than a curved proton path estimate, which was also demonstrated by Wang et al. [57]. Two sophisticated ion path estimates, that were used in the scope of this thesis, namely the most likely path (MLP) formulation of Schulte et al. [53] and the optimized cubic spline defined by Fekete et al. [56], are discussed in further detail in the following sections.

### 2.4.1 Most likely path

Schulte et al. [53] employed Bayesian statistics in order to describe the MLP as a maximum likelihood problem. In the following, the beam direction is defined as $w$ and the orthogonal directions as $t$ and $v$ (see figure 2.4.2). For demonstration purposes, it is sufficient to describe the MLP formalism in the $w-t$ plane, as the formalism is the same in the $w-v$ plane and scattering in the orthogonal directions is uncorrelated. In their approach, Schulte et al. [53] combine the characteristics of an incident ion in a vector $y_0$ containing the initial ion position $t_0$ and direction $\theta_0$,

$$y_0 = \begin{pmatrix} t_0 \\ \theta_0 \end{pmatrix}. \tag{2.4.1}$$

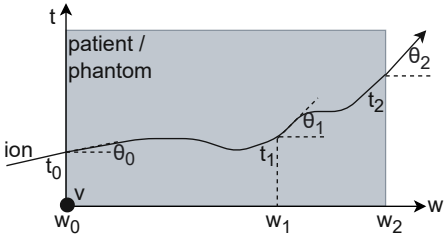


Figure 2.4.2: Variable definition of the MLP formalism. Figure based on Schulte et al. [53] and Kaser et al. [58].

While the exit coordinates $y_2$ – consisting again of a position $t_2$ and direction $\theta_2$ – are known from the downstream tracker measurements, the coordinates $y_1$ at an arbitrary position between $y_0$ and $y_2$ are unknown. The likelihood of an ion passing exactly through position $y_1$ with the given entry data can be written as $L(y_1|\text{entry data})$, whereas the likelihood to find such an ion with the given exit data can be written as $L(y_1|\text{exit data})$ [53]. In order to find the MLP ($y_1 = y_{\text{MLP}}$), the latter likelihood needs to be maximized. A solution to this problem was found in Schulte et al. [53] as

$$y_{\text{MLP}} = \begin{pmatrix} t_{\text{MLP}} \\ \theta_{\text{MLP}} \end{pmatrix} = (\Sigma_1^{-1} + R_1^T \Sigma_2^{-1} R_1)^{-1} (\Sigma_1^{-1} R_0 y_0 + R_1^T \Sigma_2^{-1} y_2), \tag{2.4.2}$$

with $R_0$ and $R_1$ defined as

$$R_i = \begin{pmatrix} 1 & w_{i+1} - w_i \\ 0 & 1 \end{pmatrix}, \quad i = 0, 1. \tag{2.4.3}$$

$\Sigma_1$ and $\Sigma_2$ correspond to the scattering matrices depending on the variances and covariances between $t_1$ and $\theta_1$ or $t_2$ and $\theta_2$, respectively

$$\Sigma_i = \begin{pmatrix} \sigma_{t_i}^2 & \sigma_{t_i\theta_i}^2 \\ \sigma_{t_i\theta_i}^2 & \sigma_{t_i}^2 \end{pmatrix}, \quad i = 1, 2. \tag{2.4.4}$$

While the exact definitions of the elements of the scattering matrices are given in appendix A.1, one term is discussed in more detail in the following. All the scattering elements $\sigma$ contain an integration of the form

$$\int_{w_0}^{w_1} \frac{w^n}{\beta(w)^2 p(w)^2} \mathrm{d}w, \quad n = 0, 1, 2, \tag{2.4.5}$$

where the term $(\beta^2 p^2)^{-1}$ is dependent on the rest energy of the ion $E_{\text{rest}}$ and the kinetic energy $E$ at a depth $w$ and can be written as [53]

$$\frac{1}{\beta(w)^2 p(w)^2} = \frac{(E(w) + E_{\text{rest}})^2 c^2}{(E(w) + 2E_{\text{rest}})^2 E(w)^2} \approx \sum_{i=0}^{5} a_i w^i. \tag{2.4.6}$$

As seen in equation (2.4.6), $(\beta^2 p^2)^{-1}$ is usually approximated by a polynomial with the parameters $a_i$ to avoid numerical integration [52, 53, 59]. The parameters are therefore typically extracted from a preceding Monte Carlo simulation, where the value of $(\beta^2 p^2)^{-1}$ is extracted at multiple thicknesses within a (water) target and a polynomial fit is calculated afterwards. In order to allow an analytical integration of equation (2.4.5) without an additional Monte Carlo simulation, Kaser et al. [58] investigated analytical approaches to solve this problem. For the investigated calculations, the range definition of Bortfeld [23] for protons in matter,

$$R = \alpha E^q, \tag{2.4.7}$$

which only depends on two material-specific parameters ($\alpha$, $q$), was used. With this approach, a relationship between the energy of a proton at a depth $w$ and its initial range $R_0$ is given by

$$E(w) = (R_0 - w)^{1/q}, \tag{2.4.8}$$

which can be inserted into equation (2.4.6). The values for $\alpha$ and $q$ given in Bortfeld [23] are only valid for protons up to 200 MeV and mainly influence the complexity of the integration given in equation (2.4.6) [58]. The approaches that were therefore investigated for protons and helium ions up to 300 MeV in Kaser et al. [58] used different values for these parameters based on the minimization of the figure-of-merit

$$\mathrm{FOM}_i = \sqrt{\left(\frac{|R_{\mathrm{fit},i} - R|}{\Delta_R}\right)^2 + 0.97\left(\frac{|S_{\mathrm{fit},i} - S|/S}{\Delta_S}\right)^2 + 0.03\left(\frac{\max(|S_{\mathrm{fit},i} - S|)/S}{\Delta_S}\right)^2}, \tag{2.4.9}$$

with $\Delta_S$ and $\Delta_R$ defined as 10 % and 0.1 cm, respectively [24]. The SP $S$ is defined as

$$S = \frac{dE}{dw} = \frac{1}{\alpha^{1/q}}(R_0 - w)^{1-\frac{1}{q}} \tag{2.4.10}$$

in the Bortfeld [23] model. In the following, the analytical calculation approaches investigated in Kaser et al. [58] are briefly discussed. Furthermore, a third option (option A) is introduced as a reference method to evaluate the performance of the two new approaches.

**Option A** This option represents the reference method corresponding to the MLP calculation described by Schulte et al. [53]. A Monte Carlo simulation is performed in which $(\beta^2 p^2)^{-1}$ is recorded in multiple thicknesses of a water target. The term is fitted with a polynomial and the fit parameters are used to calculate equation (2.4.6) and, from that result, the full MLP estimate given by equation (2.4.2).

**Option B** To simplify the integral in equation (2.4.6), the parameter $q$ of the Bortfeld model was fixed at 1.75 which is close to the value originally proposed [23]. By minimizing the figure-of-merit in equation (2.4.9), as described in Kaser et al. [58], $\alpha$ was found to be $2.41 \times 10^{-3}$ ideally. This option allowed for a fully analytical integration of equation (2.4.5). The resulting analytical solutions to integrals can be found in appendix A.2.

**Option C** The parameters $q$ and $\alpha$ were both optimized by minimizing equation (2.4.9) and were found to be 1.7174 and $2.88 \times 10^{-3}$, respectively. With these parameters, $(\beta^2 p^2)^{-1}$ was calculated at various depths $w$ in a water phantom and a fit was added to the results, similar to the previously used fit to Monte Carlo simulation data [53]. By doing so, equation (2.4.5) can again be analytically evaluated, based on the fit parameters. Hence, this option (which is more accurate than the previous option) does not prevent the need for a data fit, but the analytical calculation of $(\beta^2 p^2)^{-1}$ has the potential to replace the additional Monte Carlo simulation.

As an example, MLP estimates for a helium ion in a 20 cm water target are given in figure 2.4.3. In the image, various path estimates (options A-C), are compared to the 'real' ion path (as extracted from a Monte Carlo simulation) throughout the phantom. While in the given example, the maximum error of the path estimates (all options) was found to be approximately $-3.5 \times 10^{-2}$ cm at maximum, the estimates themselves hardly differ: The difference between estimates from options A and B was found to be $6 \times 10^{-4}$ cm at maximum. For option C, the difference to the reference method (option A) was found to be even smaller: the path estimate based on a Monte Carlo simulation differed at maximum by approximately $4 \times 10^{-4}$ cm from the path estimate obtained from option C. This confirms that the presented analytical calculation methods are a valid option for replacing a Monte Carlo simulation in the MLP calculation process. Further analysis was done in Kaser et al. [58], where a total of 3000 path estimates were evaluated for various proton and helium ion energies and water phantom thicknesses. The root mean square error (RMSE) of path estimates using options A-C from the real ion paths was calculated. While the RMSE was found to be 0.1 cm at maximum for protons in a 40 cm water target, the difference between the RMSEs of the different path estimates was found to be only in the order of 1 µm.

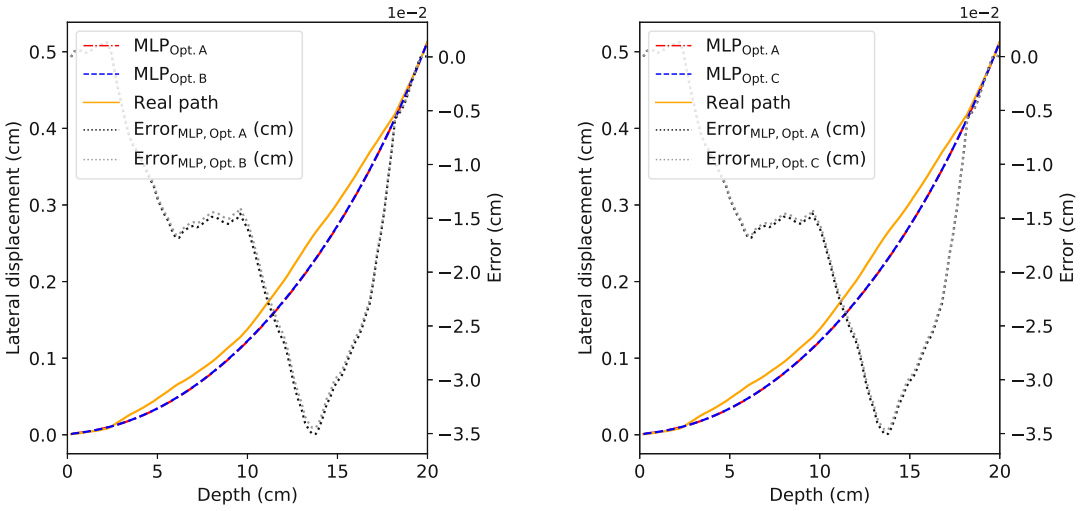


Figure 2.4.3: MLP estimates for a 200 MeV helium ion in a 20 cm water target. $\text{MLP}_{\text{Opt. A}}$ stands for the path estimate using a preceding Monte Carlo simulation, whereas $\text{MLP}_{\text{Opt. B}}$ and $\text{MLP}_{\text{Opt. C}}$ represent the newly investigated MLP estimates using an analytical calculation of $(\beta^2 p^2)^{-1}$ (option C) or a fully analytical calculation of the integrals represented by equation (2.4.6) (option B).

### 2.4.2 Cubic spline

Li et al. [59] have already investigated the performance of a cubic spline (CS) ion path in comparison to an MLP approach. While, as expected, both of these approaches showed better accuracy than a SL path estimate, the MLP formalism outperformed the CS. However, Fekete et al. [56] developed an optimized CS path estimate for ions in heterogeneous materials. The ion position $p_{\text{CS}}$ along the path estimate is defined as [56]

$$p_{\text{CS}} = (2t^3 - 3t^2 + 1)p_0 + (t^3 - 2t^2 + t)d_0 + (-2t^3 + 3t^2)p_1 + (t^3 - t^2)d_1, \tag{2.4.11}$$

with the initial and final position $p_0$ and $p_1$, initial and final direction $d_0$ and $d_1$ and the running parameter $t \in [0, 1]$. The direction vectors are optimized according to Fekete et al. [56]

$$\begin{aligned} d_0 &= \hat{d}_0 \, \lambda_0 \, |p_1 - p_0|, \\ d_1 &= \hat{d}_1 \, \lambda_1 \, |p_1 - p_0|, \end{aligned} \tag{2.4.12}$$

where $\lambda_0$ and $\lambda_1$ are defined as

$$\begin{aligned} \lambda_0 &= 1.01 + 0.43 \left( \frac{\text{WET}}{\text{WEPL}} \right)^2 \\ \lambda_1 &= 0.99 - 0.46 \left( \frac{\text{WET}}{\text{WEPL}} \right)^2 . \end{aligned} \tag{2.4.13}$$

For the WEPL, equation (2.4.7) is calculated with $\alpha = 0.0244$ and $q = 1.75$ [56] which is a good approximation for the proton and helium ion range in water [17, 27, 58]. The WET corresponds to the actual measurement value for each ion obtained from the calorimeter or range telescope. Using this optimized direction vectors, the CS path estimate, which is further referred to as optimized CS, closely overlaps the MLP estimate for the ion path [56].

## 2.5 Image reconstruction in (ion) computed tomography

As seen in sections 2.3.1 and 2.3.2, the basic principles of x-ray CT and iCT are similar: an imaging setup is rotated around a patient or a phantom while a physical quantity $f(x, y)$, which depends on the material properties of the imaged object, is measured. This quantity can be understood as an integration over the beam's or particle's path through the medium. Image reconstruction aims to 'smear back' these integrals over a voxelized volume to obtain a three-dimensional map of the object-to-be-imaged. The basic principles of image reconstruction can again be understood similarly for CT and iCT. However, differences arise in the handling of the binned x-ray CT data and the list-mode data obtained from iCT.

### 2.5.1 Tomographic equation

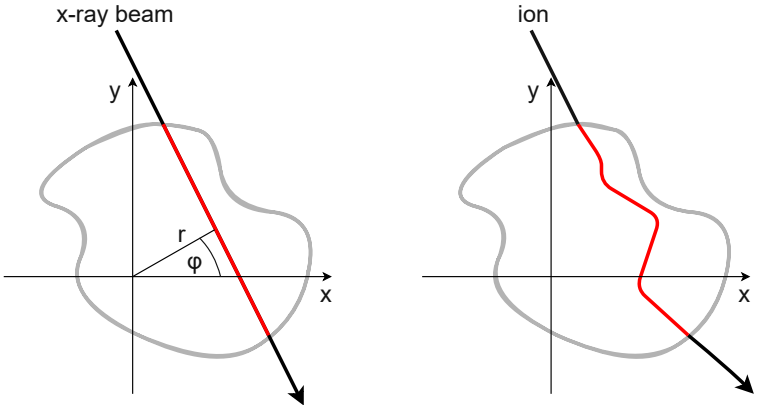


Figure 2.5.1: Schematic representation of the radon transform for x-ray CT (left). An x-ray beam passes through an object (in gray) on a straight line. For iCT (right), this simple line integral is not an accurate representation of the actual ion path. Hence, a definition for the tomographic equation, which incorporates the ion path estimate, is needed. Figure based on Birkfellner [50].

In the following, imaging principles are explained in two dimensions (imaging in a 2D plane) for simplicity. Of course, the very same principles are also applied to the orthogonal plane in a real imaging setup. If an x-ray beam passes through a medium on the path $r$, it is continuously attenuated according to Lambert-Beer's law (see equation (2.3.1)) depending on the object's linear attenuation coefficients $\mu_k$. In two dimensions, the path $r$ can be described by the coordinates $x$ and $y$ in the imaging plane and the angle $\varphi$ between a fixed coordinate system and the incoming beam's direction [50]

$$r = x\cos\varphi + y\sin\varphi. \tag{2.5.1}$$

This process is schematically displayed in figure 2.5.1. The line integral along this straight line is referred to as Radon transform [50]

$$R(\varphi, r) = \int_{r=\binom{x}{y}\cdot\binom{\cos\varphi}{\sin\varphi}} \mu(x, y)ds, \tag{2.5.2}$$

with the linear attenuation coefficient $\mu(x, y)$ replacing the general material function $f(x, y)$ mentioned in the introduction of this chapter. When it comes to ion imaging, single particle tracks have to be considered instead of bundled beams. As discussed in section 2.4, a SL can no longer be used as an accurate estimate of ion paths, which makes the representation of equation (2.5.1) inapplicable for iCT. The integration for each ion is hence done along the specific ion path estimate. As the material-specific quantity, the SP replaces the linear

attenuation coefficient from x-ray imaging, giving the projection value (ray sum) $p_i$ for an ion $i$ [60]

$$p_i = \int_{\text{path}} S(x, y, E_{\text{init}})\, ds \approx - \int_{E_{\text{init}}}^{E_{\text{out}}} \Big[ S(H2O) \Big]_{E}^{E_{\text{init}}} \mathrm{d}E. \tag{2.5.3}$$

The right side of equation (2.5.3) shows that the integration along the ion path can also be written as an integration over the ion's energy loss within the medium. The integrand on the right side of equation (2.5.3) stands for the ratio of the mass SPs at the initial ion energy $E_{\text{init}}$ and an arbitrary ion energy $E$ at $(x, y)$ in water,

$$\Big[ S(H2O) \Big]_{E}^{E_{\text{init}}} = \frac{\frac{S}{\rho}(x, y, E_{\text{init}})}{\frac{S}{\rho}(x, y, E)}. \tag{2.5.4}$$

Water can be used as reference material, as the fraction of the mass SPs is not strongly depending on the material [60, 61]. For a set of $M$ ions and $N$ pixels, the right side of equation (2.5.3) can be further discretized [60], yielding

$$p_i = \int_{\text{path}} S(x, y, E_{\text{init}})\, ds = \sum_{j=1}^{N} w_{ij} S_j(E_{\text{init}}), \quad i = 1, ..., M, \tag{2.5.5}$$

where $w_{i,j}$ corresponds to the intersection length of the ion $i$'s path estimate with the $j^{\text{th}}$ pixel.

For x-rays, the information obtained in the imaging corresponds to Radon transforms at multiple angles and radii that can be displayed in an image in the $(r, \varphi)$-plane, which is referred to as a sinogram. As ions do not follow the same scheme due to their curved path estimates, a sinogram representation usually is not reasonable (SL approach for the ion path needed) or feasible (the path is not described with a SL and only one angle $\varphi$). Instead, the data is stored in 'lists', so they are referred to as list-mode data. The following sections explain methods to use these data in the so-called backprojection to obtain a 3D image.

### 2.5.2 Direct reconstruction

The most popular direct reconstruction technique for x-ray CT is the filtered backprojection (FBP), which connects the Fourier transform with the Radon transform, as elaborated in Birkfellner [50]. The idea originates from Bracewell and Riddle [62] and was adapted for cone-beam CT (CBCT) by Feldkamp et al. [63]. According to Bracewell and Riddle [62], the original material function $f(x, y)$ can be found from

$$f(x, y) = \frac{1}{2\pi} \int_0^{\pi} \left[ \frac{1}{\sqrt{2\pi}} \int_{-\infty}^{\infty} \widehat{R_f(\varphi, \ \cdot \ )}(r) |r| \exp^{\mathrm{i}r \binom{\cos\varphi}{\sin\varphi} \binom{x}{y}} dr \right] d\varphi, \tag{2.5.6}$$

where the term in the square brackets refers to the inverse Fourier transform of $\widehat{R_f(\varphi, \ \cdot \ )}(r)|r|$ (see equation (2.5.2)) evaluated at $t$, which is defined as the straight line $x \cos\varphi + y \sin\varphi$ (cf. equation (2.5.1)) [50]. This can be interpreted as a filtering operation of $R_f(\varphi, r)$ with a fixed value of $\varphi$ using a filter with a frequency response of $|r|$ (ramp filter or Ram-Lak filter [64]). In a simplified notation, this can be written as the sum of $R_f(\varphi, \ \cdot \ ) * \text{ramp}$ over all possible $t_i$ [50]

$$f(x, y) \approx \frac{1}{2\pi} \sum_i (R_f(\varphi_i, \ \cdot \ ) * \text{ramp})(t_i). \tag{2.5.7}$$

The notation $R_f(\varphi, \ \cdot \ )$ indicates that the value of $\varphi$ is fixed, while $t$ is varied. As already discussed, the straight trajectory $t$ leads to problems in iCT image reconstruction. However, a well-known solution to adapt the FBP for iCT was developed and described by Rit et al. [65] for a cone-beam geometry (hence, using the adapted version of Feldkamp et al. [63] as

a basis). In their approach, virtual ion radiographs are created at various depths through the imaged volume, incorporating the path estimates of each ion contributing to the image. Such a radiography $g_{j,p}(w)$, which was binned at position $w$ in the original beam direction, can be written as

$$g_{j,p}(w) = \frac{\sum_{i \epsilon \mathrm{I}_p} h_j(u_i(w), v_i(w)) G(E_i^{\mathrm{in}}, E_i^{\mathrm{out}})}{\sum_{i \epsilon \mathrm{I}_p} h_j(u_i(w), v_i(w)}, \tag{2.5.8}$$

where $G$ corresponds to the integral described in equation (2.5.3) and $u$ and $v$ correspond to the distance between the pixel $j$ an ion $i$ is assigned to and the beam source. $h_j$ corresponds to a delta function, which equals one if the MLP of an ion went through a pixel $j$ and zero otherwise. $\mathrm{I}_p$ corresponds to the set of protons emitted from the same source position $a_p$ (projection angle for cone-beam iCT) [65].

In a voxel-specific backprojection, the $p = \{1, ..., P\}$ filtered projections acquired at the same source position are used to evaluate the RSP at a position $x$ with respect to the centre of rotation $o$:

$$\mathrm{RSP}(x) = \sum_{p \epsilon \mathrm{P}} \Delta\theta_p \left( \frac{\|o - a_p\|_2}{w(a_p, x)} \right)^2 \times \tilde{g}_p(u(a_p, x), v(a_p, x), w(a_p, x)), \tag{2.5.9}$$

with the angle weighting $\Delta\theta_p$. The approach is very similar to the standard Feldkamp-Davis-Kress (FDK) algorithm, but uses 3D projection images instead of 2D projection images.

An alternative approach for direct iCT reconstruction was given by Poludniowski et al. [66]. Instead of filtering and backprojecting the ion data, which was binned at various depths, their approach follows the opposing way: ray-projections are sampled through a 2D slice and backprojected through a 2D reconstruction matrix which is afterwards filtered with a 2D kernel (done for each measurement angle) [66].

### 2.5.3 Iterative reconstruction

The Radon transform for x-ray CT (equation (2.5.2)) and the projection values for iCT (equation (2.5.3)) can be interpreted as the solution of a set of linear equations [50, 67]

$$Ax = b. \tag{2.5.10}$$

For x-ray CT, the sparse system matrix $A$ describes the intersection of the x-rays with the pixels of the reconstructed phantom slice (or voxels of the reconstructed volume, if the problem is described in 3D) [68]. For $k$ measurement angles and $n$ parallel beams, the dimension of the system matrix, which is obtained from the scanner geometry, becomes $(k \times n) \times (n \times n)$. The vector $b$ corresponds to the measured Radon transforms and $x$ is the unknown vector containing the linear attenuation coefficients $\mu_i$ of the object-to-be-imaged [50]. Similarly, for iCT, the system matrix $A$ describes the intersection length of an ion $i$ with a pixel $j$ of the 2D phantom slice to reconstruct, which results in matrix dimensions of $I \times J$ for a total of $I$ protons and $J$ pixels. As for CT, the problem can be trivially extended to three dimensions. The vector $b$ in equation (2.5.10) now corresponds to the WEPL measurement for each ion contributing to the imaging process, whereas $x$ corresponds to the vector containing the unknown material RSPs [67]. Deriving from the imaging principles introduced in section 2.3.2, $A$ and $b$ are obtained from the tracker system and the calorimeter/range telescope, respectively.

Multiple approaches to iteratively solve the set of linear equations for CT [69–71] and iCT [67] were developed. Two algorithms families are discussed in more detail within this section, as they are used for image reconstructions throughout this thesis. The first algorithm family is the simultaneous algebraic reconstruction technique (SART)-type family, where the original SART algorithm was defined by Andersen and Kak [72]. Algorithms of these families follow the general equation

$$x^{k+1} = x^k + \lambda_k V A^T W (b - A x^k), \tag{2.5.11}$$

to generate an image estimate $x^{k+1}$ from a prior guess $x^k$ [68]. As initial guess $x^0$, any arbitrary image can be used (trivial case: empty image). $V$ and $W$ are weight matrices, which, in case of x-ray CT, depend on the ray length or, in case of iCT, on the intersection length of the path estimate with a specific pixel/voxel. The parameter $\lambda_k$ corresponds to a relaxation parameter. The algorithm is used with blocks ('subsets'), which consist of image projection rays from a single angle [67].

Instead of using subsets from a single projection angle, so-called 'ordered subsets', as proposed by Wang and Jiang [73] in their ordered subsets SART (OS-SART), can be used. The basic idea is to split up equation (2.5.10) into subsets and apply the SART methodology to each of these subsets [67]. The algorithm can be written as [67]

$$x^{k+1} = x^k + \lambda_k \left( \frac{1}{\sum_{i \in B_{t(k)}} a^i_j} \right) \sum_{i \in B_{t(k)}} \frac{b_i - \langle a^i, x^k \rangle}{\sum_{l=1}^{J} a^i_l} a^i_j, \tag{2.5.12}$$

where $B_t$ is a subset of indices $\subseteq \{1, 2, ..., I\}$. In total, $T$ subsets $B_t = \{i^t_1, ..., i^t_{n(t)}\}$ with $n(t)$ elements are used in a way, that each element in $\{1, 2, ..., I\}$ appears at least in one subset [67]. In equation (2.5.12), $a^i_j$ stands for the matrix elements of $A$. In contrast to SART, where the image is updated projection per projection, OS-SART uses a whole subset of projections when updating the image [68].

The second algorithm family to be discussed within this thesis is the total variation regularization family, which is often used in CT as the total variation norm constrains the resulting image to be piece-wise smooth [68]. Algorithms of this family first minimize the input data by using an algorithm from another family (e.g., SART-type family) and then minimize the total variation (noise) of the resulting image. Hence, a double optimization of the problem is performed, which leads to more tuning parameters of the algorithms [68]. One algorithm of this family is the adaptive-steepest-descent-projection onto convex sets (ASD-POCS) [74], which especially performs well with limited projection data. The algorithm exploits the algebraic reconstruction technique (ART) for data consistency and basic projection enforces positivity (which is referred to as projection onto convex sets (POCS)) [74]. The ART was described in 1970 by Gordon et al. [75] for x-ray CT and can be written as [76, 77]

$$x^{k+1} = x^k + \lambda_k \frac{b_i - \langle a^i, x^k \rangle}{||a^i||_2^2} a^i_j. \tag{2.5.13}$$

Other algorithms of the total variation regularization family (e.g., SART total variation) are known for their good reconstruction performance for noisy input data in CT [68].

## 2.6 Other ion imaging modalities

Besides conventional ion radiography (iRad) or iCT (see section 2.3.2), which use the ions' energy loss as contrast-defining quantity in the resulting image, other imaging modalities with ions are also possible. While using the large-angle elastic scattering of ions with atomic nuclei would require large detectors or detector offsets [78, 79], other imaging techniques allow using an iCT setup without further modification. Two of these, namely MCS imaging and attenuation imaging (also referred to as fluence loss imaging), are briefly discussed in the following sections. Both of these imaging modalities solely depend on the tracking information of the ions. Hence, no calorimeter or range telescope is needed.

### 2.6.1 Imaging based on multiple Coulomb scattering

As discussed in section 2.1.2, ions are subject to MCS when they interact with matter. For thin absorbers, this results in the already mentioned Highland formula, given for protons in equation (2.1.8). Measuring $\theta_0$ can be used for creating radiographic images, as it was demonstrated for electrons in Jansen and Schütze [80] and for protons in Plautz et al. [81], Ulrich-Pur et al. [82], and Kaser et al. [83] where the latter results are shown in detail in section 4.3.2. For a full scattering iCT, Krah et al. [84] extended the principle and introduced the so-called scattering power analogous to the stopping power as

$$T(z) = \frac{dA}{dz}, \tag{2.6.1}$$

where $A$ corresponds to the variance $\langle\sigma\rangle^2$ of the scattering distribution at a certain depth $z$. With further investigation [84], it is found that the scattering power can be written as a function $\tau$ depending on $A(z)$ and the radiation length $X_0$ of the traversed material within a depth $z$ (see equation (2.1.9)). Similar to the RSP, the relative scattering power can then be defined as [84]

$$\delta(X_0(z), A(z)) = \frac{\tau(X_0(z), A(z))}{\tau_\mathrm{w}(A)}, \tag{2.6.2}$$

with the scattering power in water $\tau_\mathrm{w}$. Finally, the projection value $G$ obtained for each ion $i$ from the tracker measurements is given by [84]

$$G(A_{\mathrm{out},i}) = \int_0^{A_{\mathrm{out},i}} \frac{1}{\tau(w)} \mathrm{d}A = \int_{\vec{\Gamma}_i} \delta(\vec{\Gamma}_i(w)) \mathrm{d}w, \tag{2.6.3}$$

which depends on the path estimate $\vec{\Gamma}_i$, analogous to equation (2.5.3) for conventional iCT. To solve this equation for the relative scattering power, again an adequate iCT reconstruction algorithm such a FBP using distance-driven binning (section 2.5.2) can be used. Again, the projection values are binned in radiographs at multiple phantom depths $w$. This corresponds to the binning process described by equation (2.5.8) but using equation (2.6.3) instead of $G(E_i^\mathrm{in}, E_i^\mathrm{out})$.

### 2.6.2 Attenuation imaging

An ion beam traversing a medium can be characterized by its fluence, which corresponds to the number of ions $\mathrm{d}N$ passing an area element $\mathrm{d}A$ orthogonal to the beam direction. In matter, the initial fluence $\phi_\mathrm{in}$ is attenuated due to inelastic interactions of the ions with the atomic nuclei of the target material. This attenuation follows an exponential law [22] (see section 2.1.3)

$$\phi_\mathrm{out} = \phi_\mathrm{in} \exp\left(-\int_{w_\mathrm{in}}^{w_\mathrm{out}} \kappa(\vec{\Gamma}(w)) \mathrm{d}\vec{\Gamma}(w)\right), \tag{2.6.4}$$

where, similar to the Lambert-Beer law in equation (2.3.1), the ions within a beam are assumed to travel along the same path $\vec{\Gamma}$. The resulting fluence $\phi_\mathrm{out}$ depends on the linear inelastic nuclear cross-section $\kappa$. For each pixel $j$ in a radiograph, a projection value $g_j$ can be found by solving equation (2.6.4) for the integral over $\kappa$ [22]

$$\int_{w_\mathrm{in}}^{w_\mathrm{out}} \kappa(\vec{\Gamma}(w)) \mathrm{d}\vec{\Gamma}(w) = -\ln \frac{\phi_\mathrm{out}^j}{\phi_\mathrm{in}^j} \equiv g_j, \tag{2.6.5}$$

with pixel-specific initial and exit fluences $\phi_\mathrm{in}^j$ and $\phi_\mathrm{out}^j$. To incorporate a MLP estimate for each particular ion, Quiñones et al. [22] added a third dimension to equation (2.6.5) in a way that depth-specific $\phi_\mathrm{out}^j = \phi_\mathrm{out}^j(w)$ result in multiple distance-driven radiographs $g_j(w)$

that can be used with the modified FBP algorithm described in section 2.5.2. Attenuation radiographs obtained with an iCT demonstrator [85] are presented in section (4.3.3).

# CHAPTER 3

# Software tools

In this chapter, an introduction to the software toolkits used in the scope of this thesis is given. Section 3.1 outlines the Corryvreckan framework that was applied to test beam data measured at MedAustron. While section 3.2 focuses on mechanisms for data generation with Monte Carlo toolkits, section 3.3 gives a short introduction to the data format used for the simulation output. Section 3.4 introduces the compute unified device architecture (CUDA) application programming interface (API) and the tomographic iterative GPU-based reconstruction (TIGRE) toolbox that was used to generate 3D images from simulated or measured iCT data within the scope of this work.

## 3.1 Corryvreckan

Corryvreckan [86] is an open-source software tool for track reconstruction and analysis of test beam data. It is a modular framework written in C++ which simplifies the process of adapting or adding custom code. The software is invoked via the command-line by submitting a configuration file in which the track reconstruction and analysis chain (modules) to be applied is defined. Furthermore, a geometry file defines the specifics of the test beam setup (such as positions and orientations of detectors).

In the main configuration file, the detector-specific *EventLoader* modules are used to decode raw data from pixel or strip detectors. The very first module to be invoked defines the chunk of data to be processed (explicitly given by time stamps or trigger numbers), which is taken over by the subsequent modules in the given analysis chain. *Clustering* modules based on closest-neighbor search or timing information allow finding hit positions on the detectors (arithmetic mean for binary information and charge-weighted center of gravity if the charge information is available). *Tracking* modules enable finding and modelling particle tracks. Here, the module *TrackingMultiplet* is defined to specifically find particle trajectories in different arms of a beam telescope (such as the tracker of the iCT demonstrator) [86].

An important feature embedded in the Corryvreckan framework is the alignment procedure, which consists of two steps (pre-alignment and alignment). Both steps produce an updated geometry file, which contains detector rotations and offsets with regard to a reference plane (in case of the iCT demonstrator, the first tracker plane was regarded as fixed) [86].

## 3.2 Monte Carlo toolkits for particle transport in matter

Monte Carlo simulations are a convenient and useful tool for the modelling of particle transport in matter and are used to complement or prepare real experiments. Random sampling is applied in order to set up a stochastic model for the solution of the physical problem [87]. When passing through an object, one particle is potentially subject to $n$ independent interaction mechanisms $I_1, ..., I_n$, which occur with respective possibilities $p_1, ..., p_n$ so that

$$\sum_n p_i = 1. \tag{3.2.1}$$

An adequate algorithm is used to generate a random number $x$ from the interval [0,1) so that

$$\sum_{1 \le x \le i-1} p_i \le x < \sum_{1 \le x \le i} p_i. \tag{3.2.2}$$

Hence, $x$ may be used to determine one specific interaction process $I_i$. For the principle to work, it must be guaranteed that the random numbers are evenly distributed over the given interval and independent of one another. Given that all possible interaction types can be summarized in one total cross-section $\sigma_t$, the probability $p_i$ for the interaction $I_i$ can be defined via the respective cross-section $\sigma_i$ [87]

$$p_i = \frac{\sigma_i}{\sigma_t}. \tag{3.2.3}$$

These principles are exploited in Monte Carlo toolkits such as Geant4 [88] or its implementations for clinically related research, GATE [31, 89] or TOPAS [90].

### 3.2.1 Geant4

Geant4 [88] is an object-oriented, C++ based Monte Carlo simulation toolkit which was originally developed for high energy physics applications by KEK and CERN. The framework is organized in so-called class categories, where lower class categories (right in figure 3.2.1) are used by higher class categories (left in figure 3.2.1). In the figure, the square indicates that a class category uses the class assigned with the solid black line.

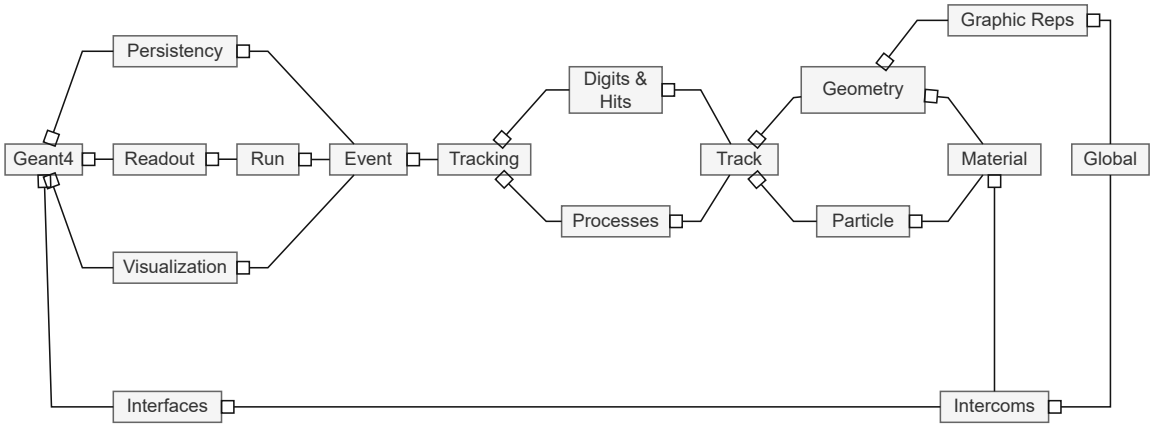


Figure 3.2.1: Top level categories of Geant4. The square indicates that the category uses the category connected via the solid black line. Figure based on Agostinelli et al. [88].

According to the description of Agostinelli et al. [88], the *global* class category handles the random numbers that are later used to define the physical process that is assigned to a particle at a certain point along its track. Furthermore, the class includes physical units, constants and numerics. The class categories *material*, *particle* and *geometry* are self-descriptive and

incorporate all facilities necessary to describe the particle type (e.g., mass and charge) and material/geometry of the object that the particle is propagating through. *Track* contains the tracks and steps of a particle, which are then again used by the *processes* and its implementations of physical models for particle interactions. Geant4 includes multiple physics lists for different particle physics applications (incorporating, for example, a more detailed interaction model for a certain energy range or particle type). All the priorly mentioned categories are invoked by *tracking*, which describes the further development of the particle track according to the given processes. If a volume is declared as *sensitive* in the simulation, *tracking* provides information about *digitization and hits*. Tracks resulting from one primary particle are bundled in an *event*, while all events from a common beam are collected in the class category *run*. *Interfaces*, *persistency* and *visualization* allow connecting Geant4 to outside facilities, while the *readout* class category handles pile-up of the generated data.

### 3.2.2 GATE

As Geant4 was primarily developed for high-energy physics applications, some more user-friendly implementations which do not require a strong programming background were developed for specific research areas. The aim of these frameworks is to allow for fast and easy-to-achieve results in a specific field of research without a deep knowledge of the original Geant4 class structure. One of them is the GATE [31], which encapsulates the Geant4 libraries in simple macro scripts for the user. The framework has a focus on positron emission tomography (PET) and single-photon emission computed tomography (SPECT) applications, however, this imaging focus also makes the tool applicable for iCT. For example, the tool allows importing a CT image as a voxelized phantom and converting the CT numbers (HUs) to materials/tissues via an implemented conversion table [91].

## 3.3 ROOT

ROOT [92] is an object-oriented data analysis framework that was developed in the scope of particle experiments at the large hadron collider (LHC), where the obtained large data sets showed the limits of the existing FORTRAN-based libraries. The framework is written in C++ and offers various tool for data analysis such as fitting, visualization or data binning in histograms. As ROOT is designed in a modular fashion, the user is able to adapt or extend the framework to his/her specific needs [92].

The framework provides a data structure allowing to store large amounts of data in a strongly compressed way. One main component of this structure is referred to as *ROOT-tree*, an object which contains a high number of same-class elements, allowing for efficient compression in contrast to individually memorized objects. Furthermore, the object allows for fast data access [93].

Within this thesis, the ROOT data format was chosen as the output file format for simulations performed in Geant4 and GATE and for storing the data analyses from Corryvreckan that were obtained from the iCT demonstrator data.

## 3.4 TIGRE toolbox

Over the past years, many image reconstruction and processing frameworks or codes for tomographic imaging, such as ASTRA [94], the python package scikit-image [95], STIR [96], RTK [97], or Gadgetron [98] were developed. Furthermore, a few specific codes for iCT [99–101] evolved, either as a stand-alone tool or to be used as additional code for an existing framework. For CT and iCT, not only a fast reconstruction but also a user-friendly implementation is crucial, especially when the cooperation of multiple disciplines is essential. For example, in using or improving tomographic imaging, the fields of medicine, biology, physics,

math, informatics, and others may contribute, which typically come along with a different depth of knowledge of programming. In that context, the TIGRE toolbox [68] was developed for CBCT (but it also allows for a parallel-beam geomtery).

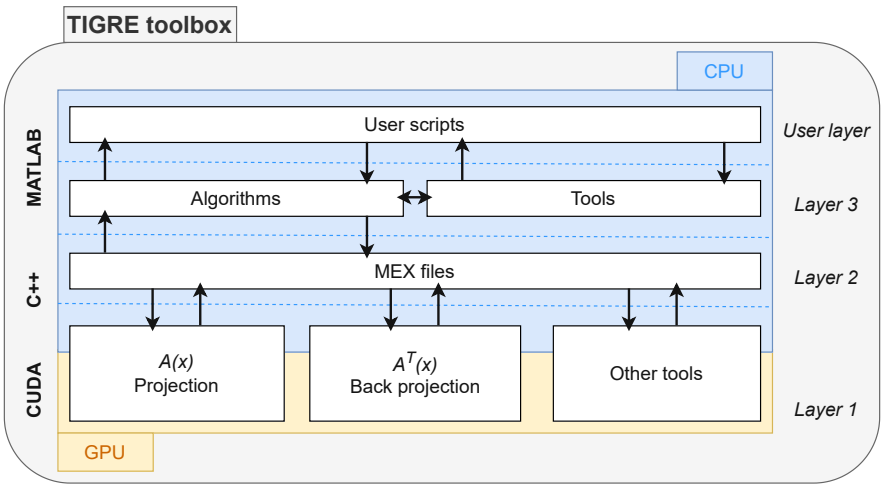


Figure 3.4.1: Structure of the TIGRE toolbox. Figure based on Biguri et al. [68].

While the computationally expensive parts of the toolbox are written in CUDA (hence they run on a graphics processing unit (GPU), see section 3.4.1), the user can invoke these operations with simple MATLAB scripts. This principle is visualized in figure 3.4.1: the top layer is referred to as the user layer, which contains the scripts that invoke the algorithms or image processing tools implemented in the toolbox. Again, algorithms and tools are implemented in MATLAB, intended to make adapting and adding other algorithms easier. As discussed in section 2.5.3, iterative reconstruction algorithms aim at solving a matrix equation of the form $Ax = b$. Therefore, two operations are needed: a forward projection $A$ and a back projection $A^T$ are performed to refine the resulting vector $x$. These operators are implemented in CUDA in the TIGRE toolbox. The MATLAB-based algorithms communicate via C++ *MEX files* with this basic layer of the framework [68].

As the toolbox was developed for CBCT, the projection and back projection as implemented in the toolbox correspond to operations along straight lines (matching with straight-line x-ray beams).

The toolbox incorporates reconstruction algorithms from four different families. Although the focus of lies on iterative image reconstruction, the FBP and its pendant for cone-beam geometries, the FDK algorithm (see chapter 2.5.2), are implemented. From the type of SART algorithms (see section 2.5.3), three algorithms are part of the toolbox: simultaneous iterations reconstruction technique (SIRT) (uses all projections at once), SART and OS-SART. Another algorithm family incorporated in the toolbox are the Krylov subspace methods, where the conjugate gradient least squares (CGLS) [102] was added. Finally, multiple algorithms from the total variation regularization family, such as ASD-POCS (see section 2.5.3), are implemented [68].

### 3.4.1 General purpose computation on a GPU

The rising demand for computational power in research and industry over the last years has lead to major developments in the field of computer technology. Besides the continuous downsizing of transistor sizes (*Moore's law*), developments on different computer architectures were carried out. These include the advance of two architectures: high performance computers (HPCs) and GPUs. While HPCs refer to large-scale clusters composed of numerous computing units (typically high in cost and maintenance effort), GPUs were developed in the scope of graphics and visualization requirements in personal computers (PCs) and

especially pushed by the video game industry. Designed after the need of video games, GPUs offer hundreds of low power and speed processors able to handle a large amount of simple arithmetic calculations with fast memory access. These developments also showed advantages for the demands of research and industry, where the term general purpose computation on a graphics processing unit (GPGPU) was introduced [103].

The main GPU architecture is displayed in figure 3.4.2. It consists of $n$ multiple stream multiprocessors, where each assigns the instructions to the $m$ stream processors it includes. A stream processor then runs a so-called *block* of instructions, which consists of multiple *threads*. Per definition, blocks run the exactly same algorithm (*kernel*). Each thread has access to a thread-specific register memory, where local variables are stored (small of size). Furthermore, the stream processors within one multiprocessor have access to a shared memory, which is also fast in access, but slower than register memory. The largest but also the slowest memory type on the GPU is the device random-access memory (DRAM). It is typically used to store results or to allocate memory before a kernel call - however, large data sets often force using this memory type within a kernel. On each stream multiprocessor, memory cache is available, which allows for faster communication with the threads than DRAM and is designed to improve the execution of memory coalescing warps (i.e., combining the access to global memory from multiple threads at the same time into one single access) [103].

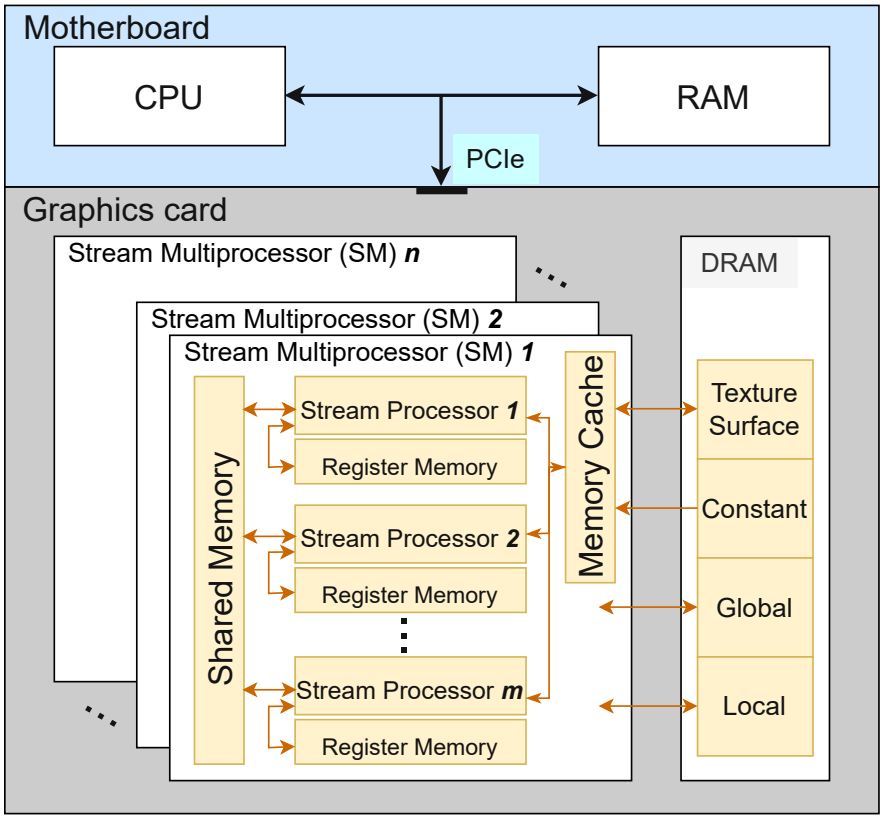


Figure 3.4.2: Basic architecture of a GPU. Figure based on Biguri [103].

Finally, GPU and central processing unit (CPU) communicate via the peripheral component interconnect (PCI) express [103].

To exploit the structure of a GPU, CUDA [104] was developed by NVIDIA. It is an API that allows to run parts of a program on a supported GPU using the high number of independent parallel threads. With CUDA-specific terminology, the functions of a user-written script are either run on the CPU or invoking a kernel. Besides CUDA, other APIs like OpenGL [105] or DirectCompute also allow running calculations on a GPU.

# CHAPTER 4

## Radiographic ion imaging with an ion CT demonstrator setup

In the following sections, an overview of the technologies and hardware parts used for ion imaging by the Institute of High Energy Physics (HEPHY) and the Technische Universität Wien (TU Wien) is given. Experimental results from an ion computed tomography (iCT) demonstrator, including the imaging modalities discussed in sections 2.3.2 and 2.6 are presented in section 4.3. While in this chapter, only radiographic images are presented, a full iCT scan obtained from the demonstrator system, will be presented in section 5.3 of the preceding chapter. The work presented in this chapter was done in collaboration or built upon the work presented in Burker [106] and Ulrich-Pur [107].

## 4.1 MedAustron facility

MedAustron [40, 108] is a centre for ion-beam therapy with protons and carbon ions based on synchrotron technology (see section 2.2). The facility is located in Wiener Neustadt, which is approximately 50 km south of Austria's capital Vienna. Three irradiation rooms (IRs) are available for patient treatment, which started in 2016. Proton energies up to 250 MeV and carbon ion energies up to 400 MeV/u are available in these treatment rooms [108]. Furthermore, a fourth beam line is provided exclusively for non-clinical research. This beam line offers the same maximum energy for carbon ion beams as the treatment rooms, but proton energies up to 800 MeV are available [108]. The facility is schematically represented in figure 4.1.1, where IR 1 represents the room for non-clinical research.

The accelerator complex was optimized for medical applications, which incorporates particle rates in the order of $10^8$ to $10^9$ particles per second [108, 110]. Although, theoretically, the accelerator design would allow reducing the particle rate to the order of $10^6$ particles per second [111], physics experiments like iCT test runs often require even lower rates [109]. Therefore, Ulrich-Pur et al. [109] established and commissioned three particle flux settings for seven proton beam energies below 252.7 MeV (ranging from $\approx 2.4 \times 10^3$ particles per second to $\approx 5.2 \times 10^6$ particles per second). Additionally, three low flux settings were commissioned for a proton energy of 800 MeV (ranging from $\approx 2 \times 10^3$ particles per second to $\approx 1.3 \times 10^6$ particles per second).

## 4.2 Ion CT demonstrator setup

An iCT demonstrator was built by TU Wien and HEPHY and tested at the MedAustron facility [112, 113]. The demonstrator was intended to be a preliminary experimental setup

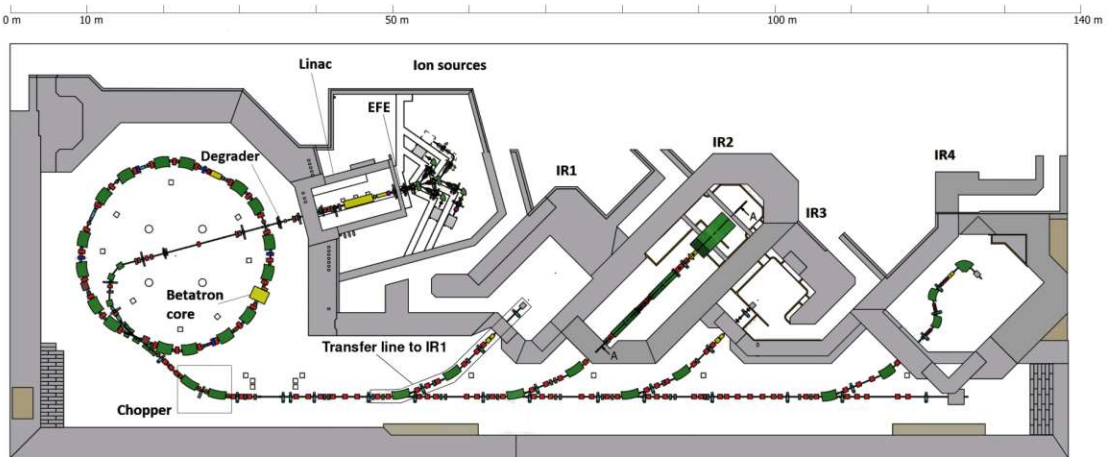


Figure 4.1.1: Schematic representation of the MedAustron accelerator complex. Figure from Ulrich-Pur et al. [109].

for iCT measurements. The findings of the demonstrator should be used to define the requirements for a system of clinically relevant size. As schematically displayed in figure 4.2.1, the setup consists of four double-sided silicon strip detectors (DSSDs), two of which are used as upstream and two as downstream tracker. In the very first implementation of the demonstrator [82], six detector modules were used (three for the upstream tracker and three for the downstream tracker, respectively). This allowed to measure a particle track even if one module did not record a detector hit (e.g., in the case of noisy strips). However, the additional material budget leads to a higher amount of multiple Coulomb scattering (MCS) which affects the beam and, hence, the resulting image. For this reason, the additional modules were finally removed from the demonstrator.

Each sensor has an active area of 2.56 cm × 5.12 cm and a thickness of 300 µm. The n-side ($x$-coordinate) has a pitch of 100 µm and the p-side ($y$-coordinate) a pitch of 50 µm [112, 113]. The Gigabit Ethernet readout system, that was newly implemented for the tracker, allows for a data acquisition (DAQ) of up to 30 kHz [113].

Between the upstream and downstream tracker, a motorized rotating table was installed. This allows to rotate the phantom in steps of 1.8° instead of moving the whole setup around the phantom.

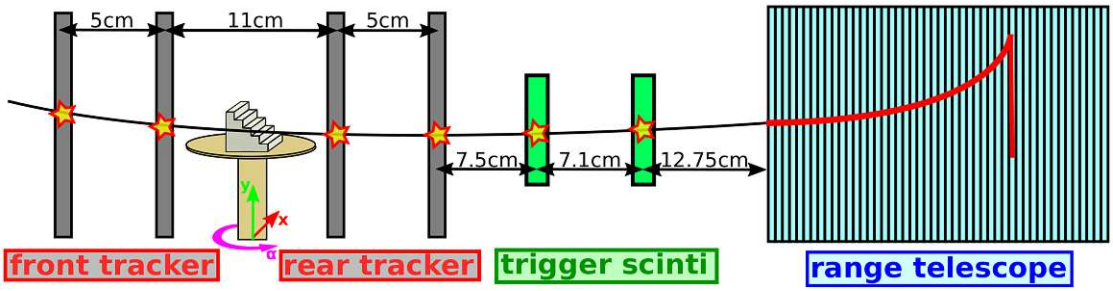


Figure 4.2.1: Schematic representation of the iCT demonstrator. Figure from Ulrich-Pur et al. [113].

As a range telescope, the proton range radiography system (PRR30), which was formerly developed by the TERA foundation [114], was used. In contrast to a calorimeter, which measures an ion's residual energy, a range telescope directly returns the water-equivalent thickness (WET) of an ion. The range telescope consists of 42 scintillator slices with an active area of 30 cm × 30 cm [113]. The data readout was done via USB, resulting in a DAQ rate < 1 MHz. Synchronization between tracker and range telescope was performed with

the AIDA2020 trigger and logic unit (TLU) [115], using two 5 cm × 5 cm × 1 cm plastic trigger scintillators [113], which were located between the downstream tracker and the PRR30. Each scintillator corresponds to 1.549 cm of G4_PLASTIC_SC_VINYLTOLUENE in Geant4 (density of 1.032 g/cm$^3$). The setup allowed for a total DAQ of approximately 900 iCT events per second.

A photo of the demonstrator as installed at the MedAustron facility can be found in figure 4.2.2, where the phantom area is highlighted.

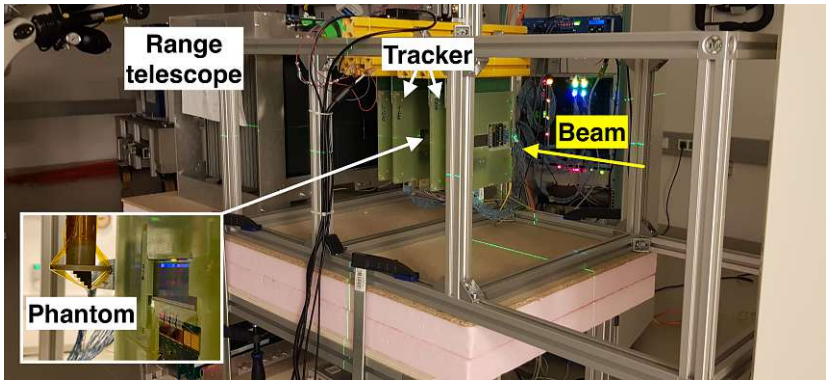


Figure 4.2.2: Photo of the iCT demonstrator (the image of the phantom corresponds to an adapted version of Ulrich-Pur et al. [113]).

### 4.2.1 Phantoms

The phantom size to be investigated with the demonstrator is limited due to the size of the tracking modules. While first experiments with the demonstrator incorporated phantoms such as a mounting hub [112] or a custom phantom with multiple cut-outs [82], a simpler phantom shape was used in recent measurements [83, 113].

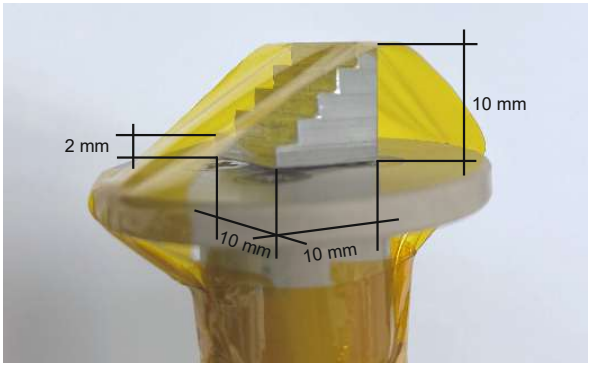


Figure 4.2.3: Aluminium phantom used for experiments with the iCT demonstrator. The phantom is mounted on the rotational table with Kapton tape.

The phantoms investigated within the scope of this thesis correspond to a stair profile as displayed in figure 4.2.3. The total length of the profile is 10 mm, while each stair has a length of 2 mm (five stairs in total). As phantom materials, aluminium and polymethylmethacrylat (PMMA) were chosen.

## 4.3 Results

The following sections present radiographic images that were measured with the iCT demonstrator. All imaging modalities, that were studied with the demonstrator, were commonly

investigated with protons. Theoretically, the presented imaging techniques could also be studied with carbon ions, as they are available at the IR 1 of MedAustron. However, low flux settings as for protons would have to be commissioned for these particles. Furthermore, as seen in section 2.2, these ions strongly suffer from fragmentation, leading to a decrease in the beam fluence and artefacts in the resulting image, if the fragments are not correctly filtered in the data set. This was shown, for example, for helium ions in Volz et al. [13]. Nevertheless, imaging with helium ions could be a suitable compromise for ion imaging in the future, as they show less fragmentation than carbon ions but, due to their higher mass, pass in more straight paths through matter than protons.

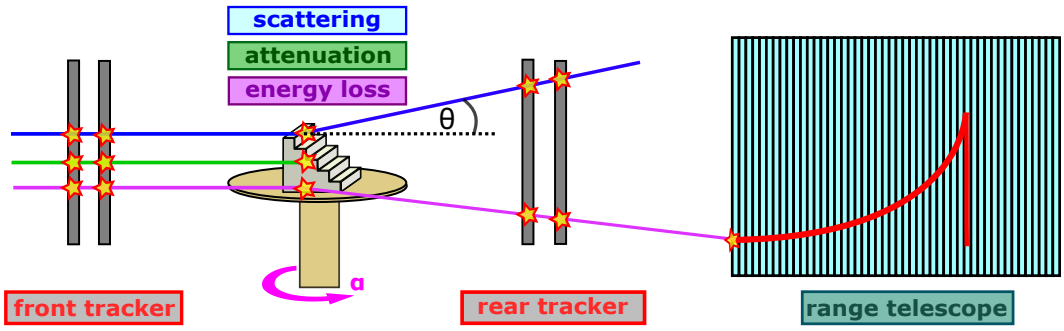


Figure 4.3.1: Schematic representation of imaging modalities that can be investigated with the iCT demonstrator. In this representation, the iCT scanner is displayed in a simplified version. For example, the trigger scintillators were removed from the sketch. Furthermore, the distance between the tracker planes and the phantom were adapted in the sketch to allow for a better representation of the imaging modalities.

Figure 4.3.1 displays all imaging modalities that were investigated with the iCT demonstrator. In contrast to figure 4.2.1, the trigger scintillators are not included in the sketch and the distances between the scanner elements were adapted to better visualize the physical effects that an ion can undergo when passing through a phantom. While an energy-loss ion radiography (iRad) or iCT (pink track) requires an additional calorimeter, images based on scattering and attenuation (blue and green tracks) require a tracker measurement only.

For all presented measurements with the demonstrator system, alignment was necessary to account for offsets or rotation of the modules forming the tracking system. Therefore, an empty imaging run (without phantom and rotational table) was measured. The data were then analyzed with Corryvreckan [86], a software tool for the analysis of test beam data (see section 3.1). In the analysis, the first detector was regarded as fixed (offset and rotation of zero). Track reconstruction from the proton data measured with all modules allowed for evaluating the rotation and offsets of the three further modules, which are then used to correct the particle hit positions in a general coordinate system.

### 4.3.1 Energy-loss radiography

The radiographs displayed in figure 4.3.2 were created from the same data set that was used in Ulrich-Pur et al. [113]. The spatial information is given by the tracker measurement, while the projection value is defined by the measurement of the range telescope (directly measuring the WET of each ion). In total, 80 proton radiographs (pRads) of the aluminium phantom were measured at a proton beam energy of 100.4 MeV. For each pRad, which incorporated approximately $5.5 \times 10^5$ protons on average, a mean measurement time of 24 min was needed. Actually, the data per radiography corresponded to approximately $2.5 \times 10^6$ proton events of raw data on average. However, this count was reduced due to synchronization and tracking inefficiencies [113].

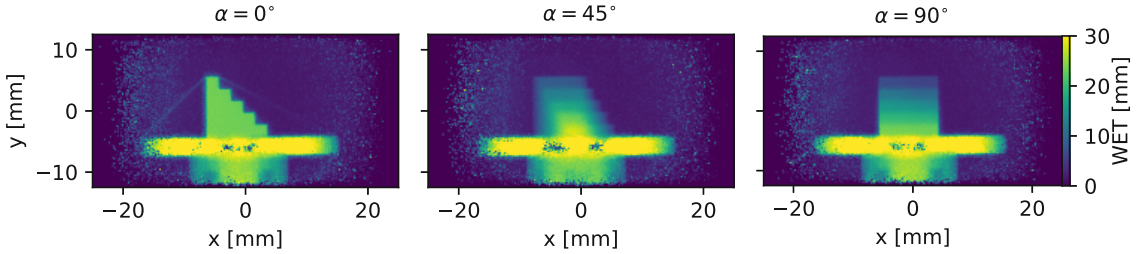


Figure 4.3.2: pRads measured at various rotation angles ($E_{\text{init}} = 100.4\,\text{MeV}$).

The data from the iCT demonstrator were processed with a C++ script and the WET values of the single protons were binned into 0.2 mm × 0.2 mm pixels using a straight line (SL) approach that will be discussed in detail in section 5. Due to the small phantom size, the SL path estimate allows distinguishing the phantom details in spite of the influence of MCS. The radiograph at 90° was analysed by exploiting the five different stair thicknesses (2 mm to 10 mm) in this front view. A region of interest (ROI) consisting of 25 × 4 pixels was defined in the centre of each phantom step. The average WET within this region was recorded and the background value (taken from a ROI outside the phantom area) was subtracted. The resulting value ($\text{WET}_{\text{measured}}$) was compared to a theoretical value ($\text{WET}_{\text{ref}}$) for each stair with a thickness $t_{\text{stair}}$, corresponding to equation

$$\text{WET}_{\text{ref}}(t_{\text{stair}}) \approx \int_0^{t_{\text{stair}}} \text{RSP}\, \mathrm{d}x, \tag{4.3.1}$$

where the relative stopping power (RSP) was assumed to have a fixed (energy-independent) value of ≈ 2.08, which was obtained from a reference simulation (R80 measurement, see section 5.1 for details). Furthermore, the relative error $\epsilon_{\text{rel}}$ of the measured WET was calculated using

$$\epsilon_{\text{WET}}(\%) = 100 \cdot \frac{\text{WET}_{\text{measured}} - \text{WET}_{\text{ref}}}{\text{WET}_{\text{ref}}}. \tag{4.3.2}$$

The results of this calculation can be found in table 4.1. For the thinnest stair (2 mm), a relative error of 2.3 % was recorded. For the other stairs, $\epsilon_{\text{WET}}$ was found to be below 7 % (peaking at 6.6 % for the 4 mm stair). For the 10 mm stair, the measured WET differed from its reference value by 2.2 %. A full analysis of the pRad data set is given in section 5.3, where all 80 proton radiographs were used to generate a 3D RSP map.

Table 4.1: Measured WET for each phantom stair in a pRad measured at a rotation of 90°.

| **Stair thickness [mm]** | **$\text{WET}_{\text{measured}}$ [mm]** | **$\text{WET}_{\text{ref}}$ [mm]** | **Rel. error [%]** |
|---|---|---|---|
| 2 | 4.26 | 4.16 | 2.3 |
| 4 | 8.86 | 8.32 | 6.6 |
| 6 | 13.25 | 12.48 | 6.2 |
| 8 | 17.48 | 16.64 | 5.1 |
| 10 | 21.25 | 20.80 | 2.2 |

### 4.3.2 Scattering radiography

The results discussed in this section were published in Kaser et al. [83]. Scattering imaging is an imaging technique which only relies on the measurement of the particle tracks - hence, the setup described in section 4.2 can be simplified by removing the range telescope. This

allows for higher DAQ rates as the synchronization step between tracker and range telescope is cancelled. Images were taken of the stair-shaped phantom described in section 4.2.1 using two different materials, namely aluminium and PMMA. For each material, a radiography was measured at two energies (100.4 MeV and 145.4 MeV) and at two phantom rotations (0° and 90°). For each radiography, roughly $10^7$ protons were used, with the measurement time varying between 15 min and 30 min.

For the data analysis, two modules (*TrackingMultiplet* and *AnalysisMaterialBudget*) of the Corryvreckan [86] framework were used. These modules return the average absolute deviation (AAD) of the kink angle distribution for each radiographic pixel. The kink angle corresponds to the angle between entry and exit direction of an ion, as calculated from the measured hit positions at the upstream and downstream trackers. The AAD can be assigned to $\theta_0$ using a scaling factor [80]. The $\mathrm{AAD}_{90}$, which corresponds to the AAD of the inner 90 % quantile obtained from the module *AnalysisMaterialBudget*, was used as a pixel value in the radiographic images. To convert this value to the width of the scattering distribution $\theta_0$, a scaling factor or 1.48 was determined in Kaser et al. [83].

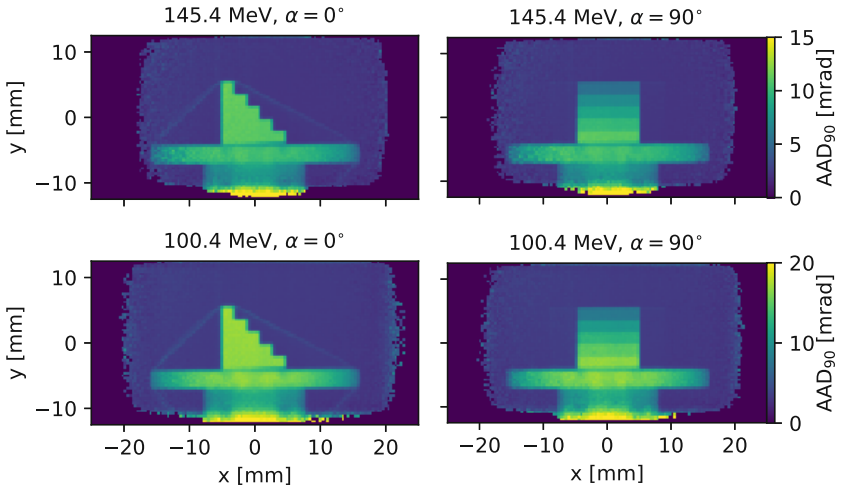


Figure 4.3.3: Scattering radiography results for 100.4 MeV and 145.4 MeV (aluminium phantom). Figure from Kaser et al. [83].

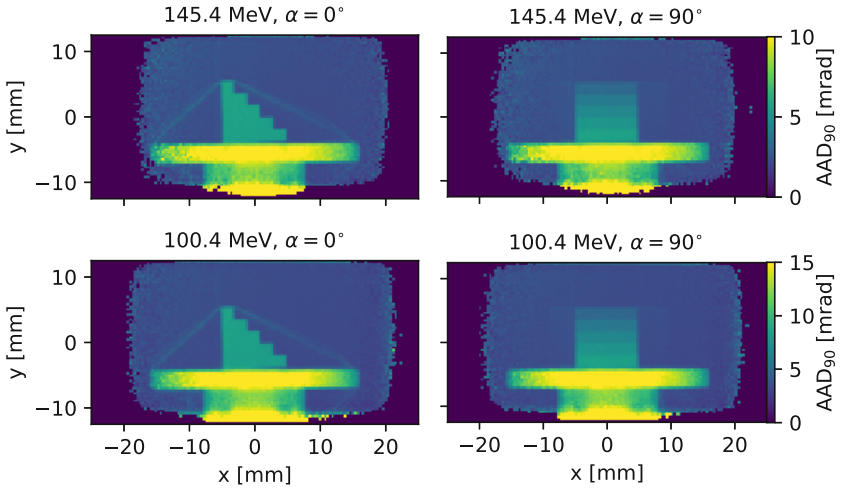


Figure 4.3.4: Scattering radiography results for 100.4 MeV and 145.4 MeV (PMMA phantom). Figure from Kaser et al. [83].

The measured radiographic images for the aluminium phantom and the PMMA phantom, as they were obtained after the analysis with Corryvreckan, are displayed in figure 4.3.3 and figure 4.3.4, respectively. The data binning was done in $0.4 \times 0.4$ mm$^2$ pixels in the centre of the phantom (isocentre) by following the initial and final particle direction on straight lines to this position. In all eight images, the phantom and the rotary table can be clearly distinguished from the background. Comparing the images at 100.4 MeV and 145.4 MeV, the slightly decreased beam spot size can be observed (full-width at half maximum (FWHM) of 14 mm and 10.2 mm, respectively). In the 0° images (corresponding to the side view of the phantom), all five stairs and even the Kapton tape, which mounts the phantom to the table, are visible. In the front views (90° images), the different shades again allow distinguishing between the five phantom stairs. As expected, aluminium shows a higher scattering effect than PMMA, hence yielding a higher AAD. The same effect can be seen for different energies: for lower energies, a larger scattering impact can be measured.

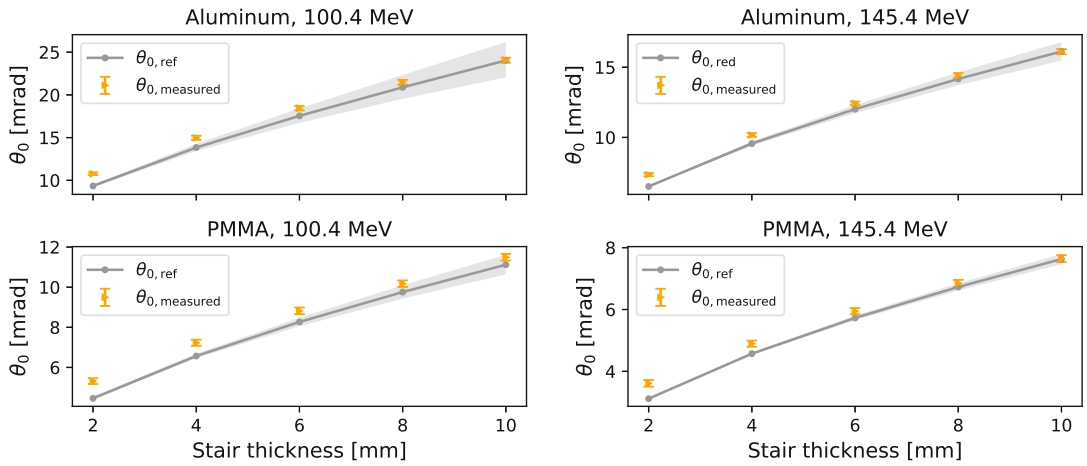


Figure 4.3.5: Analyses of the scattering radiographs at 90 deg (aluminium and PMMA phantom, beam energies of 100.4 MeV and 145.4 MeV). Measured values $\theta_{0,\text{measured}}$ are compared to reference values $\theta_{0,\text{ref}}$. The error bars indicate one standard deviation of the measurement value. Figure from Kaser et al. [83] (adapted).

As shown in section 2.1.2, the expected scattering distribution (described by $\theta_0$) of an initially parallel, mono-energetic proton beam after passing a thin absorber can be calculated using the Highland formula, see equation (2.1.8). Besides the particle energy and the absorber thickness, the formula requires the knowledge of the radiation length $X_0$ of the absorber material, which amounts to 88.97 mm for aluminium (phantom material), 340.7 mm for PMMA (phantom material) and 93.70 mm for silicon (material of the tracking modules) [116]. With these radiation lengths, reference values for $\theta_0$ were calculated for each phantom stair thickness. To do so, the energy loss within the four silicon tracker modules and the phantom itself was estimated via the Bethe equation, see equation (2.1.3). The value of $\theta_0$ resulting from the calculated entry and exit energy are seen as light gray bands in figure 4.3.5, while the solid dark gray line represents the value of $\theta_0$ calculated for the geometric mean of entry and exit energy, further referred to as $\theta_{0,\text{ref}}$.

These reference values can be compared to the actual measurement values for each phantom step, which are displayed in orange in figure 4.3.5. To determine the actual measurement value $\theta_{0,\,\text{measured}}$, a ROI of $3 \times 22$ pixels within each stair was evaluated ($\theta_{0,\,\text{measured, init}}$) and the background value $\theta_{0,\,\text{background}}$ (measured outside the phantom area) was subtracted

$$\theta_{0,\,\text{measured}} = \sqrt{\theta^2_{0,\,\text{measured, init}} - \theta^2_{0,\,\text{background}}}. \tag{4.3.3}$$

The relative error $\epsilon_{\theta_0}$, defined as

$$\epsilon_{\theta_0}(\%) = 100 \cdot \frac{\theta_{0,\,\text{measured}} - \theta_{0,\,\text{ref}}}{\theta_{0,\,\text{ref}}} \tag{4.3.4}$$

was determined to be between 12.9 % and 19.2 % for the thinnest phantom stairs (2 mm). For the thickest stairs (10 mm), $\epsilon_\theta$ was evaluated to be between 0.1 % and 3.4 %, depending on the beam energy and phantom material.

### 4.3.3 Attenuation radiography

The main results reported in this section were published and discussed in Kaser et al. [85], while one attenuation pRad was already shown in Kaser et al. [83]. Equivalent to scattering imaging, attenuation imaging is based on a tracker measurement only. Thus, the calorimeter can be excluded from the iCT measurement setup. In contrast to the imaging techniques described in the last sections, the trigger scintillators were placed in front of the upstream trackers. Otherwise, only particles passing the full tracking setup would be recorded. This would rule out attenuation imaging, as this technique is based on the ratio of particles passing the full tracker to those which were absorbed in the phantom (and therefore only passed through the upstream tracker). The imaging method was investigated for three proton beam energies, namely 100.4 MeV, 145.4 MeV and 800.0 MeV using the iCT demonstrator presented in section 4.2 (without calorimeter) and the aluminium stair phantom shown in section 4.2.1.

The basic principle of this imaging technique was already discussed in section 2.6.2. In principle, two scenarios should be of interest for proton beam (or, in more general, ion beam) attenuation imaging. If a proton or ion passes through the phantom and hence creates hits in all four detector planes of the particle tracker, it contributes to the incoming particle fluence $\phi_{\text{in}}$ as well as to the final particle fluence $\phi_{\text{out}}$. However, due to inelastic nuclear scattering, the charged particle could already be absorbed in the phantom and hence only create two upstream hits. In this case, the proton or ion only contributes to $\phi_{\text{in}}$, which is expected to decrease exponentially with the phantom thickness [22].

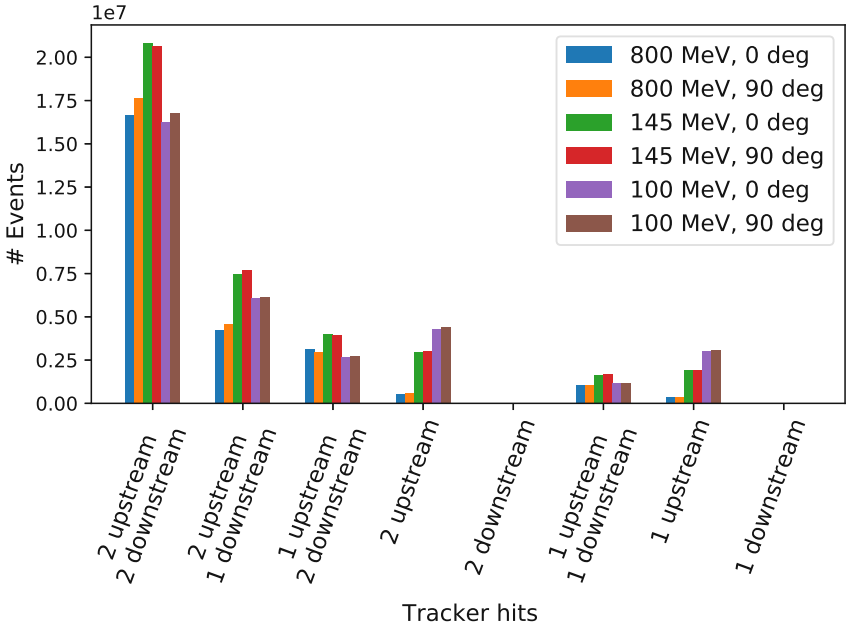


Figure 4.3.6: Number of upstream and downstream tracker hits recorded for attenuation images (100.4 MeV, 145.4 MeV and 800.0 MeV at 0° and 90°). Figure from Kaser et al. [85].

These two scenarios can be recreated in an idealized setup, such as in a Monte Carlo simulation. A detailed study of attenuation imaging with protons with a single particle

tracking setup was done in Quiñones et al. [22] using Geant4 simulated data. However, for the measurements with a real iCT scanner, additional detector hit scenarios compared to the ones previously reported may be recorded. Figure 4.3.6 displays the combinations of upstream and downstream hits that were obtained with the iCT demonstrator for various proton beam energies and phantom rotation angles. Some combinations of upstream and downstream hits can be explained by the physical properties of the tracker itself. As the DSSDs consist of 300 µm silicon each, they can themselves absorb a certain fraction of the incoming proton fluence. If a proton gets absorbed in the tracker, only one upstream or only one downstream hit could be recorded. Furthermore, elastic scattering in the phantom or the tracker modules could lead to a steep angle in the proton path with regard to the original beam direction, which could also cause that the particle does not reach all detector planes. Depending on the detail of the simulation, these effects may also be accounted for in a Monte Carlo setup. Other upstream and downstream hit combinations (such as, for example, only one downstream hit) can also occur when using real measurement data and can be caused by ghost hits, detector noise or errors in the decoding of the raw data. This underlines the importance of verifying Monte Carlo studies of this imaging technique with experimental data [85]. To decide which of the detector hit combinations displayed in figure 4.3.6 should contribute to which fluence ($\phi_{\text{in}}$, $\phi_{\text{out}}$, none or both of them), however, Monte Carlo simulations can be used. In Kaser et al. [85], they were hence exploited to implement two analysis methods. The following description closely follows the wording used in Kaser et al. [85]:

**Analysis for low energies:** This analysis method was applied to experimental data measured at beam energies of 100.4 MeV and 145.4 MeV. All protons, that created two upstream hits but no downstream hits, were assigned to the initial flux $\phi_{\text{in}}$. Protons that created two upstream hits and one or two downstream hits were assigned to $\phi_{\text{out}}$ (and, of course, also contributed to $\phi_{\text{in}}$). By using Monte Carlo simulations, it could be verified that protons that only created one downstream hit are likely to be primary particles that, due to MCS, were scattered in a way that they did not reach the second downstream detector (steep exit angle with regard to the original beam direction).

**Analysis for high energies:** As the effect of MCS decreases with increasing energy, a different analysis was created for the measurement at 800 MeV. Monte Carlo simulations were used to verify that the major fraction of particles, which passed through the phantom, also passed both downstream trackers (99.7 %). Particles that only created one hit in the first downstream tracker plane, were mostly secondaries that resulted from inelastic collisions of the primary protons in the phantom material. Therefore, protons that caused two upstream hits were counted as $\phi_{\text{in}}$, while only protons with two upstream and two downstream hits contributed to $\phi_{\text{in}}$ and $\phi_{\text{out}}$.

In order to create the final attenuation images, the Corryvreckan module *TrackingMultiplet* was adapted for attenuation imaging [83]. The number of hits per tracker plane of each event were extracted from this Corryvreckan analysis, and a subsequent python analysis was performed. The radiographic pixel values ($-\ln(\phi_{\text{out}}/\phi_{\text{in}})$) were obtained by binning the proton hits in the centre of rotation by following the initial direction (obtained from the upstream tracker) and final direction (obtained from the downstream tracker, if the particle created hits there).

For all measured attenuation pRads, the total number of events is reported in table 4.2. As attenuation imaging is prone to noise [22] more than other ion imaging modalities, a high primary fluence was used for each pRad (corresponding the measurement times up to one hour per pRad with the iCT demonstrator system).

For the measurement with the 800 MeV proton beam, enhanced occurrence of noisy strips was observed in the measurement, especially for the second module of the upstream tracker. This had a severe impact on the tracking efficiency: only 25 % to 35 % of the hits registered

| **Energy** [MeV] | **Rotation angle** [°] | **Primary particles** [$10^7$] |
|---|---|---|
| 100.4 | 0 | 2.73 |
| 100.4 | 90 | 2.66 |
| 145.4 | 0 | 3.13 |
| 145.4 | 90 | 3.13 |
| 800.0 | 0 | 1.72 |
| 800.0 | 90 | 1.82 |

Table 4.2: Total number of events that was recorded for each attenuation pRad [85].

at the first upstream tracker module were also recorded at the second module. After masking the noisy strips, this ratio could be increased to a value of approximately 83 %. One example for masking the second detector ($y$ direction) is given in figures 4.3.7 (unmasked) and 4.3.8 (masked). For the unmasked case, one apparent noisy strip at approximately −6 mm is visible. By masking this strip, the peak disappears and the number of valid hits at the other strips increases. However, the noisy strips and subsequent masking still decreased the overall number of valid hits, leading to lower statistics as compared to the attenuation pRads measured at other beam energies (see table 4.2) [85].

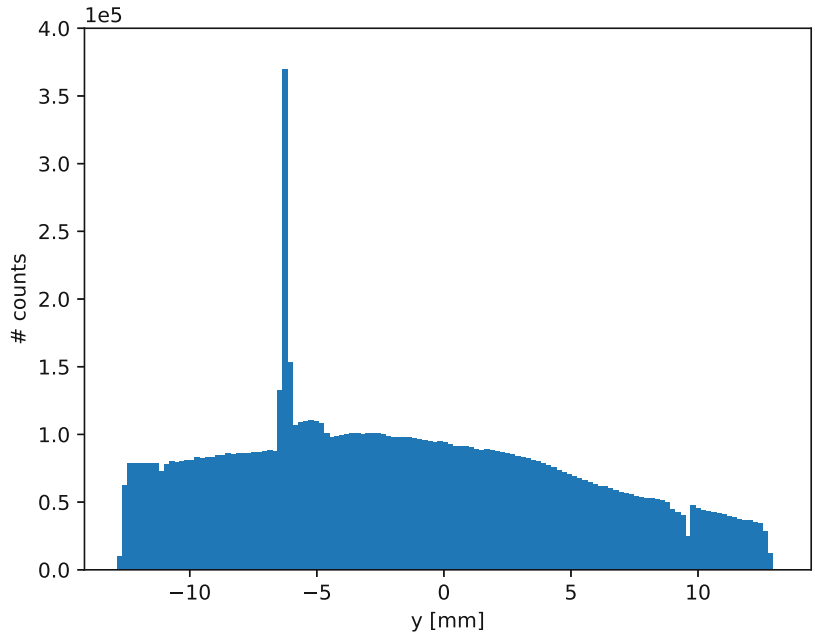


Figure 4.3.7: Example detector hits at 800 MeV (y-direction of the second upstream tracker module) without masking.

Figure 4.3.9 shows the resulting attenuation pRads measured at initial proton beam energies of 100.4 MeV, 145.4 MeV and 800.0 MeV. As discussed in section 2.6.2, the projection value is given as the logarithmic fraction between final and initial beam fluence ($\phi_{\text{out}}$ and $\phi_{\text{in}}$, respectively). In the top row, the side profile of the aluminium stair profile is seen (constant thickness of 10 mm, corresponding to a rotation angle of 0°). The bottom row displays the images measured at a rotation angle of 90°, where the five different stair thicknesses (ranging from 2 mm to 10 mm) can be observed in their frontal view. The field of view was cut to the phantom region (although the DSSDs have a larger area), to remove effects of decreasing beam intensity (resulting in high noise) at the edges of the image.

In the background of the images, some streak artefacts are visible. They arise from noisy and subsequently masked strips. At lower energies, they become less apparent due to MCS,

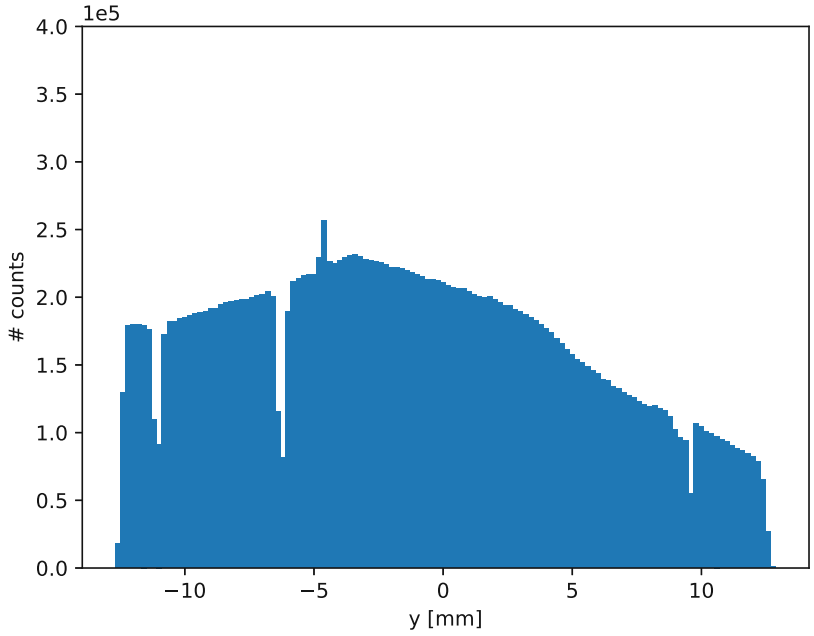


Figure 4.3.8: Example detector hits at 800 MeV (y-direction of the second upstream tracker module) after masking noisy strips.

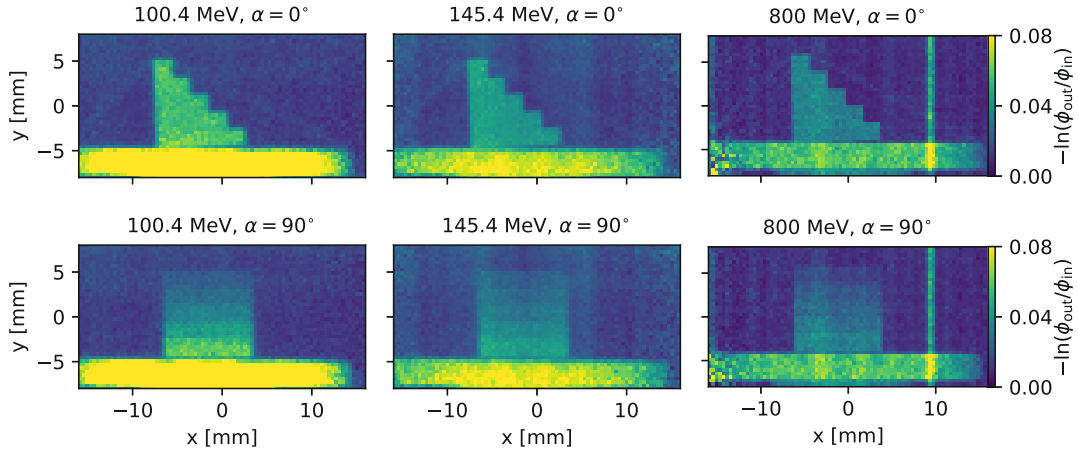


Figure 4.3.9: Beam attenuation radiographs for 100.4 MeV, 145.4 MeV and 800 MeV proton beams. Figure from Kaser et al. [85].

which blurs the artefacts. One obvious streak artefact due to multiple noisy strips in a row is visible in the right area of the image.

In order to remove such artefacts, an additional attenuation pRad can be used, where the phantom is removed from the beam (referred to as *empty* pRad). If the attenuation pRad *including* the phantom is normalized to the *empty* image, the streak artefacts are suppressed if the same strips were noisy in both images. However, some issues arise when using this method. On the one hand, the measurement time doubles as two images have to be recorded. Furthermore, more or other strips could become noisy during both measurements, which would then again cause additional artefacts. One example for the removal of the background artefacts is given in figure 4.3.10 (measurement at 145.4 MeV and using $2.09 \times 10^7$ protons for the *empty* image.).

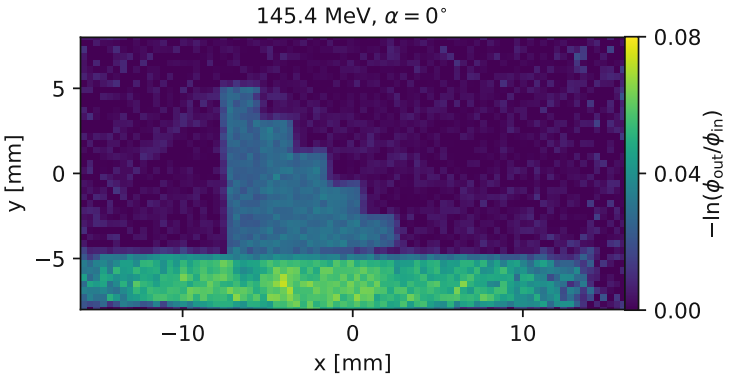


Figure 4.3.10: Beam attenuation pRad at 145.4 MeV. To subtract the background values, an "empty" pRad (no phantom in the beam) was used as a reference. Figure from Kaser et al. [85].

The measurements at a rotation angle of 90° were analysed in more detail, as they allow comparing the obtained pixel values for several stair thicknesses to a theoretical calculation and to a Monte Carlo simulation. For the simulation, the setup (trackers, trigger scintillators and phantom) was recreated in the Geant4 application for tomographic emission (GATE) [89]. For the calculation of expected values, the attenuation can be solved by using equation (2.6.4) (presented in section 2.6.2), which is now given in a simplified form

$$\phi_{\text{out}} \approx \phi_{\text{in}} \exp(-\kappa \Delta z), \tag{4.3.5}$$

where $\kappa$ corresponds to the linear inelastic nuclear cross-section and the path through the medium can be approximated with the stair thickness $\Delta z$ in beam direction. However, to insert the correct value of $\kappa$ to obtain reference values, the energy loss in the imaging system and the phantom have to be considered [85], as $\kappa$ is not an exactly constant function with the energy (especially at low beam energies). Therefore, the Bethe [6] equation (see section 2.1.1) was used to calculate the energy arriving at the phantom after passing through the trigger scintillators ($E_{\text{entry}}$) and the energies after 2 mm to 10 mm of aluminium ($E_{\text{exit}}$). The geometric mean of these energies ($E_{\text{mean}}$) was used as the expected average energy in a phantom stair and was used to extract the respective value of the inelastic nuclear cross-section $\sigma$ from Geant4[1]. To obtain the linear inelastic cross-section $\kappa$ from these values (given in barn), $\sigma$ was multiplied with the particle density of aluminium (density of 2.699 g/cm$^3$ and 26.982 g/mol as extracted from Geant4). For the 10 mm stair, the resulting values of $E_{\text{entry}}$, $E_{\text{exit}}$ and $E_{\text{mean}}$ are stated in table 4.3. As expected, the energy loss within the imaging system is the highest for the lowest beam energy (as the stopping power (SP) increases with decreasing ion energy).

In each phantom step, the average pixel value was determined from an $2 \times 15$ ROI and the background value was subtracted (obtained from a ROI outside the phantom area). In figure 4.3.11, these values are compared to data from a respective Monte Carlo simulation and calculated reference values. For 145.4 MeV and 800.0 MeV, good agreement of all three data sets (measurement, Monte Carlo simulation and calculated values) was observed. However, for the measurement at a beam energy of 100.4 MeV, a discrepancy between the three data sets can be observed: measured values and Monte Carlo data lie clearly above the calculated values. However, since measurement and Monte Carlo data follow a similar trend and correspond well to one another, a systematic reason, which will be discussed later in this section,

[1] obtained from the Geant4 example `https://github.com/Geant4/geant4/tree/master/examples/extended/hadronic/Hadr00` (accessed: 09/2022)

| $E_{\text{init}}$ [MeV] | $E_{\text{entry}}$ [MeV] | $E_{\text{mean}}$ [MeV] | $E_{\text{exit}}$ [MeV] |
|---|---|---|---|
| 100.4 | 73.8 | 61.9 | 52.0 |
| 145.4 | 126.2 | 119.3 | 112.7 |
| 800.0 | 792.3 | 789.8 | 787.3 |

Table 4.3: Primary beam energies used to measure the attenuation pRads ($E_{\text{init}}$). Furthermore, the energy arriving at the phantom after passing the trigger scintillators and the upstream tracker $E_{\text{entry}}$ and the energy after passing 10 mm of aluminium ($E_{\text{exit}}$) as well as their geometric mean ($E_{\text{mean}}$) are given. $E_{\text{entry}}$ and $E_{\text{exit}}$ were calculated with the Bethe-Bloch formula (also for the other stair thicknesses). The table values were published in Kaser et al. [85].

was identified to be the most probable reason for the mismatch with regard to the calculated values [85].

The approximation introduced in equation (4.3.5) can be used to approximate the value of the linear inelastic nuclear cross-section $\kappa$. Starting from this equation, the projection value $p_i = -\ln(\phi_{\text{out}}/\phi_{\text{in}})$ is equal to the product of the product of $\kappa$ and the stair thickness $\Delta z$ [85]

$$p_i \approx \kappa \cdot \Delta z. \tag{4.3.6}$$

Therefore, $\kappa$ can be simply approximated by dividing the projection value by the stair thickness

$$\kappa \approx p_i/\Delta z. \tag{4.3.7}$$

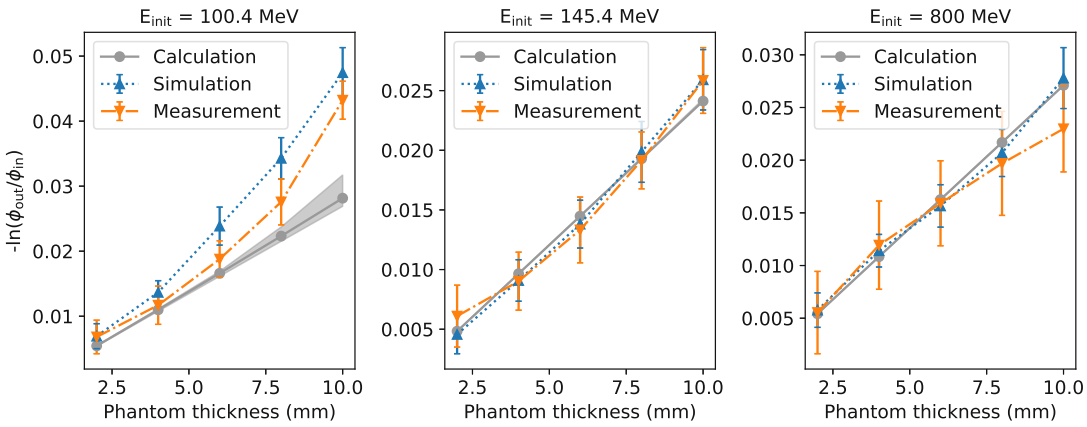


Figure 4.3.11: Comparison of measured (orange), simulated (blue) and calculated (gray) fluence loss for initial beam energies of 100.4 MeV, 145.4 MeV and 800 MeV. Figure from Kaser et al. [85] (adapted).

Equation (4.3.7) was evaluated for the attenuation pRads measured at a rotation angle of 0° (side view of the phantom). This allowed for a quadratic ROI (5 × 5 pixels) in the phantom centre (edge effects and influence of the rotary table are less probable). The background value (obtained from a ROI outside the phantom area) was subtracted from the average projection value in the phantom. The resulting values for $\kappa$ were again compared to the cross-sections extracted from Geant4, as seen in figure 4.3.12.

A similar result as for the single-stair analysis was observed. For the measurements at 145.4 MeV and 800.0 MeV, good accordance with literature values was found. Especially the value of $\kappa$ obtained at 800.0 MeV ($2.79 \times 10^{-3}\,\text{mm}^{-1}$), matched very well with an existing measurement at 792.9 MeV [117], where the inelastic nuclear cross-section $\sigma$ was deter-

mined to be 466 mb (corrsponding to $\kappa = 2.81 \times 10^{-3}\,\mathrm{mm}^{-1}$). At a primary beam energy of 145.4 MeV (correspnding to a mean energy of 119.3 MeV in the phantom), $\kappa$ was expected to be $2.41 \times 10^{-3}\,\mathrm{mm}^{-1}$. A value of $2.60 \times 10^{-3}\,\mathrm{mm}^{-1}$ was actually obtained from the measurement [85].

For the measurement at 100.4 MeV (corresponding to a expected mean energy of 61.9 MeV inside the phantom), an apparent offset to the reference value was observed. The measured value of $\kappa$ ($4.01 \times 10^{-3}\,\mathrm{mm}^{-1}$) was clearly higher than the expected value of $2.82 \times 10^{-3}\,\mathrm{mm}^{-1}$. The reason for this offset was identified using Monte Carlo simulation data. The imaging setup was modelled in GATE using the materials and distances described in section 4.2. From this simulation, $\kappa$ was determined to be $4.9 \times 10^{-3}\,\mathrm{mm}^{-1}$. As the actual measurement value, this lies clearly above the reference value. In a second simulation, the four tracker planes were moved closer to the phantom (to a distance of 1 cm and 2 cm upstream and downstream from the outer phantom edge). Before that, a distance of 5 cm and 10 cm to the phantom edge was used [85]. In this simulation, $\kappa$ was determined to be $2.89 \times 10^{-3}\,\mathrm{mm}^{-1}$, which corresponds well with the reference value. Apparently, the tracker elements need to be closer to the phantom for measurements at this energy, as MCS otherwise removes an essential part of the beam, which is then mistakenly interpreted as fluence loss due to inelastic nuclear scattering [85].

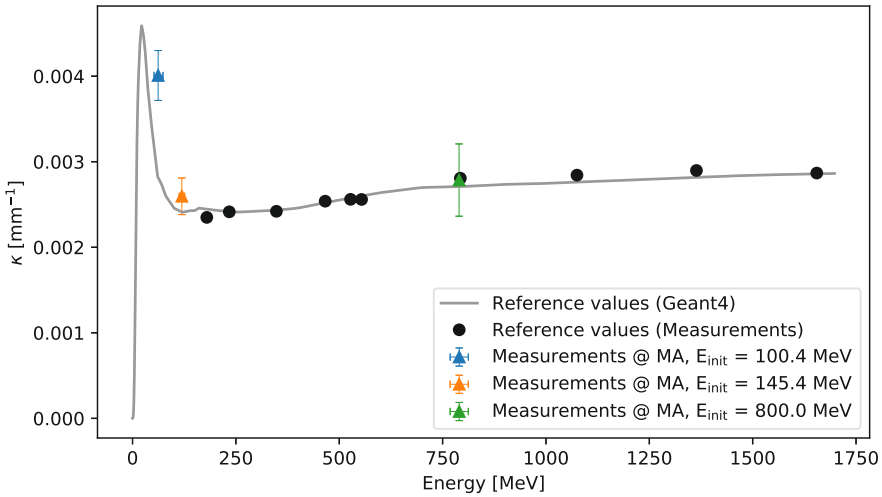


Figure 4.3.12: Estimated linear nuclear cross-sections from attenuation imaging at 100.4 MeV, 145.4 MeV and 800 MeV. The black dots correspond to measurement data extracted from the EXFOR data base [118] that were converted from nuclear cross-sections to linear nuclear cross-sections by multiplying them with particle density of aluminium [85]. The gray line corresponds to the data extracted from Geant4. Figure from Kaser et al. [85] (adapted).

This finding reveals one main drawback of attenuation imaging. If the trackers are not positioned close enough to the respective phantom, an image of high contrast but increased pixel values may be obtained. However, not every geometry may allow such a positioning, due to additional equipment (e.g., the rotary table in case of the iCT demonstrator) or phantoms, which are not rotationally symmetric (such as a head model, which will result in various distances from the actual object to the tracker) [85].

## 4.4 Discussion

In this chapter, the iCT demonstrator that was installed and operated at MedAustron, was introduced. Due to its size (DSSD tracker planes have an active area of 51.2 mm × 25.6 mm),

it is limited to the imaging of small phantoms only. However, the system allows investigating ion imaging in a real scenario and to identify challenges and requirements for a future system to be designed with appropriate size, speed (DAQ) and accuracy.

Three different imaging modalities were investigated with the demonstrator and discussed in this chapter. Ion imaging based on energy loss is a modality with a promising future application in the clinic, as it would allow receiving patient WETs and RSPs without further conversion from other images. While in section 4.3.1, only radiographic images were shown, this imaging modality will be discussed in full detail (including the reconstruction procedure) in section 5.

Other imaging modalities may find application as a complementary measurement in the clinic in the future, or as a stand-alone technique in material science. Using only the tracker of the iCT system allows measuring images based on MCS and beam attenuation. Regarding the first imaging modality, pRads at two energies (100.4 MeV and 145.4 MeV), at two rotation angles (0° and 90°) were measured of two phantoms (stair profiles made of PMMA and aluminium). Images with a high degree of detail were obtained and presented in section 4.3.2. In the side view, even the Kapton tape, that attached the phantom to the rotary table, was visible (see figures 4.3.3 and 4.3.4). Measured values for the scattering distribution showed good accordance with theoretically calculated values. As a future improvement, however, a full reconstruction should include a sophisticated ion path estimate such as presented in Krah et al. [84].

For attenuation imaging with a single particle tracking setup, a comprehensive Monte Carlo study was already presented in Quiñones et al. [22]. However, the results in section 4.3.3 showed the importance of a verification with a real demonstrator system. While Monte Carlo simulations are a solid method to generate reference data, to investigate the general feasibility of an imaging technique or to identify some systematic sources of error, a certain level of idealization will always remain in contrast to a real setup. For attenuation imaging, the radiographic pixel values do not correspond to an average quantity obtained from all ions assigned to a certain pixel, but the actual ion count per pixel. Therefore, an idealized setup as used in simulations can have a strong impact on the imaging result. In this chapter, however, it could be shown, that imaging with a real single particle tracking setup allows obtaining images based on beam attenuation. While a measurement at 800.0 MeV showed good agreement with literature values, measurements at lower energies showed an offset to the expected reference, which was found to be caused by the distance between the tracker planes and the phantom. Due to increased amount of noise in attenuation imaging, the imaging method requires higher statistics than other imaging modalities. This could likely prevent the implementation of this technique as a stand-alone tool in a clinical setting. However, attenuation imaging may still be used as complementary imaging modality alongside with other ion imaging modalities in the future.

# CHAPTER 5

## Development of an ion CT reconstruction workflow

In this chapter, an overview on the development of an ion computed tomography (iCT) reconstruction workflow for the demonstrator system described in chapter 4 will be given. Before applying the workflow to the data measured with the demonstrator (see section 5.3), it was applied to preparatory Monte Carlo simulations (see section 5.2), modelling the test setup with ideal and realistic assumptions. Furthermore, the workflow was tested for phantoms of clinically relevant size, see section 5.4. To benchmark the reconstruction results in terms of relative stopping power (RSP) accuracy, reference values are crucial. Therefore, R80 measurements, as described in section 5.1 were performed in a Monte Carlo simulation.

### 5.1 R80 measurement

An R80 measurement, as, for example, described in Michalak et al. [119], can be used to define a reference value for the RSP of the materials under investigation in an iCT scan. The measurement, which is schematically displayed in figure 5.1.1, consists of two parts: At first, an ion beam with energy $E_{\text{in}}$ is directed through air directly into a water absorber. The residual energy $E_{\text{out}}$, which approximately corresponds to the initial energy $E_{\text{in}}$, is fully deposited in the absorber. The resulting Bragg peak can be used to determine the residual beam range ($R_0$). Within this thesis, the R80 was used, which corresponds to the depth in the absorber, where the Bragg peak has decreased to 80 % of its maximum. Other typically used values are the R90 or R20. Furthermore, the maximum value of the Bragg peak could be used to determine the beam range.

Afterwards, the measurement is repeated with a homogenous absorber block of thickness $t_m$, made of the material under investigation, which is placed in front of the water absorber. Again, the residual range of the beam ($R_1$) is recorded in the water absorber using the same range definition as in the primary measurement. The difference between both ranges

$$\text{WET} = R_0 - R_1, \tag{5.1.1}$$

allows determining the water-equivalent thickness (WET) of the material absorber block (see also section 2.2.3). From the WET, the RSP of the material ($\text{RSP}_\text{m}$) can be approximately distinguished using

$$\text{RSP}_\text{m} \approx \frac{\text{WET}}{t_\text{m}}. \tag{5.1.2}$$

In an iCT scan, the RSPs in the obtained image can be compared to the reference values from the R80 measurement. Of course, this reference measurement can only be used if

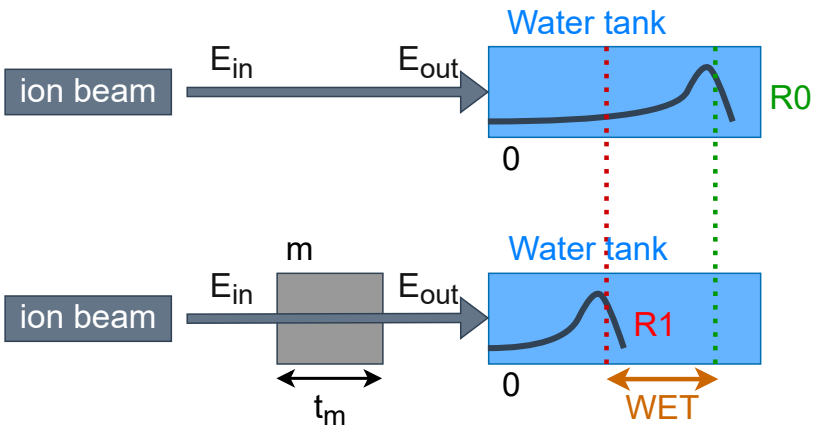


Figure 5.1.1: Schematic representation of an R80 measurement.

the materials under investigation are known in the beginning and available as homogenous material blocks.

## 5.2 Preparatory reconstructions

In order to develop a reconstruction workflow that can be used for the data measured with the iCT demonstrator presented in section 4.2, a preliminary reconstruction workflow was applied to data from Monte Carlo simulations. The workflow was originally presented in Kaser [120] and used in Ulrich-Pur et al. [82]. The Geant4 (see section 3.2.1) simulations that were used to generate imaging data are briefly described in the following.

### 5.2.1 Simulation setup

Two Monte Carlo simulation models based on Geant4 (version `10.05.p01` with the physics list *QGSP_BIC*) were used to investigate image reconstructions with the iCT demonstrator system under ideal and realistic conditions before applying the reconstruction workflow to real measurement data. In both simulations, the aluminium phantom (described in section 4.2.1) was used as object-to-be-imaged. The whole iCT setup was placed in an air volume. A pixel size of 0.5 mm × 0.5 mm was selected for the radiographs taken at each measurement angle, resulting in a size of 100 × 50 pixels. The beam energy was set to 100.4 MeV, which represents the actual beam energy at which preliminary measurements with the given setup were already performed at MedAustron [82, 112]. In both simulations, $10^6$ protons were used per measurement angle, which corresponds to a fluence of 800 protons per mm$^2$ (parallel beam). 180 projections were generated by scanning the phantom in equidistant steps of 2° over a range of 360°.

**Ideal conditions** Six detector planes (300 µm thickness and an active area of 25 mm × 50 mm) were modelled in the simulation (corresponding to the 'old' configuration described in section 4.2). The range telescope was replaced by assuming an ideal energy measurement (infinite energy resolution) at the sixth detector. Ideal (infinite) spatial resolution of the detectors was assumed as well.

**Realistic conditions** In a second simulation (see figure 5.2.1), an existing Geant4 model of the whole test beam setup [82] was used in order to capture the impact of additional material in the beam as well as the impact of realistic spatial resolution and energy resolution on the reconstruction result. The range telescope was modelled with 48 scintillator slices with an active area of 300 mm × 300 mm and a thickness of 3 mm per slice. The energy resolution for each slice was set to 8 % in accordance to Bucciantonio et

al. [121]. The phantom was placed on a rotary table that was included via a CAD model in this simulation. The two trigger scintillators were also included in the simulation model. Since the strip width of the double-sided silicon strip detectors (DSSDs) in $x$-direction is 50 µm and 100 µm in $y$-direction (directions orthogonal to the beam direction $z$), the spatial resolution for the silicon strip detectors was set to 14.43 µm and 28.86 µm in the simulation, corresponding to $\frac{\text{pitch}}{\sqrt{12}}$.

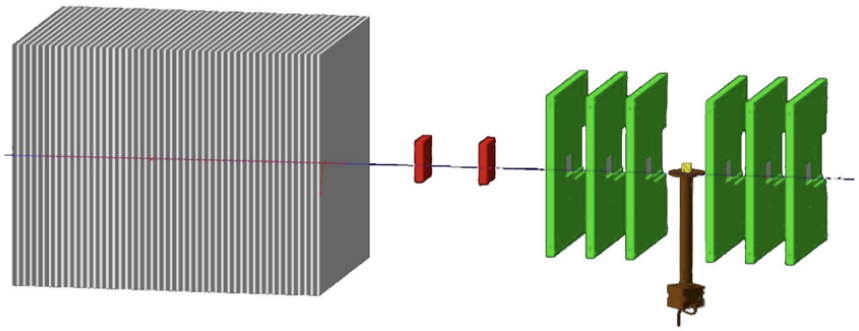

Figure 5.2.1: Simulation of a realistic test beam setup consisting of 6 DSSDs (embedded in the centre of the green printed circuit boards (PCBs)), two trigger units (red) and a range telescope (gray). The phantom (yellow) was placed on a rotary table (brown) in this setup.

### 5.2.2 Projection value definition

As stated in section 2.1.4, the stopping power (SP) of ions in matter can be approximated as [26]

$$S = \frac{dE}{dz} = \frac{E^{1-p}}{p \cdot \alpha}. \tag{5.2.1}$$

While $\alpha$ strongly depends on the material, $p$ only shows a minor material dependence in the energy range for ion imaging. In Zhang et al. [27], ion beams in the energy range from 10 MeV to 250 MeV (protons) and 25 MeV to 1000 MeV (helium ions) were investigated. Values of $p$ between 1.735 and 1.677 were found for proton beams in materials with densities ranging from 0.3 g/cm$^{-3}$ (lung substitute) to 19.311 g/cm$^{-3}$ (gold). Similar values were determined for helium ions. For a preliminary reconstruction workflow, the value of $p$ was therefore regarded to be constant, with a value of 1.7. This is only a valid approximation for protons and helium ions, and would have to be adapted for other ion species. $p$ was inserted into the Bragg-Kleeman rule, resulting in [82]

$$\frac{dE}{dz} = \frac{E^{-0.7}}{1.7 \cdot \alpha}. \tag{5.2.2}$$

As shown in Ulrich-Pur et al. [82], the approximation can be sorted into two parts by moving energy-dependent and spatial functions on one side of the equation each. This sorting is followed by an integration along the ion energy and path, respectively

$$1.7 \cdot \int_{E_{\text{in}}}^{E_{\text{out}}} E^{0.7} dE = \int_{x_{\text{in}}}^{x_{\text{out}}} \frac{1}{\alpha(x,y,z)} dz. \tag{5.2.3}$$

Reconstruction frameworks like the tomographic iterative GPU-based reconstruction (TIGRE) toolbox only work with positive inputs. Negative values are seen as violation of physics (in case of iCT this would correspond to an energy gain of the ions in the object). Therefore, the integration limits for the energy-dependent term were interchanged and the absolute value

of the term depending on the ion path is taken. Furthermore, the integration is approximated with a numerical addition over several small steps $\Delta z$ in the beam direction [82]

$$E_{\text{in}}^{1.7} - E_{\text{out}}^{1.7} \approx \left|\sum \frac{1}{\alpha(x,y,z)} \Delta z\right|. \tag{5.2.4}$$

This equation already has the form of a tomographic equation as presented in section 2.5.1, with an unknown function $\alpha$ to be determined in the reconstruction process from the projections

$$p(\theta, x, y) = \int |\alpha(x,y,z)| ds \approx \sum |\alpha(x,y,z)| \Delta z. \tag{5.2.5}$$

The SP can be obtained by inserting the reconstructed $\alpha$ in equation (5.2.1). To further obtain the RSP, the reconstructed SP has to be further divided by the SP in water at the same ion beam energy. Therefore, the parameters given in Zhang et al. [27] ($\alpha$ =2.633 × $10^{-3}$, $p$ =1.735 for protons) were again inserted in equation (5.2.1).

### 5.2.3 Binning and position cuts

Due to promising results of the TIGRE toolbox (see section 3.4) with noisy and limited projection data [68] and due to its layered structure which allows for a user-friendly application, the framework was chosen as reconstruction tool. However, as it was developed for x-ray computed tomography (CT), the toolbox only allows for reconstructions along straight lines. In order to improve the reconstruction result, a similar approach as presented by Cirrone et al. [122] was chosen (see Kaser [120] and Kaser et al. [123]). For each particle, the hit positions on the two innermost detectors are compared: they are further referred to as $\text{D}_{\text{init}}$ and $\text{D}_{\text{exit}}$ and correspond to the third and fourth tracker plane in case of six DSSDs, respectively. In both directions orthogonal to the beam direction $z$, the absolute difference between the hit positions is calculated using

$$d_x = |\, x(\text{D}_{\text{init}}) - x(\text{D}_{\text{exit}}) \,|, \tag{5.2.6}$$

$$d_y = |\, y(\text{D}_{\text{init}}) - y(\text{D}_{\text{exit}}) \,|. \tag{5.2.7}$$

These differences are compared to a threshold $t_{x,y}$. Only if both values $d_x$ and $d_y$ are smaller than the given threshold (further referred to as *position cut*),

$$d_x < t_{x,y}, \tag{5.2.8}$$

$$d_y < t_{x,y}, \tag{5.2.9}$$

the ion is used in the projection (corresponding to a proton radiography (pRad)), otherwise it is removed from the data set.

If an ion fulfils equations (5.2.8) and (5.2.9), its projection value (see section 5.2.2) is binned in the centre of rotation using the average of the hit positions at $\text{D}_{\text{init}}$ and $\text{D}_{\text{exit}}$. The choice of the position cut $t_{x,y}$ has an essential impact on the resulting reconstruction, as it affects the size and characteristics of the input data set. In table 5.1, the increasing rejection rate with decreasing $t_{x,y}$ is demonstrated: the average of protons contributing to one 0.5 mm × 0.5 mm pixel is decreased to approximately 10 % of its original value for the strictest position cut ($t_{x,y}$ = 0.5 mm) for the setups described in section 5.2.1. To obtain these values, a projection at 0°, where the protons have to pass through 10 mm of aluminium (side view with constant thickness), was used.

As the 1 mm position cut still allowed using approximately one third of the full data set, this cut option was chosen and compared to reconstructions using no position cut. The reconstruction results are discussed in the following section.

Table 5.1: Different cuts and the resulting particles per pixel (0.5 mm × 0.5 mm) in the phantom area (average measured at centre of phantom in projection at 0°).

| | **Idealized setup** | **Realistic setup** |
|---|---|---|
| $t_{x,y}$ | p/pixel | p/pixel |
| 0.5 mm | 18 | 17 |
| 1.0 mm | 60 | 54 |
| 1.5 mm | 103 | 94 |
| 2.0 mm | 136 | 128 |
| no cut ($t_{x,y} = \infty$) | 177 | 173 |

### 5.2.4 Results

For each experimental setup modelled in Geant4 (ideal and realistic conditions, see section 5.2.1), four reconstructions were analysed. At first, two reconstructions without position cut using 180 and 90 projections/pRads were generated. For comparison, two reconstructions with a 1 mm position cut (again using 180 and 90 pRads as input) were generated. For the reconstruction, the ordered subsets SART (OS-SART) algorithm (see section 2.5.3) as implemented in the TIGRE toolbox was used with 10 iterations and a blocksize of 10.

#### 5.2.4.1 Ideal setup

Figure 5.2.2 displays the reconstructions (central slices) obtained when using 180 pRads as input. On the left, the result without position cut is seen, while the right image shows the reconstruction result with a 1 mm position cut. In the ideal setup, no rotary table was included in the simulation. Therefore, the field-of-view was reduced to the phantom area (although the tracker modules are actually larger, as described in section 5.2.1).

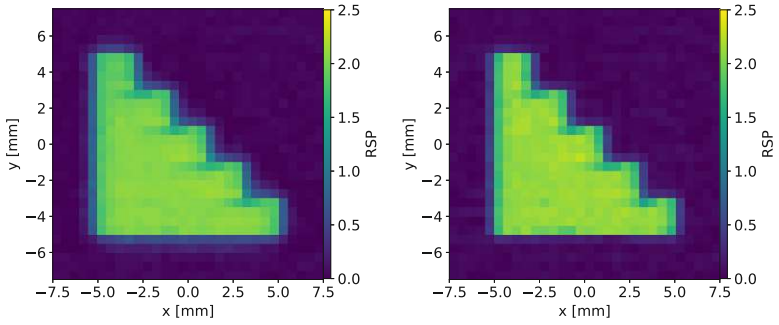


Figure 5.2.2: Reconstructions of the ideal data set (180 projections). Left: no position cut used. Right: 1 mm position cut used.

In both reconstructions, the stair profile is clearly distinguishable from the background. However, some voxels directly surrounding the phantom show a higher RSP than expected for air, resulting in 'smeared' phantom edges. This effect is discussed in more detail in appendix A.3.

Figure 5.2.3 displays the reconstructions with and without 1 mm position cut using 90 pRads as input data. Visually, hardly any difference between the reconstructions using 180 and 90 projections can be determined. For this reason, the RSP was analysed in a region of interest (ROI) in each phantom stair (excluding edge voxels). For each reconstruction, the results are displayed in figure 5.2.4 with the reference value (approximately 2.08, as obtained with an R80 measurement) being marked as a dotted gray line. In the top row, the reconstruction results with 180 pRads as input data can be seen. Especially for the thinnest

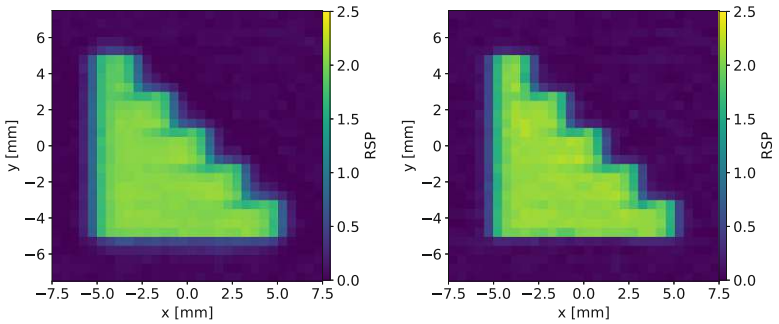


Figure 5.2.3: Reconstructions of the ideal data set (90 projections). Left: no position cut used. Right: 1 mm position cut used.

stair (2 mm thickness), an improvement with the 1 mm position cut can be observed. Without position cut, the average RSP for this stair was determined to be 1.95, while it was found to be 2.08 for the reconstruction using a position cut.

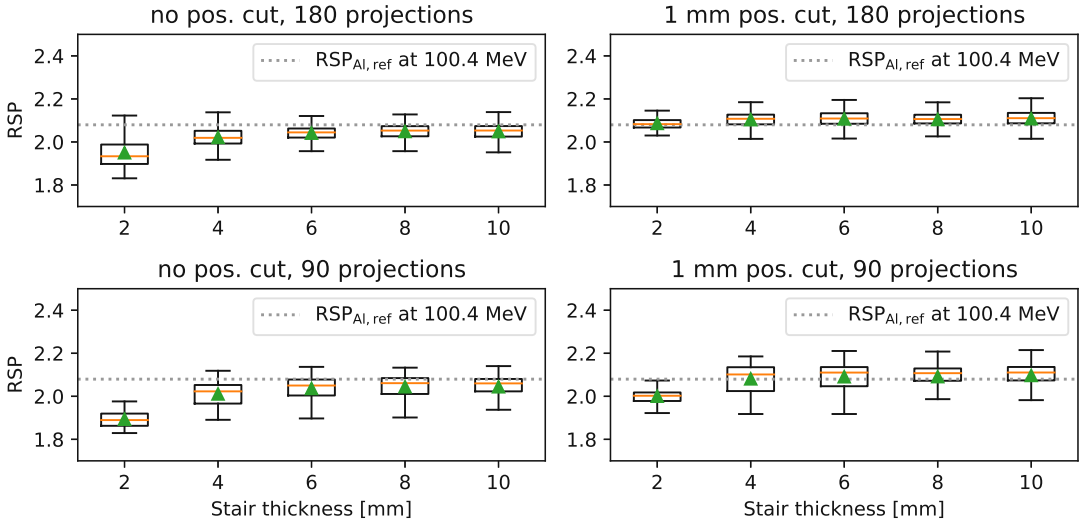


Figure 5.2.4: RSPs in the phantom stairs (ideal data set).

Using only 90 pRads as reconstruction input results in an increased spread of values in a ROI: regarding, for example, the 6 mm step in the reconstruction using a 1 mm position cut, RSPs between 2.08 and 2.13 were found using 180 pRads as input. Using 90 projections resulted in RSPs between 2.05 and 2.14.

### 5.2.4.2 Realistic setup

Figure 5.2.5 displays the central slices of reconstructions using 180 pRads obtained from the 'realistic' Monte Carlo simulation setup (see section 5.2.1) as input data. Figure 5.2.6 shows the reconstruction results using only 90 pRads. In all four resulting images, the phantom stair profile and the rotary table are visible. Again, only minor differences can be visually determined between the images. For further analysis, the edge voxels of the phantom were studied in more detail in appendix A.3.

For a more detailed analysis regarding the RSP accuracy, the values in a ROI in each phantom stair were analysed and are shown in a box plot diagram for each reconstruction (see figure 5.2.7). As expected, the spread of values was found to be generally higher than it was obtained for the reconstruction results using the idealized data set. Furthermore, the reconstructions using a 1 mm position cut showed a higher spread of values in a ROI.

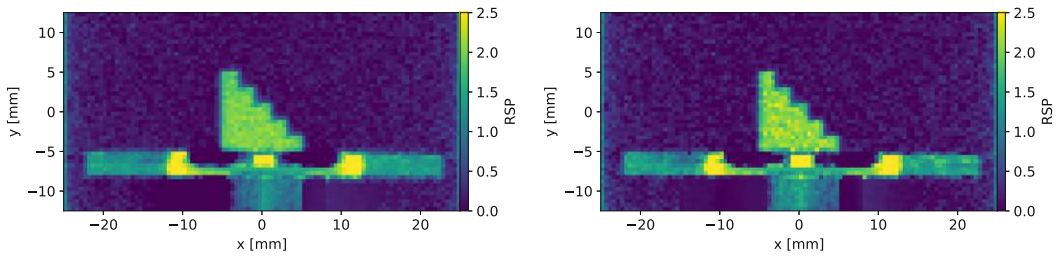


Figure 5.2.5: Reconstructions of the realistic data set (180 projections). Left: no position cut used. Right: 1 mm position cut used.

This effect is due to the particle rejection rate resulting from position cut, which reduces the original data set to approximately one third of its original size (see table 5.1).

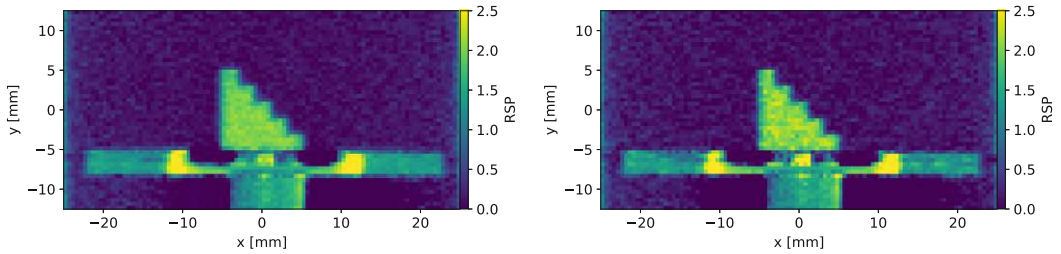


Figure 5.2.6: Reconstructions of the realistic data set (90 projections). Left: no position cut used. Right: 1 mm position cut used.

Again, the 1 mm position cut resulted in an improved RSP accuracy in the thinnest phantom stair. While the average RSP in this stair was determined to be 1.94 without position cut, the value increased to 2.07 with the cut. Using only 90 pRads for the reconstruction impaired the reconstruction result: for the thinnest stair, the average RSP decreased to 1.88 without position cut and 2.00 with 1 mm position cut. However, apart from the ROI in the thinnest phantom stair, cutting the number of pRads used in the reconstruction by half, did not strongly influence the reconstruction result.

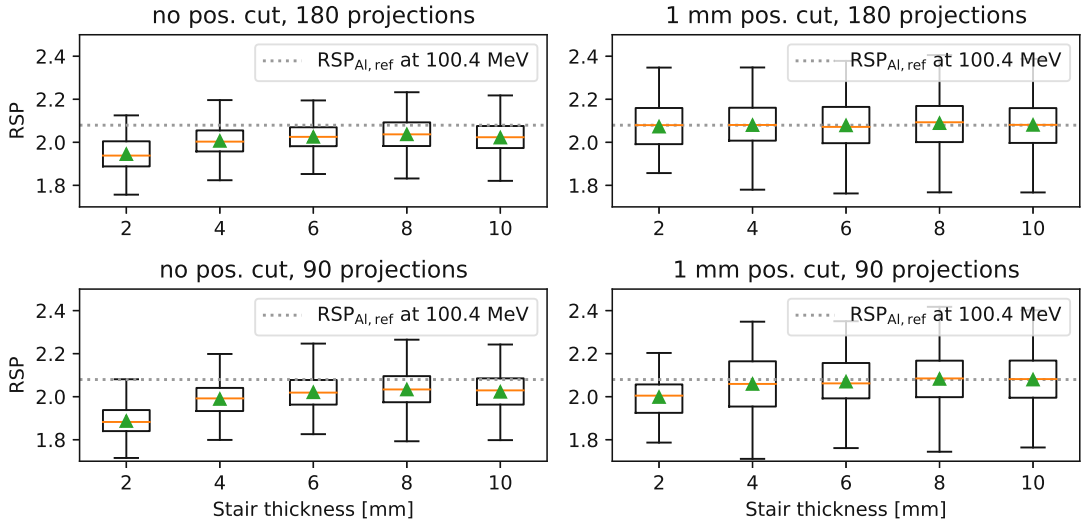


Figure 5.2.7: RSPs in the phantom stairs (realistic data set).

Overall, the presented reconstruction workflow showed promising preliminary results for the investigated phantom. Even in the reconstructions without position cut, the phantom

shape was visible. A position cut was able to improve the result but also caused a data rejection rate of approximately two thirds. For larger phantoms, multiple Coulomb scattering contributes more to the imaging result. Hence the data rejection rate is expected to even increase with a position cut. On the other hand, reconstruction results without any position cut are expected to result in low spatial resolution. These issues are addressed in section 5.4.

## 5.3 Reconstruction results using experimental data

As discussed in section 4.3.1, multiple pRads were measured using the aluminium stair phantom presented in section 4.2.1 as object-to-be-imaged. These pRads were not recorded equidistantly, but with angular steps ranging from 1.8° to 9° covering a full rotation (corresponding to 360°). From these pRads, a 3D RSP map was reconstructed. Reconstruction results using this data set were presented in Ulrich-Pur et al. [113] and the proceedings of the Fully3D conference 2021 [124].

The reconstruction workflow presented in section 5.2 was generally used to create the RSP map from the measured pRads. However, the WET was directly extracted from the range telescope measurement (no conversion from energy to WET was necessary). Two reconstructions of the experimental data set are compared in the following: at first, the pRads were reconstructed using 3 $\sigma$ cuts on the particle energy and scattering angle (further referred to as 3 $\sigma$ reconstruction) but without position cut. Furthermore, a reconstruction using 3 $\sigma$ cuts and, additionally, a 1 mm position cut as described in section 5.2.2 was performed (further referred to as 3 $\sigma$ + 1 mm reconstruction). Using that cut, the number of protons used per projection decreased to approximately $3.6 \times 10^5$ on average. A voxel size of $(0.2 \times 0.2 \times 0.2)\,\mathrm{mm}^3$ was used. For the reconstruction, the OS-SART (see section 2.5.3) was used with 10 iterations and a block size of 10.

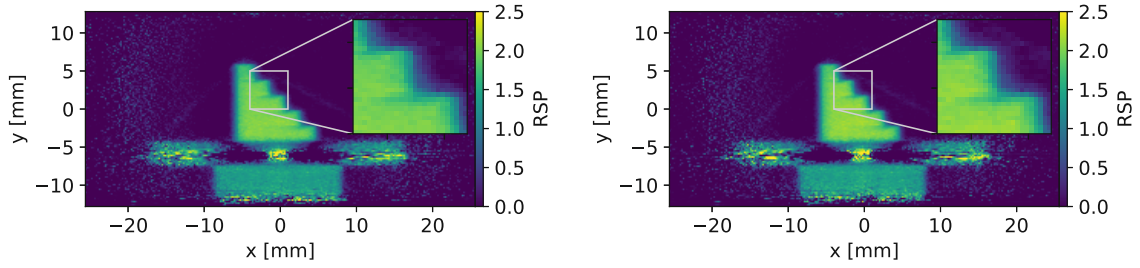


Figure 5.3.1: Reconstruction of a 3D RSP map from multiple pRads. In the image, the central slice of the phantom is displayed and parts of the stair profile are zoomed in for better comparison between the reconstructions. Left: reconstruction using 3 $\sigma$ cuts only. Right: reconstruction using 3 $\sigma$ cuts and a 1 mm position cut.

The central slices ($xy$-plane) of the reconstructions are displayed in figure 5.3.1. Visually, only minor differences between the two reconstructed slices can be observed (as for the simulation results presented in section 5.2.4). In both images, the five phantom stairs are visible. Furthermore, the rotary table is seen in both reconstructions and is actually smaller than the CAD model used in the simulations in section 5.2. Figure 5.3.2 shows a 3D rendering of the reconstructed data.

To compare the reconstructions in more detail, the RSPs in the single phantom voxels were analysed. Therefore, a ROI was defined in the centre of each phantom step (to exclude edge effects, a distance of 0.4 mm to the phantom edge was used for the ROI). The obtained values are visualized in a box plot diagram in figure 5.3.3. For both reconstructions (3 $\sigma$ and 3 $\sigma$ + 1 mm), the median (orange) and average (green) values lie below the expected reference value in all cases. The effect is the strongest for the thinnest (2 mm) stair: for the

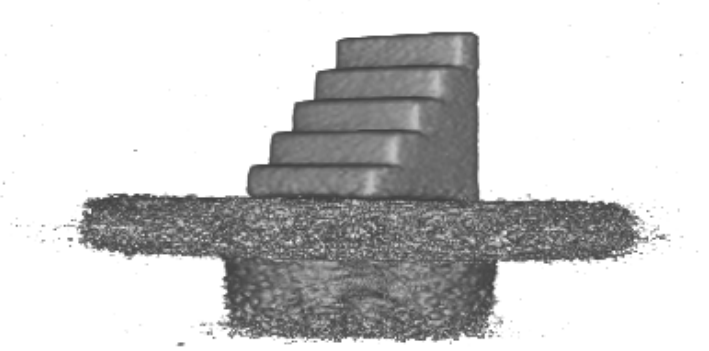

Figure 5.3.2: 3D rendering of the reconstructed RSP map. The figure was taken from Schramm et al. [124].

3 $\sigma$ reconstruction, the average RSP lies 15.2% below the reference. A slight improvement can be seen using the additional 1 mm position cut, where the error of the average value decreases to -12.6% for the thinnest stair. Smaller relative errors on the RSP average were found for the other ROIs: they were ranging between −8.1 % and −5.0 % for the 3 $\sigma$ reconstruction and −6.1 % and −3.2 % for the 3 $\sigma$ + 1 mm reconstruction.

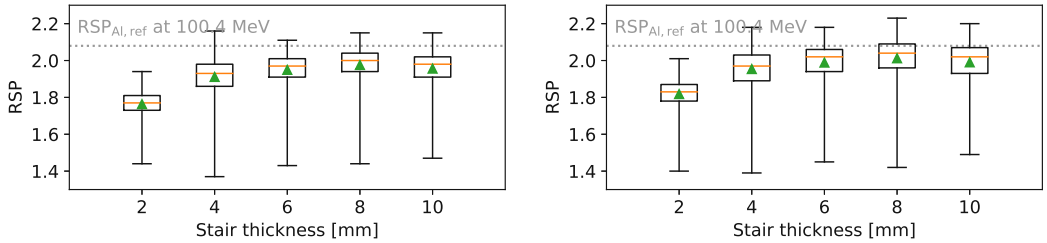


Figure 5.3.3: RSPs in the phantom stairs (central ROI excluding edge effects). The orange line corresponds to the median value, while the green marker shows the average RSP in a ROI. Left: reconstruction using 3 $\sigma$ cuts only. Right: reconstruction using 3 $\sigma$ cuts and a 1 mm position cut. The figure was taken from Schramm et al. [124] (adapted).

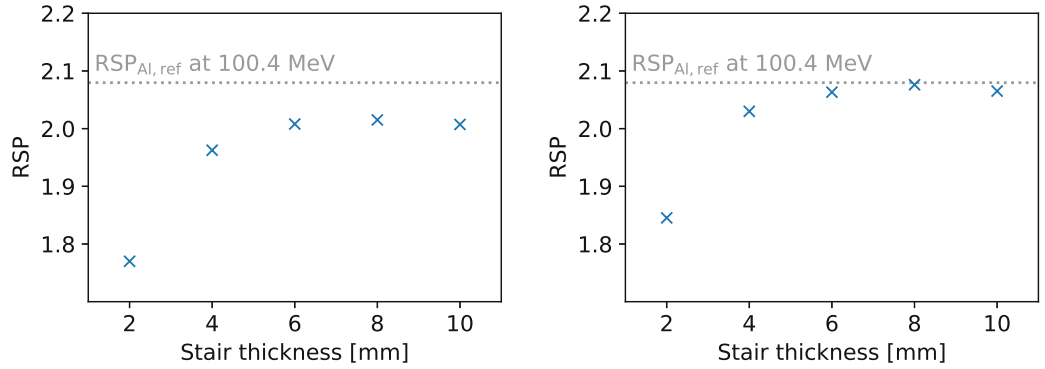


Figure 5.3.4: RSPs in the phantom stairs (most probable values (MPVs)). Left: without position cuts. Right: with 1 mm position cuts.

In figure 5.3.3 it is evident that the RSP average per ROI always lies below the median value, indicating that the distribution of RSPs does not exactly follow a Gaussian shape. In fact, the distributions showed a Gaussian-like shape with a long tail towards low RSPs. Therefore, also the MPVs were analysed for each ROI by extracting the bin with the largest

count in an RSP histogram for each phantom stair. They are displayed in figure 5.3.4. Again, both reconstructions show a similar behaviour: the relative error was the highest for the thinnest step (-14.9% for the 3 $\sigma$ reconstruction and -11.3% for the 3 $\sigma$ + 1 mm reconstruction). For the other stairs, the maximum relative errors were found to be -5.6% (3 $\sigma$ reconstruction) and 2.4% (3 $\sigma$ + 1 mm reconstruction).

The average RSPs, median RSPs and MPVs for all ROI and their relative errors are summarized in table 5.2 (3 $\sigma$ reconstruction) and table 5.3 (3 $\sigma$ + 1 mm reconstruction). It can be concluded that the position cut has a small but measurable impact on the reconstruction of the aluminium phantom. However, due to the limited phantom size, even the reconstruction without additional cut does show the object's details (stairs) and only results in slightly worse RSP accuracy.

Table 5.2: Average RSP, median RSP and MPV for each ROI of the 3 $\sigma$ reconstruction.

| **Stair thickness [mm]** | **Average** | **Rel. error [%]** | **Median** | **Rel. error [%]** | **MPV** | **Rel. error [%]** |
|---|---|---|---|---|---|---|
| 2 | 1.76 | -15.2 | 1.77 | -14.9 | 1.77 | -14.9 |
| 4 | 1.91 | -8.1 | 1.93 | -7.2 | 1.96 | -5.6 |
| 6 | 1.95 | -6.3 | 1.97 | -5.3 | 2.01 | -3.4 |
| 8 | 1.98 | -5.0 | 2.00 | -3.8 | 2.02 | -3.1 |
| 10 | 1.96 | -5.9 | 1.98 | -4.8 | 2.01 | -3.4 |

Table 5.3: Average RSP, median RSP and MPV for each ROI of the 3 $\sigma$ + 1 mm reconstruction.

| **Stair thickness [mm]** | **Average** | **Rel. error [%]** | **Median** | **Rel. error [%]** | **MPV** | **Rel. error [%]** |
|---|---|---|---|---|---|---|
| 2 | 1.82 | -12.6 | 1.83 | -12.0 | 1.85 | -11.3 |
| 4 | 1.95 | -6.1 | 1.97 | -5.3 | 2.03 | -2.4 |
| 6 | 1.99 | -4.4 | 2.02 | -2.7 | 2.06 | -0.8 |
| 8 | 2.01 | -3.2 | 2.04 | -1.9 | 2.08 | -0.2 |
| 10 | 1.99 | -4.3 | 2.02 | -2.9 | 2.07 | -0.7 |

## 5.4 Investigation of larger phantom sizes

Due to the size of the tracker modules of the demonstrator (51.2 mm × 25.6 mm, see section 4.2), the phantom size that can be investigated, is limited. However, in this section, the reconstruction workflow presented in section 5.2 is used to reconstruct 3D RSP maps of larger phantoms using Monte Carlo simulated data. The phantoms that were used for this study are presented in section 5.4.1. The imaging setup implemented in the simulations is discussed in section 5.4.2 and a refined definition of the projection values is discussed in section 5.4.3. The results of this section were presented in Kaser et al. [123] and the proceedings of the Fully3D conference 2021 [124]. The descriptions and interpretations in this section closely follow the structure and content of these two publications.

### 5.4.1 Phantoms

The Catphan® (CTP) modules CTP528 (high resolution) and CTP404 (sensitometry) (The Phantom Laboratory Incorporated, Salem, NY, USA) [125] were replicated as phantoms in a

Geant4 Monte Carlo simulation [123]. They each consist of a cylindrical body with a diameter of 15 cm. In this acrylic body, specific inserts allow determining the spatial resolution and RSP accuracy of a reconstruction. Both modules are displayed in figure 5.4.1.

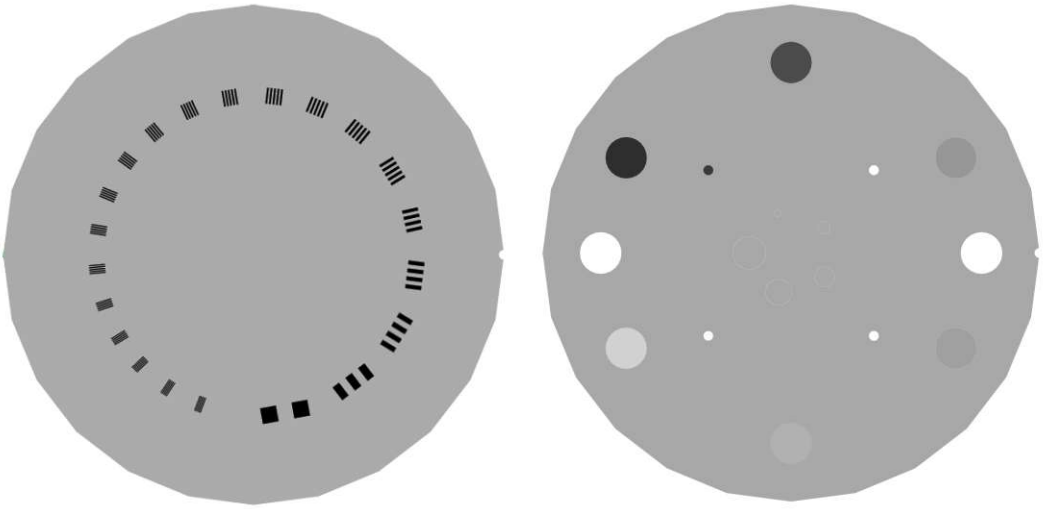

Figure 5.4.1: CTP modules used as phantoms in the Monte Carlo simulations. Left: high resolution module (CTP528). Right: sensitometry module (CTP404). The figure was taken from Kaser et al. [126].

The CTP528 incorporates 21 aluminium inserts with decreasing thickness, ranging from 1 to 21 line pairs (lp) per cm (corresponding to an insert thickness of 0.5 cm to 0.024 cm, respectively). The CTP404 contains multiple cylindrical inserts made of several materials, with RSPs above and below the one of water ($RSP_{water} = 1$). The materials of the outer cylindrical inserts have a diameter of 1.25 cm and consist of acrylic, low density polyethylen (LDPE), polymethylpentene (PMP), polystyrene, Delrin® (polyoxymethylene) and Teflon® (polytetrafluoroethylene). The two remaining cylindrical slots seen in figure 5.4.1 correspond to air holes. The RSPs of the materials were determined with an R80 measurement (see section 5.1) using protons and helium ions. The results are listed in table 5.4 and compared to the relative electron density $\eta$ as given in the CTP manual. If the ionization potential of the investigated material is assumed to be equal to the one of water (which is an appropriate assumption for tissue-like materials), $\eta$ equals the RSP. As seen in table 5.4, the measured RSPs nevertheless differ from the value given in the user manual. This arises from the specific material definition used in the Monte Carlo simulation, which does not exactly represent all the original material features (e.g., small differences in the density or composition of materials). As expected, the RSPs obtained from both R80 measurements (protons and helium ions) correspond well to one another.

### 5.4.2 Simulation setup

As the iCT demonstrator presented in section 4.2 is too small to image phantoms of the size of the CTPs, an imaging system of adequate size (covering the whole phantom area) was modelled in Geant4 `10.05.p01` using the physics list QGSP_BIC. The simulated setup corresponds to an idealized version of a realistic imaging setup, which allows investigating a reconstruction workflow in a more generalized way, hence, without strong influence of a specific imaging setup on the reconstruction result.

The simulated setup that was used for subsequent reconstructions is displayed in figure 5.4.2. It consists of four silicon trackers with a thickness of 300 µm each. This corresponds to a typical sensor thickness, as for example used for the tracker planes of the iCT demonstrator system presented in section 4.2. In the simulation, ideal (infinite) spatial reso-

Table 5.4: RSPs of the CTP404 (sensitometry) module as obtained using R80 measurements in a Geant4 simulation and as determined for the real phantom in the CTP user manual [125].

| **Material** | **RSP ($p^+$ simulation)** | **RSP ($He^+$ simulation)** | **$\eta$ (CTP user manual)** |
|---|---|---|---|
| Acrylic | 1.165 | 1.162 | 1.147 |
| Delrin® | 1.371 | 1.367 | 1.363 |
| PMP | 0.890 | 0.888 | 0.853 |
| LDPE | 0.987 | 0.984 | 0.945 |
| Teflon® | 1.850 | 1.849 | 1.868 |
| Polystyrene | 1.043 | 1.041 | 0.998 |

lution of the tracker planes was assumed. Furthermore, as for the idealized setup described in section 5.2.1, the energy measurement device was replaced by extracting the residual ion energy at the last tracker plane. In this case, the last detector plane corresponds to the fourth tracker module, which is marked as D4 in figure 5.4.2.

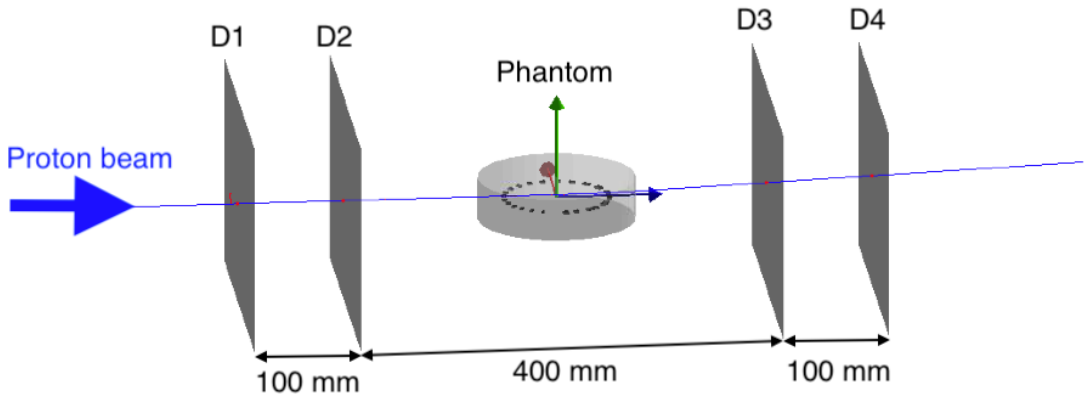


Figure 5.4.2: Monte Carlo simulation setup for the imaging of CTP modules. The simulated imaging apparatus corresponds to an idealized version of a realistic iCT scanner and only consists of four tracker planes. Instead of a separate device for the energy measurement, the residual ion energy was extracted from the fourth detector plane (D4). The figure was taken from Kaser et al. [126].

As primary particles, a parallel proton beam with an energy of 200 MeV was used and 90 projections were created (every 2° over a total angular range of 180°). Two options were investigated: using 800 protons per $mm^2$ and using 8000 protons per $mm^2$ to compensate the particle rejection introduced by the position cuts, as it will be discussed in section 5.4.3. As will be seen in section 5.4.5, the increased number of primaries improves the imaging result as expected. However, this particle fluence lies far above typically used particle fluences for ion imaging (e.g., 900 protons per $mm^2$ [65] or 100 protons per $mm^2$ [127]).

Finally, the reconstruction workflow was also tested with helium ion data obtained from Monte Carlo simulations. To compare them to reconstructions using protons, the same particle fluence (800 p/$mm^2$), the same energy (200 MeV/u) and the same position cut (2 mm) were used. An ideal filtering algorithm was assumed, since the simulations allowed to exclude the fragments of the primary helium particles from the imaging data set by identifying them via their particle ID.

### 5.4.3 Projection value definition

In section 5.2.2, a projection definition that returns the material parameter $\alpha$ as used in the Bragg-Kleeman rule as the reconstruction result was discussed. Although this definition showed promising results for the phantoms investigated in section 5.2.4, it causes some difficulties, which are discussed in the following. To obtain the RSP starting from $\alpha$, one has to insert the beam energy into the Bragg-Kleeman rule and divide the result by the expected SP of water. Especially if the energy loss in the phantom is high (as it would be the case for large phantoms), it would be better to directly obtain the RSP in the reconstruction, as this quantity is not strongly depending on the beam energy over a wide energy range. For this reason, Kaser et al. [123] discussed a projection definition, which defines the water-equivalent path length (WEPL) via the range. As discussed in section 2.5.3, the reconstruction directly returns the RSP if the projection is defined through the WEPL, which itself is defined as [123]

$$\mathrm{WEPL} = \int_{\tau} \mathrm{RSP}(x)\mathrm{d}x \approx \int_{E_{\mathrm{out}}}^{E_{\mathrm{in}}} \frac{\mathrm{d}E}{S(I_{\mathrm{water}}, E)}. \tag{5.4.1}$$

The integral can be further split in two parts, which correspond to the initial and the final ion range in water ($R_{\mathrm{water}}(E_{\mathrm{in}})$ and $R_{\mathrm{water}}(E_{\mathrm{out}})$, respectively) [123]

$$\mathrm{WEPL} = \int_{0}^{E_{\mathrm{in}}} \frac{\mathrm{d}E}{S(I_{\mathrm{water}}, E)} - \int_{0}^{E_{\mathrm{out}}} \frac{\mathrm{d}E}{S(I_{\mathrm{water}}, E)} = R_{\mathrm{water}}(E_{\mathrm{in}}) - R_{\mathrm{water}}(E_{\mathrm{out}}). \tag{5.4.2}$$

To obtain the expected ion range at the initial and residual ion energy, the range definition of Donahue et al. [24] (see equation (2.1.16)) was used, as the model is more accurate than the two-parameter Bragg-Kleeman rule that was used before. The material parameters that define the exact shape of the model were published for protons in Donahue et al. [24]. For helium ions, the model of the ion range was calibrated with NIST data [128] in a range from 5 MeV to 250 MeV using the least squares algorithm implemented in Python's `scipy` module [129].

In addition to the standard $3\sigma$ cuts on particle energy and scattering angle, position cuts as introduced in section 5.2.3 were applied to the data. Three different options were investigated: using a 2 mm position cut (the strictest possible position cut using protons as a stricter cut would create holes in the projection data), a 3 mm position cut and using no position cut at all (reference reconstruction). A 2 mm position cut rejected over 90 % of proton tracks in the phantom centre, while at the phantom edge, approximately 70 % of particles were removed from the data set (for helium ions, a rejection rate between 34-75% was determined). For a 3 mm position cut, 80 % of proton tracks were rejected in the phantom centre, while at the edges, close to 50 % of tracks were cut [123].

### 5.4.4 Analysis

For all reconstructions, the central slice was analysed. Regarding the reconstructions of the CTP528 high resolution module, the achievable line pair resolution is of interest. As in Volz et al. [13], the modulation transfer function (MTF) was defined via the maximum-to-minimum contrast of the RSP line pair profile, which was drawn through each insert. The principle of this analysis is demonstrated in figure 5.4.3 and a custom analysis software was developed to determine if the RSP value at a position $a_i$ along the line profile equals a local maximum or minimum in a certain interval $[a_i - b, a_i + b]$. The interval size, which is determined by parameter $b$, was adjusted to the thickness of the respective line pair insert [123]. If a value in such an interval was found to be larger or smaller than all other RSP values in the interval, it was counted as maximum ($\mathrm{RSP}_{\mathrm{max}}$) or minimum ($\mathrm{RSP}_{\mathrm{min}}$), respectively. If the number of identified maxima and minima did not match the actual count of the insert, the line pair was

excluded from the analysis (contrast was regarded as too low). With the correctly identified RSP maxima and minima, the MTF was calculated as [13, 123]

$$\mathrm{MTF}(i) \approx \frac{\langle \mathrm{RSP}_{\max} - \mathrm{RSP}_{\min} \rangle}{\mathrm{RSP}_{\mathrm{ref,max}} - \mathrm{RSP}_{\mathrm{ref,min}}}, \tag{5.4.3}$$

with the reference values $\mathrm{RSP}_{\mathrm{ref,max}}$ and $\mathrm{RSP}_{\mathrm{ref,max}}$ taken from an R80 measurement. They were identified to be 1.125 for the aluminium line pars and 1.165 for the acrylic body, respectively. If the MTF falls below 10 %, the image resolution was regarded to be too low to correctly resolve the respective line pair. This limit is typically used in literature [13, 130]. Note that equation (5.4.3) corresponds to an approximation of the MTF and resulting intensity values reported in this work should hence be regarded as approximate values.

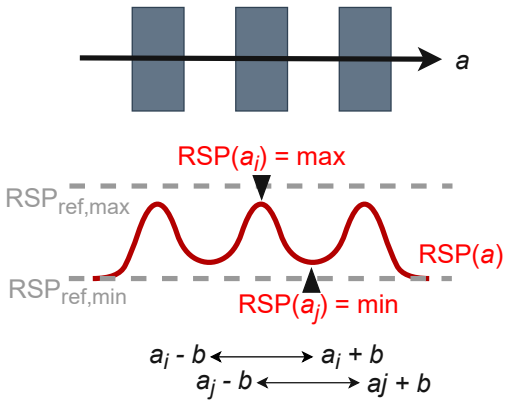


Figure 5.4.3: Definition of the approximate MTF via the line pair contrast. Figure from Kaser et al. [123] (adapted).

For the CTP404 sensitometry module, a quadratic ROI was defined in the centre of four cylindrical inserts, namely LDPE, PMP, Teflon® and Delrin®. These inserts were chosen because two of them (LDPE and PMP) have an RSP below the one of water ($\mathrm{RSP}_{\mathrm{water}} = 1$) and the other two (Teflon®, Delrin®) have an RSP above the one of water. The exact values for the reference RSPs can be found in table 5.4. The ROI in each insert had a size of $(10 \times 1 \times 10$ voxels), which corresponded to an area of $(5 \times 5)\,\mathrm{mm}^2$. The ROI was chosen to be smaller than the actual insert size to exclude edge effects from the analysis [123].

### 5.4.5 Results

The projections created in Geant4 were used as input data for the TIGRE toolbox (see section 3.4), where two of the implemented reconstruction algorithms were employed. As in section 5.2.4, OS-SART (described in section 2.5.3), was used to reconstruct a 3D image from the projection data. 30 iterations and a block size of 10 were used (more iterations did not further improve the result). Furthermore, adaptive-steepest-descent-projection onto convex sets (ASD-POCS) was used to reconstruct RSP maps as algorithms of this family are expected to perform well with limited or noisy projection data [68], which was expected to be of advantage if many protons were removed from the data set by position cuts. For the latter algorithm, the number of iterations was determined using the default stopping criteria as implemented in TIGRE [123].

The CTPs were reconstructed with a voxel size of $(0.5 \times 0.5 \times 0.5)\,\mathrm{mm}^3$. The image reconstruction of a $400 \times 20 \times 400$volume (central part of the phantom) with the TIGRE toolbox from 90 projections on an NVIDIA Quadro K620 graphics card depended on the reconstruction algorithm. For the OS-SART, a reconstruction time of 10 s was recorded, the reconstruc-

tion time using ASD-POCS depended on the number of iterations until convergence (6 to 13 iterations corresponding to a reconstruction time of 16 s to 32 s).

In the following sections, reconstruction results using protons and helium ions as primary particles for the imaging, are discussed.

#### 5.4.5.1 Protons

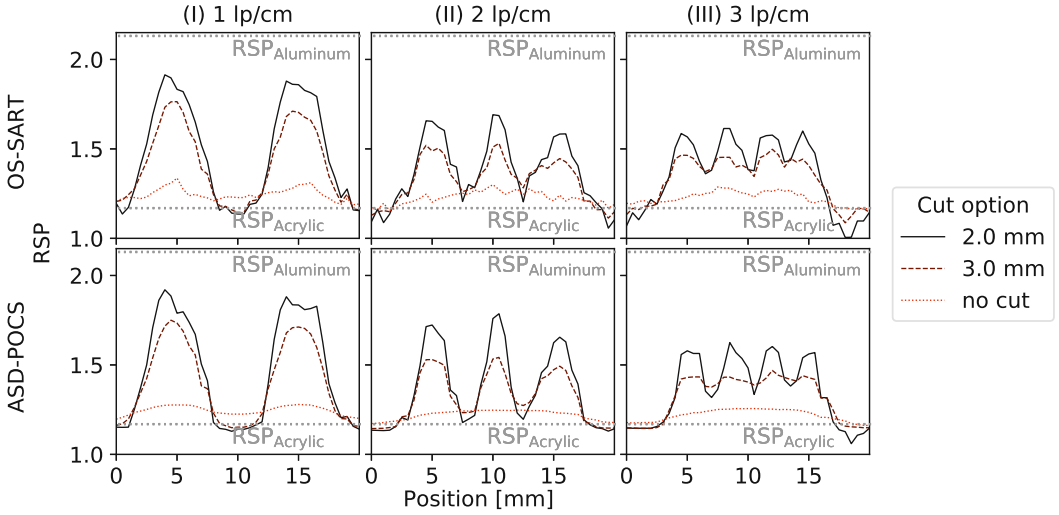


Figure 5.4.4: Line profiles through the first three CTP528 inserts using a 2 mm, a 3 mm and no position cut in addition to the standard $3\sigma$ cuts on particle energy and scattering angle. The reconstructions in the top row were obtained with OS-SART, while the reconstructions in the bottom row were obtained using ASD-POCS. The figure was taken from Kaser et al. [123].

Figure 5.4.4 shows the RSP profiles through the first three line pairs of the reconstructed CTP528, further referred to as insert I, II and III. In the top row, the reconstruction results with OS-SART are displayed, while the bottom row refers to reconstructions obtained with ASD-POCS. The effect of the position cuts is apparent: for the strictest position cut (2 mm), the maximum values along the RSP profile through the insert are closer to the reference value (dotted gray line) as compared to other cut options. This is also evident in the resulting approximate MTF values, as obtained from equation (5.4.3), which are displayed in table 5.5 for a 2 mm and a 3 mm position cut and OS-SART and ASD-POCS reconstructions.

Table 5.5: Approximate MTF values for the CTP528 inserts using a 2 mm and a 3 mm position cut and the ASD-POCS and OS-SART for reconstruction.

| **Algorithm** | **Position cut [mm]** | **MTF$_{\text{Insert I}}$** | **MTF$_{\text{Insert II}}$** | **MTF$_{\text{Insert III}}$** |
|---|---|---|---|---|
| OS-SART | 2 | 0.79 | 0.46 | 0.19 |
| OS-SART | 3 | 0.62 | 0.24 | - |
| ASD-POCS | 2 | 0.80 | 0.56 | 0.26 |
| ASD-POCS | 3 | 0.60 | 0.28 | 0.05 |

To compensate for the data rejection introduced by the 2 mm position cut, additional reconstructions with increased particle fluence were generated (8000 p/mm$^2$, as introduced in section 5.4.2). The resulting data sets were reconstructed with OS-SART and ASD-POCS. Almost the same MTF values were obtained with the increased statistics. For example, an MTF value of ≈0.42 was obtained for insert II, when OS-SART was used for the reconstruction

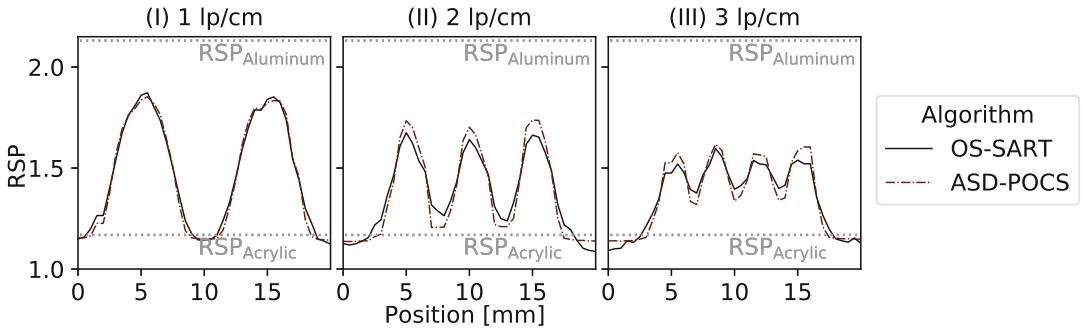


Figure 5.4.5: Line profiles through the first three CTP528 inserts using a 2 mm position cut. The reconstructions were performed with OS-SART and ASD-POCS. The figure was taken from Kaser et al. [123].

(for 800 p/mm$^2$, a value of ≈0.46 was achieved) [123]. However, a smoother line pair profile was obtained with increased statistics, as it can be visually observed in figure 5.4.5.

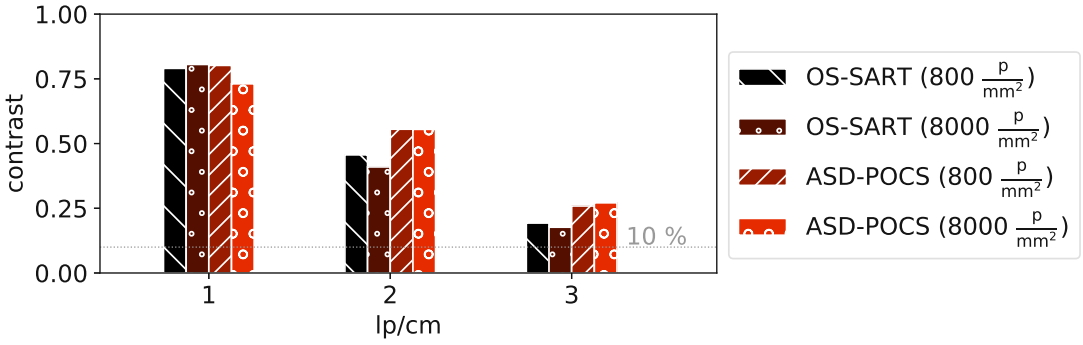


Figure 5.4.6: Maximum-to-minimum line pair contrast for the CTP528 inserts (corresponding to the approximate MTF values) using a 2 mm position cut. The figure was taken from Kaser et al. [123].

The approximate MTF values for the first three line pair inserts of the CTP528 are displayed in figure 5.4.6. It can be seen that ASD-POCS outperforms OS-SART reconstructions in most cases. For visual comparison between the algorithms, the central slices for the reconstructions using a 2 mm position cut are displayed in figure 5.4.7.

While the CTP528 was used to analyse the spatial resolution of the reconstruction workflow, the CTP404 (sensitometry) was used to analyse the RSP accuracy, as described in section 5.4.4. Figure 5.4.8 shows the obtained RSP distribution in each ROI (PMP, LDPE, Delrin® and Teflon®) for reconstructions using a primary proton fluence of 800 p/mm$^2$ and either a 2 mm position cut, a 3 mm position cut or no position cut. Again, OS-SART and ASD-POCS were used for image reconstruction. It was observed that the reconstruction algorithm did not have a strong influence on the average RSP obtained within a ROI. For the PMP insert, average RSP values between 0.879 and 0.886 were determined for all reconstruction options. However, the position cut had an apparent impact on the reconstruction result. For the Teflon® insert, which has the highest RSP of all CTP404 inserts, a strong deviation from the reference value ($RSP_{ref}$=1.85) was found when no position cut was used. For OS-SART and ASD-POCS reconstruction, average values of 1.764 and 1.762 were determined, which is almost 5 % below the reference value [123]. With a 2 mm position cut, the average values increased to 1.824 (OS-SART) and 1.822 (ASD-POCS). On the other hand, the position cuts increase the image noise due to the high data rejection rate. This can be observed via the increased spread of RSP values within a specific insert. For example,

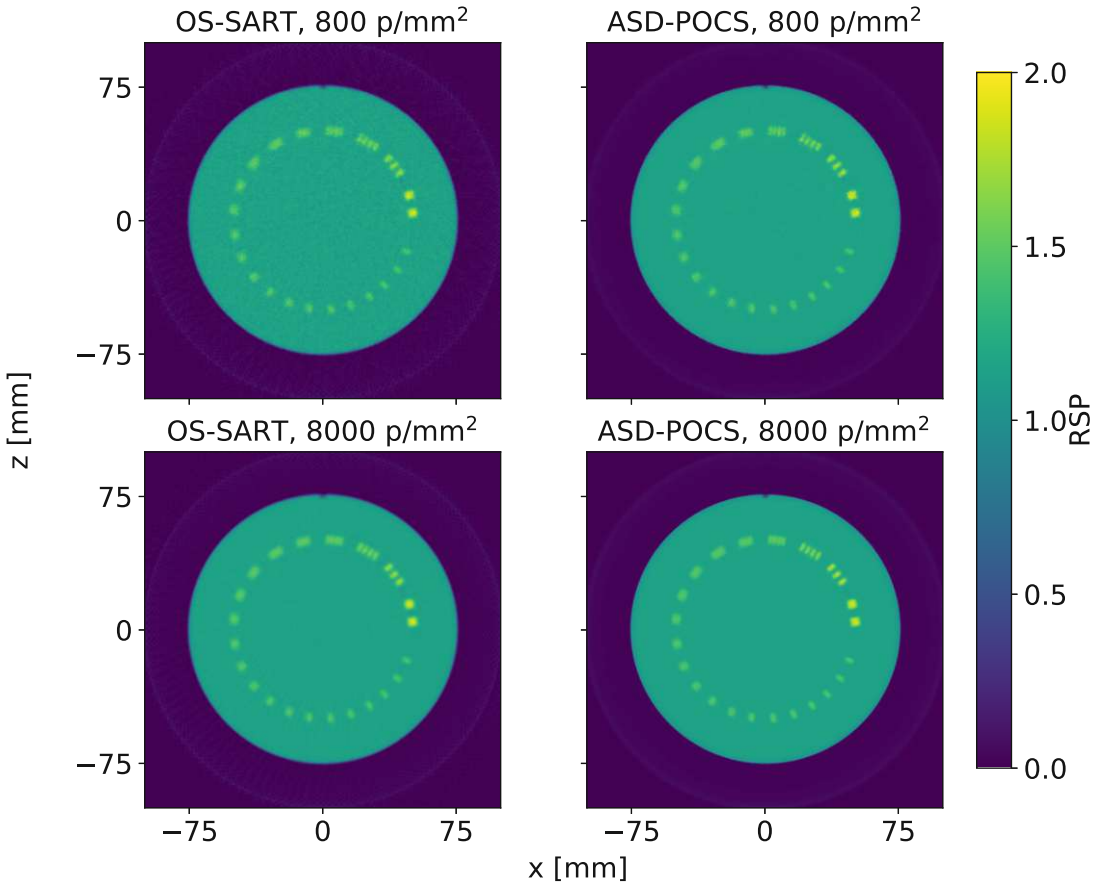


Figure 5.4.7: Central slices of the CTP528 using 800 protons per mm$^2$ (top row) and 8000 protons per mm$^2$ (bottom row). OS-SART (left) and ASD-POCS (right) were used for the reconstructions. The figure was taken from Kaser et al. [123].

RSPs between 0.914 and 1.043 were obtained for the OS-SART reconstruction using a 2 mm position cut, while the standard $3\sigma$ cuts resulted in values between 0.964 and 1.008.

As seen in figure 5.4.8, ASD-POCS reduces image noise compared to OS-SART. This also reduces the difference in the RSP range between different cut options. For a 2 mm position cut, values between 0.964 and 0.986 were obtained, while the reconstruction without position cut yielded RSPs between 0.971 and 0.986.

As for the CTP528, reconstructions using a 2 mm position cut and increased statistics (8000 p/mm$^2$) were analysed. The resulting box plots for each ROI are shown in figure 5.4.9. The increased statistics did not strongly affect the obtained average values. For the PMP insert, average values of 0.883 (OS-SART) and 0.884 (ASD-POCS) were determined (using 800 p/mm$^2$, values of 0.886 and 0.884 were obtained, respectively). However, as expected, the increased particle statistics had an impact on the spread of RSPs in one homogenous ROI. Regarding again the PMP insert, values between 0.825 and 0.960 were found using 800 p/mm$^2$ and OS-SART for the image reconstruction (corresponding to a range of $\Delta$RSP = 0.135). With increased statistics, this range of values could be reduced to $\Delta$RSP = 0.073, as values were only obtained between 0.845 and 0.918.

ASD-POCS generally resulted in a lower RSP spread as compared to OS-SART reconstruction. Using 800 p/mm$^2$ and a 2 mm position cut, values between 0.879 and 0.889 ($\Delta$RSP = 0.010) were obtained in the PMP insert. This was only slightly improved with increased statistics (8000 p/mm$^2$), where values between 0.881 and 0.887 ($\Delta$RSP = 0.006) were determined in the respective ROI.

The central slices of all reconstructions using a 2 mm position cut are displayed in fig-

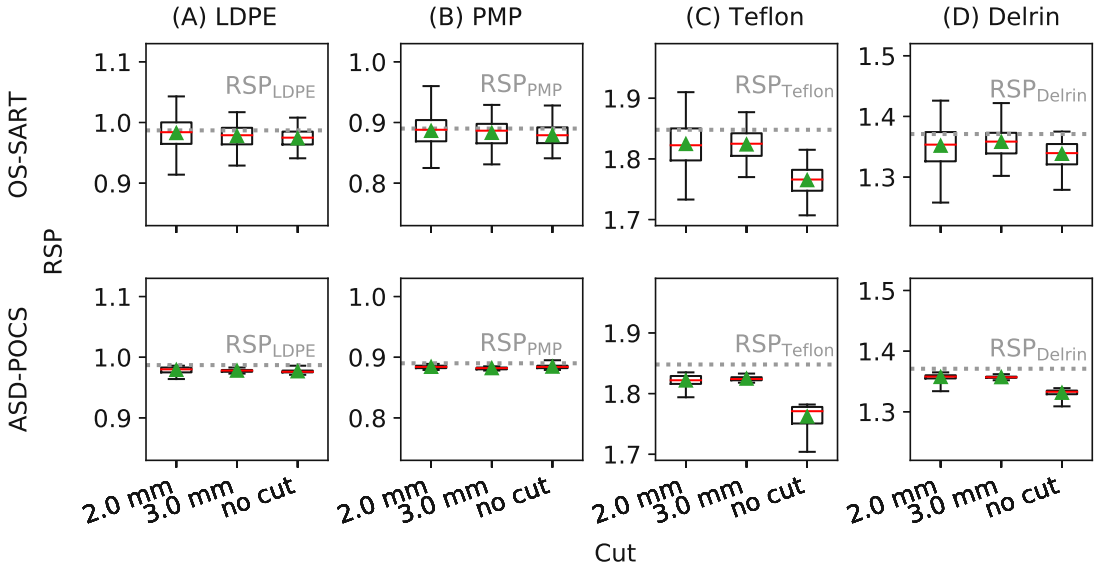


Figure 5.4.8: RSP in the CTP404 inserts using 800 p/mm$^2$ and three different position cuts in addition to the standard $3\sigma$ cuts on particle energy and scattering angle: 2 mm, 3 mm and, as a reference, no position cut. Median RSP values are marked with a red line, while the average value is highlighted by a green triangle. The figure was taken from Kaser et al. [123].

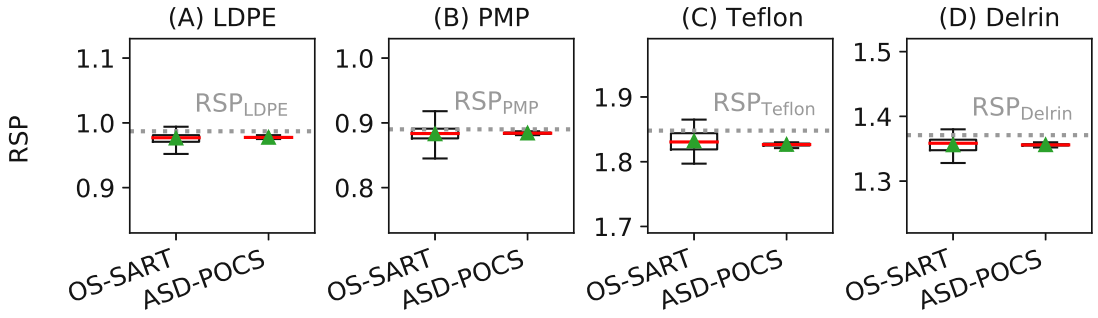


Figure 5.4.9: RSP in the CTP404 inserts using 8000 p/mm$^2$ and a 2 mm position cut. Median RSP values are marked with a red line, while the average value is highlighted by a green triangle. The figure was taken from Kaser et al. [123].

ure 5.4.10. Regarding the OS-SART reconstruction with 800 p/mm$^2$ (top left), the increased image noise as compared to the other reconstructions can be visually observed.

As described in section 5.4.4, the ROIs in the CTP404 inserts were selected to be smaller than the actual insert size to exclude edge effects from the analysis. One of them is the partial volume effect, which was described for positron emission tomography (PET) by Soret et al. [131]. As a result of the limited spatial resolution of a reconstructed image and voxels that do not perfectly match the shape of a (curved) insert, RSPs are expected to differ from their theoretical reference values. This is displayed in figure 5.4.11, where a zoomed-in view of the Teflon® insert of all reconstructions using a 2 mm position cut is given in the top row. In the bottom row, the RSP line pair profile through the centre of the insert is displayed. At the insert borders, the RSP does not decrease or increase sharply, but continuously rises to its final value. Furthermore, figure 5.4.11 shows again that ASD-POCS suppresses image noise, as smoother RSP curves were obtained for the respective reconstructions.

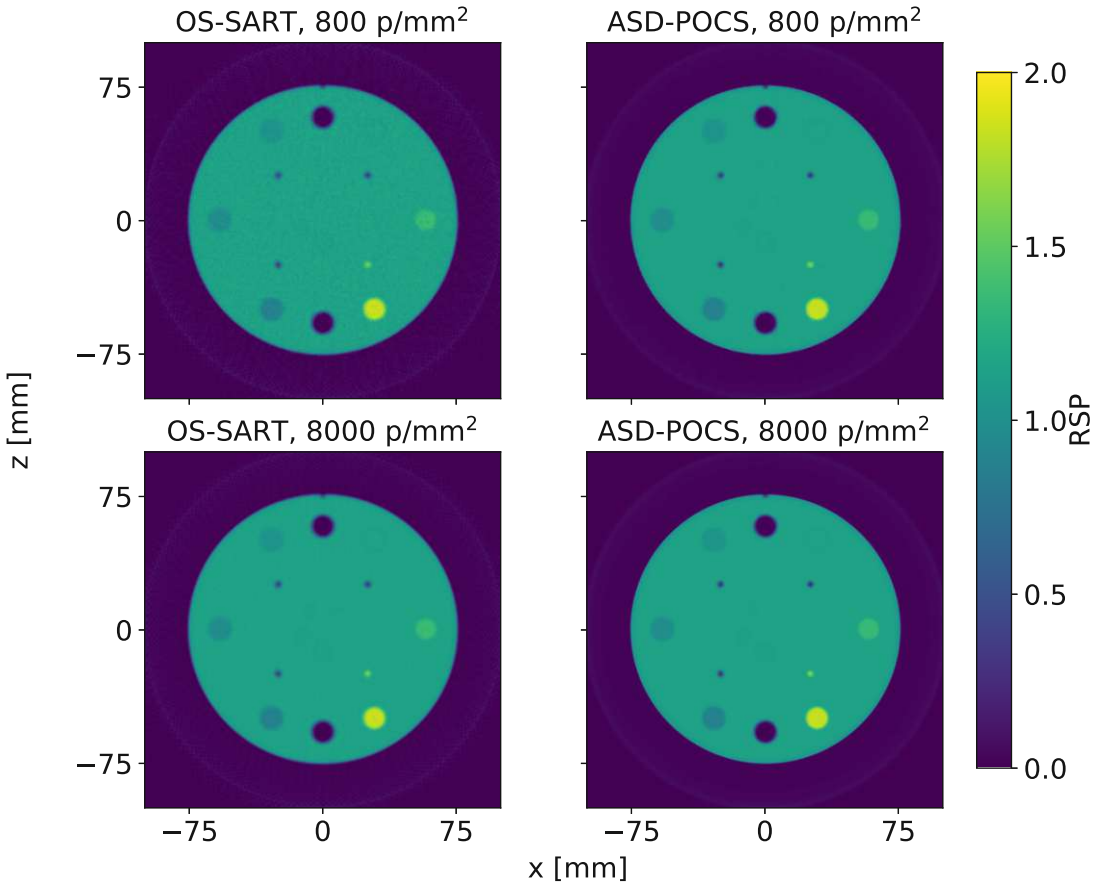


Figure 5.4.10: Central slices of the CTP404 using (top row) and (bottom row). OS-SART (left) and ASD-POCS (right) were used for the reconstructions. The figure was taken from Kaser et al. [123].

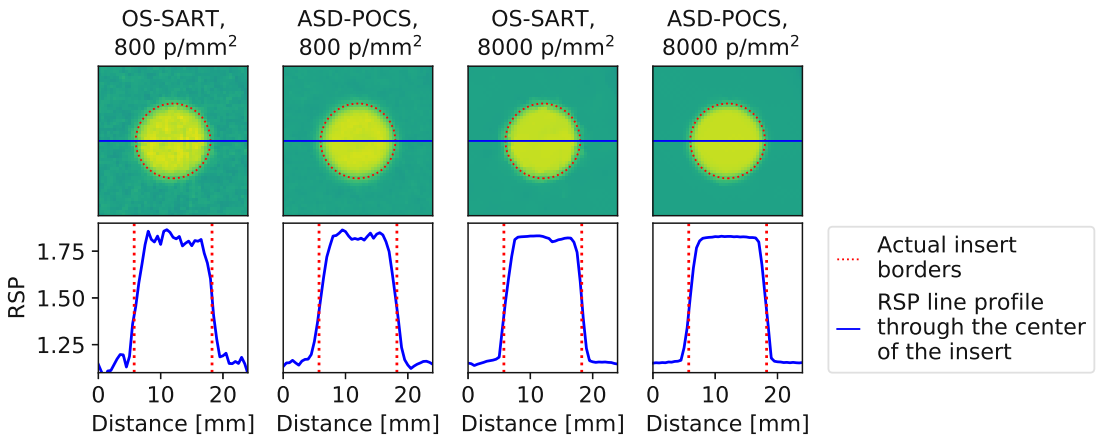


Figure 5.4.11: Demonstration of the partial volume effect for the Teflon® insert. The actual insert borders are marked with a red dotted line. The RSP line profile (blue solid line) was drawn through the insert centre and is displayed in the bottom row. The figure was taken from Kaser et al. [123] (adapted).

#### 5.4.5.2 Helium ions

The results discussed in this section were presented in the conference proceedings of the Fully3D conference 2021 [124]. To compare reconstructions using helium ions with the previously presented reconstructions with protons, the same position cut was used (2 mm). In

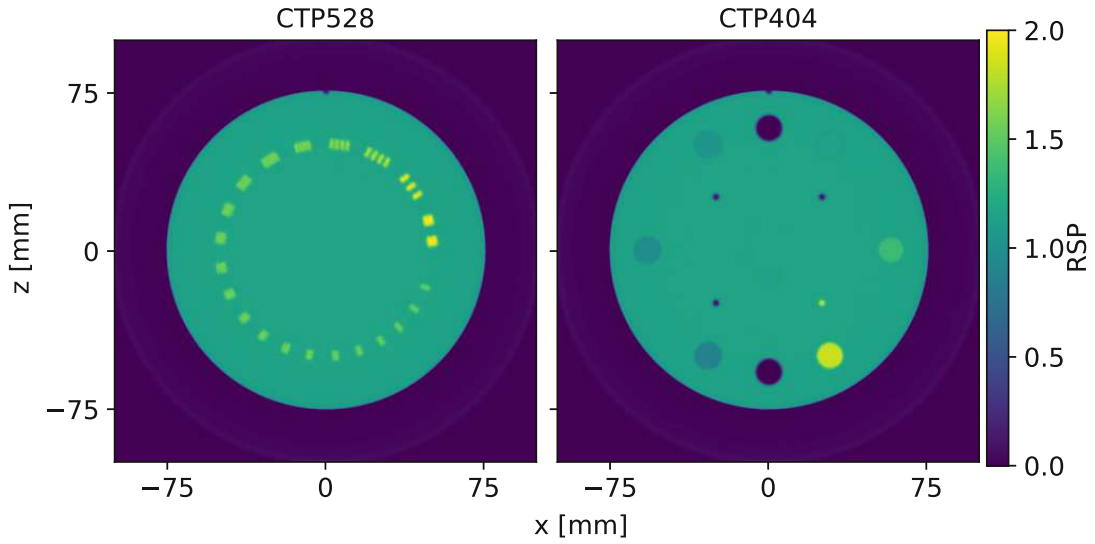


Figure 5.4.12: Reconstructed central slices of CTP528 and CTP404 using helium ions. The figure was taken from Schramm et al. [124].

section 5.4.5.1, it was shown that ASD-POCS outperformed OS-SART reconstructions in terms of image noise and approximate MTF values (line pair contrast). Therefore, the RSP map was only reconstructed from the simulated imaging data with helium ions (90 projections using 800 p/mm$^2$) using this algorithm. As discussed in section 5.4.2, an ideal filtering of projectile (and target) fragments was assumed, as only the data of helium ions were extracted from the Monte Carlo simulation data. In a real scenario, helium fragments such as protons, deuterons and tritons would arrive at the downstream detectors. They result in image artefacts and hence have to be removed from the data set [13].

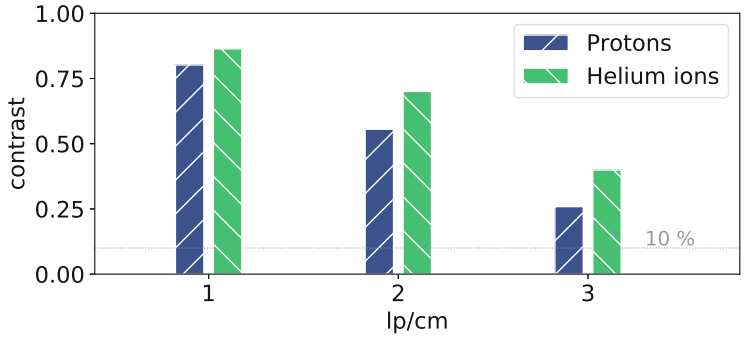


Figure 5.4.13: Approximate MTF values (maximum-to-minimum line pair contrast) for the inserts of the CTP528 (using protons and helium ions). The figure was taken from Schramm et al. [124].

Figure 5.4.12 shows the central slices of the reconstructed CTP528 (high resolution) and CTP404 (sensitometry). Both central slices were analysed according to the analysis described in section 5.4.4, which was also applied to the previously discussed reconstructions using proton data. The approximate MTF values (contrasts) of the first three line pair inserts is shown in figure 5.4.13 (green bars). For better comparison, the line pair contrasts that were obtained for protons (cf. figure 5.4.6), are again plotted in the image (blue bars). For all investigated inserts, a higher MTF was obtained with helium ions than with protons. While for insert III, the MTF already decreased to ≈26% using protons, an MTF of approximately 40% was still obtained for the reconstruction using helium ion data [124]. This effect is to be expected since - due to their higher mass - the path of helium ions through matter deviates

less from a straight line than the path of protons.

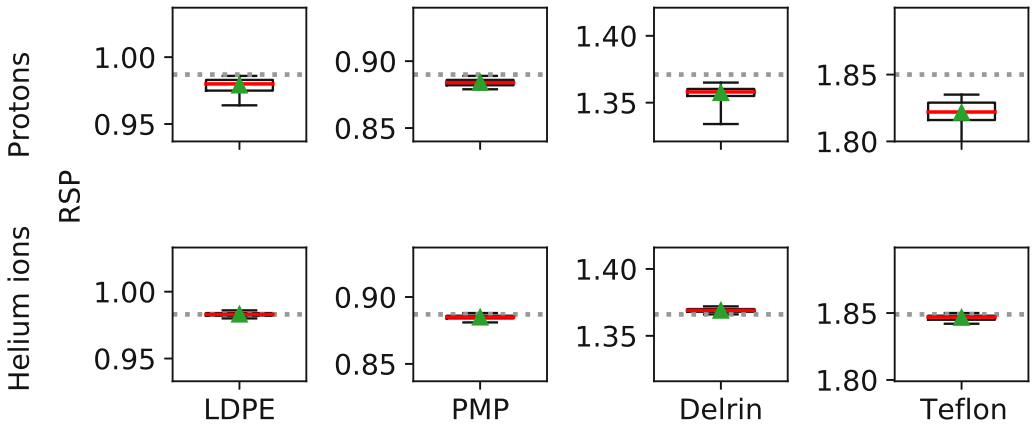


Figure 5.4.14: RSPs in the reconstructed CTP404 inserts (using protons and helium ions). The figure was taken from Schramm et al. [124] (adapted).

The RSP in the PMP, LDPE, Delrin® and Teflon® inserts of the CTP404 are displayed in box plots in figure 5.4.14 (bottom row). For better comparison, again, the already discussed results for protons were also added to the plot (top row). It is apparent that the spread of RSP values (image noise) is lower in case of helium ions as compared to the reconstruction using protons. Furthermore, it can be observed that the reconstructed average RSPs corresponded better to the reference values (see table 5.4) in case of RSPs that lie above the one of water (Delrin®, Teflon®). For example, a relative deviation from the reference value of approximately 1 % was determined for the Delrin® insert reconstructed with protons. For helium ions, the deviation from the reference was observed to be only 0.2 %.

## 5.5 TIGRE extension for ion CT

As seen in the previous section, the TIGRE toolbox allowed for a preliminary ion CT reconstruction workflow based on a straight line (SL) approach. Reconstruction results could be obtained in minutes and were improved in terms of RSP accuracy and line pair resolution by using position cuts (see section 5.2.3). However, the approach did suffer from the high data rejection rate due to these cuts. In that regard, an extension for the TIGRE toolbox was developed to achieve a more efficient and improved iCT image reconstruction with the framework. In the following sections, the methodology for the code extension and reconstruction results are discussed.

### 5.5.1 Implemented method

To obtain high resolution proton radiographs, Collins-Fekete et al. [132] proposed a binning procedure based on an maximum likelihood (ML) approach. In their approach, the volume between upstream and downstream tracker is divided in so-called channels, which correspond to a three-dimensional extension of the projection pixels to the source (see figure 5.5.1). For a parallel beam, the channel thickness is therefore constant, while for a cone beam, the channel size continuously increases from a point (source) to the final detector pixel size. For each channel $k$, the WET is calculated from the WEPL of $n$ protons that went through that channel according to their path estimate [56]

$$\mathrm{WET}_k = \frac{\sum_n^N \frac{l_{k,n}^2}{L_n^2} \mathrm{WEPL}_n}{\sum_n^N \frac{l_{k,n}^2}{L_n^2}}. \tag{5.5.1}$$

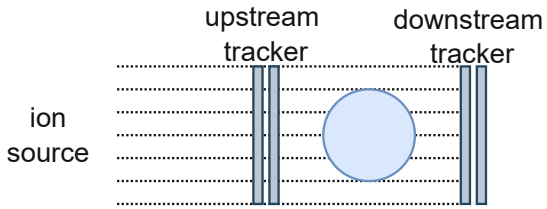


Figure 5.5.1: Definition of channels (dotted black lines) for a planar source as described by Collins-Fekete et al. [132]. The figure was taken from Kaser et al. [126].

Here, $l$ corresponds to the length a proton $n$ has spent in the respective channel $k$ and $L$ to the overall channel length. $l$ is calculated from the path estimate, where Collins-Fekete et al. [132] proposed an optimized cubic spline (see section 2.4.2). Although the approach was only presented for protons in Collins-Fekete et al. [132], the approach could also be applied for other ion species, as will be shown in section 5.5.6.2. As the high resolution pRads already contain the path information for each proton, the resulting projections can be used as input data for conventional x-ray CT reconstruction algorithms. Of course, the method could also be used as a stand-alone tool for proton radiography. In this work, the high resolution ion radiographs (iRads) were used as input data for the ASD-POCS, as it already showed promising results for ion imaging data (see section 5.4.5).

Two implementations of the radiographic binning approach were added to the TIGRE toolbox [126]:

- **Original (orig.):** This binning approach follows the original method for high resolution parallel and cone-beam iRad, as it was described by Collins-Fekete et al. [132]. This approach fits well if an iRad has to be generated and the convex hull of the object is not known. For the parallel beam, all channels share the same length (parallel lines from the detector pixels towards the source), whereas the channel sizes for the cone-beam geometry increases with the opening angle (detector pixels are connected with straight lines to the point source).

- **Improved (imp.):** In the radiographic binning process, a cylindrical hull surrounding the object is used. While for the CTP modules, this shape corresponds to the convex hull [133, 134], the implementation does not correspond to the convex hull for more complex shapes like a human head. Therefore, it will have to be refined in the future. Inside the hull, the curved path estimate (optimized cubic spline [56]) is calculated, whereas a straight-line approach is used in air.

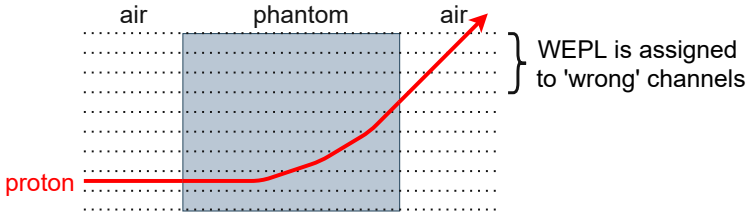


Figure 5.5.2: Without using an object hull, a proton WEPL could be assigned to multiple channels in air that did not mainly contribute to its energy loss. The figure was taken from Kaser et al. [126].

Using the improved binning approach, the assignment of an ion WEPL to channels, which only contributed little to a particle's energy loss (see figure 5.5.2), was rectified. This was achieved by introducing an additional weighting factor, which was multiplied to the contribution of ions to the respective channel. If an ion passed through the channel in air

(only a low energy loss is expected), the contribution factor $l_{k,n}^2/L_n^2$ was assigned with a weight $w_{\text{air}} = 0.00479$, which corresponds to the proton RSP of air according to Berger et al. [128]. On the other hand, inside the hull, the weighting factor is set to a higher value of $w_{\text{hull}} = 1$, corresponding to the RSP of water, which is a typical reference material for human tissues. If a channel lies fully outside (or inside) the hull, the additional weighting factor cancels out naturally.

### 5.5.2 Code structure

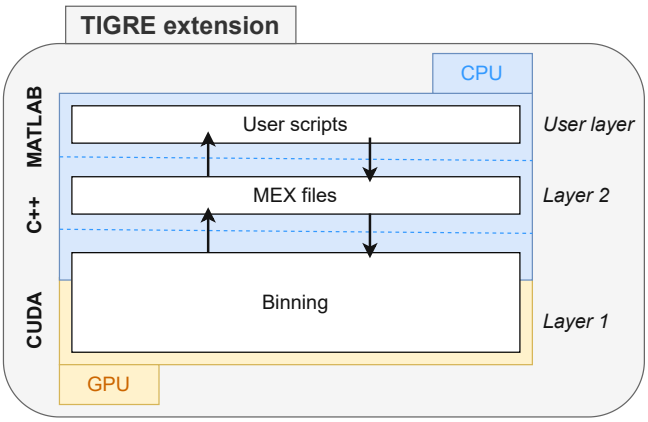


Figure 5.5.3: Structure of the code extension for the TIGRE toolbox.

A basic implementation of the code extension was discussed in Kirchmayer [135]. In the scope of this work, the code extension was adapted and complemented so that it could finally be published as part of the open-source TIGRE toolbox[1]. Figure 5.5.3 shows the structural design of the code extension, which closely follows the design of the toolbox (see section 3.4).

While the code can be invoked with a Matlab script (see appendix B), the actual binning process (calculation of the path estimate and its intercepts with the channels) is performed in the compute unified device architecture (CUDA) language. Default values for the maximum allowed channel intercepts were set using Monte Carlo simulations with different water blocks as phantoms (for a more detailed description, see Kaser et al. [126]). These maximum values are necessary, as the CUDA language does not allow for dynamic memory allocation without slowing down the code significantly. If more channel intercepts then the predefined vector size are determined, the specific proton is removed from the data set (it does not contribute to the pRad). As the given default values may not fit for each geometry, the user is able to adapt them during compile time.

### 5.5.3 Simulation setup for workflow verification

The iCT setup that was implemented in Geant4 and the Geant4 application for tomographic emission (GATE) corresponds closely to the setup described in section 5.4.2. It consisted of four silicon tracker modules and no calorimeter was modelled, as the residual ion energy was directly extracted from these tracking modules in the simulation. In contrast to the setup discussed in section 5.4.2, two implementations of the setup were created in the simulations to investigate the performance of the reconstruction under ideal and non-ideal conditions. The given descriptions closely follow the descriptions in Kaser et al. [126]:

- **Ideal setup:** The impact of the tracking system on the reconstruction result was minimized in this setup. Therefore, a thickness of only 1 µm was chosen for the tracking detectors. The energy and spatial resolution of the detectors were assumed to be

[1] https://github.com/CERN/TIGRE

ideal (infinite). The energy loss of the single ions in the phantom was determined by calculating the difference between the energies measured at D2 and D3 (at the upstream surface).

- **Non-ideal setup:** The thickness per tracking detector was set to 300 µm to analyse the performance of the reconstruction approach under more realistic conditions. This thickness corresponds to a typical size for tracking detectors, as for example the double-sided silicon strip detectors used for a proton computed tomography (pCT) demonstrator in Ulrich-Pur et al. [82]. The residual energy for each ion was obtained at the upstream surface of detector D4. It was subtracted from a fixed initial energy, corresponding to the average energy measured at the upstream surface of the tracker plane, which was located directly upstream of the phantom. A spatial resolution of $\sigma_s = 0.15\,\text{mm}$ (as in Khellaf et al. [136]) and an energy resolution of $\Delta E/E = 1\%$ were chosen. Detector effects were considered prior to any further calculation, and hence also affect the calculation of the particle directions and subsequently the ion path estimates.

#### 5.5.3.1 Phantoms

To analyse spatial resolution and RSP accuracy of the reconstructions obtained with the new code extension of the TIGRE toolbox, the CTP modules 528 and 404 were used. These phantoms were already described in section 5.4.1. For the reconstructions of these phantoms, 180 equidistant projections were generated in the Monte Carlo simulations over a total range of 360°. As initial particle fluence, 225 protons per $\text{mm}^2$ were chosen (which corresponds to the value used in Khellaf et al. [136]). While the CTP404 was reconstructed with a voxel size of $0.5 \times 0.5 \times 0.5$ $\text{mm}^3$, the CTP528 was reconstructed with a voxel size of $0.25 \times 0.25 \times 0.25$ $\text{mm}^3$ to account for the smaller insert sizes.

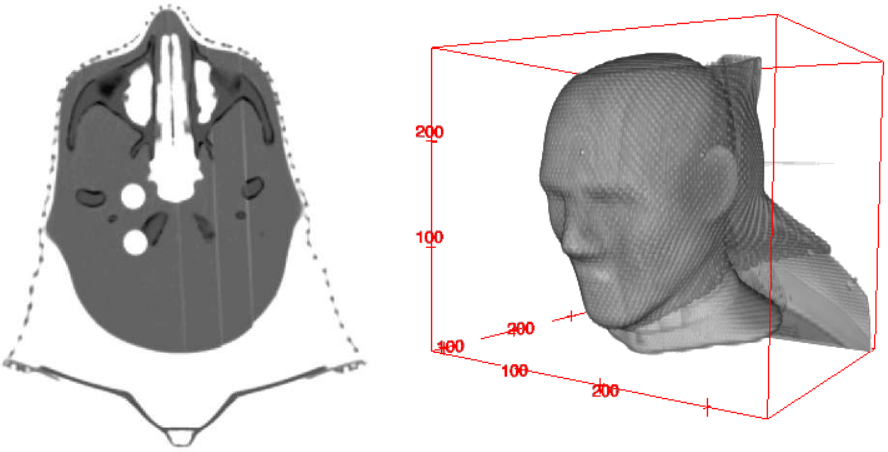


Figure 5.5.4: Slice (left) and 3D rendering (right) of the CIRS patient phantom (as obtained from an x-ray CT scan). The left part of the figure was taken from Kaser et al. [126].

Additionally, to investigate an anthropomorphic phantom, a CT scan of the 'phantom patient for stereotactic end-to-end verification (STEEV)' (CIRS, Norfolk, VA, USA)[2] [137], which is further referred to as *CIRS phantom*, was implemented as a phantom in the simulations. The Hounsfield unit (HU) of the scan were converted to materials using the correlation implemented in GATE [91]. One phantom slice is displayed on the left side of figure 5.5.4, while a 3D rendering of the phantom scan is seen in the right part of the image. 90 projections over a range of 180° and an initial particle fluence of only 50 protons per $\text{mm}^2$ were used

[2] I would like to thank Barbara Knäusl (Medical University of Vienna) and Markus Stock (MedAustron) for providing the CT image of the phantom.

for the reconstruction. The phantom was reconstructed with a voxel size of $0.68 \times 2.0 \times 0.68$ mm$^3$.

In all simulations, a parallel proton beam with an initial beam energy of 200 MeV was used (in Kaser et al. [126], also reconstructions using a cone-beam geometry can be found). However, some test reconstructions with a parallel beam of helium ions (200 MeV/u) were also performed with the new code extension of the TIGRE toolbox, see section 5.5.6.2.

### 5.5.4 Projection value definition

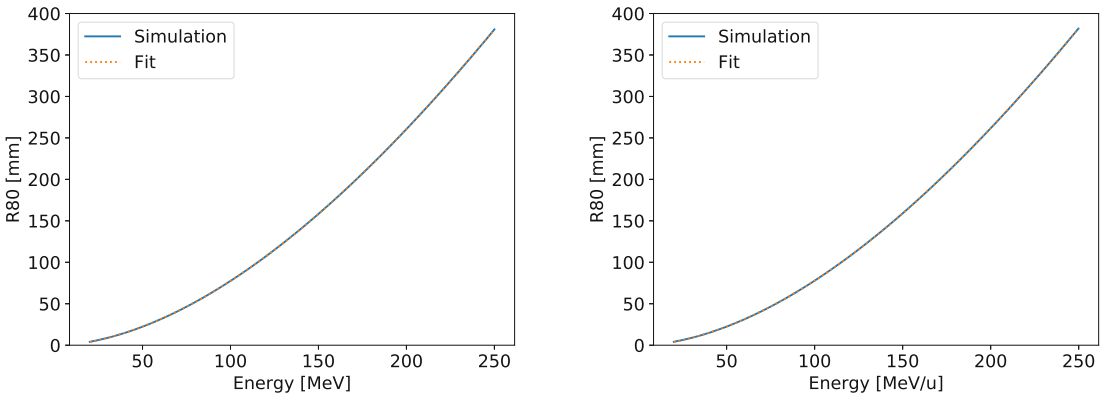


Figure 5.5.5: R80 measurements of proton (left) and helium ion (right) beams in water. The R80 measurements were implemented as a Geant4 simulation via GATE.

In sections 5.2.2 and 5.4.3, the WEPL, i.e., the projection value of the single protons, was defined via approximate range calculations using the models of Bragg and Kleeman [26] and Donahue et al. [24]. It is evident that the accuracy of this range model and its compliance with the ranges obtained in the simulation tool used has a direct impact on the RSP accuracy of the reconstruction result. Therefore, the projection value definition was refined in this section. In a GATE/Geant4 [88, 89] simulation, proton and helium ions beams were targeted at water cubes using various beam energies. The resulting ranges in water were then determined via the R80 method [119] (see section 5.1).

From these measurements, a third-order polynomial was fitted to the values using `scipy` [129]. The resulting curves for protons and helium ions in a range between 20 MeV/u and 250 MeV/u can be seen in figure 5.5.5. The fit was further used to calculate the WEPL of each specific ion $i$ as the difference of the corresponding R80 values of its initial and residual ion energy (as extracted from the simulations),

$$\mathrm{WEPL}_i = \mathrm{R80}(E_i^{\mathrm{in}}) - \mathrm{R80}(E_i^{\mathrm{out}}). \tag{5.5.2}$$

### 5.5.5 Analysis

As compared to section 5.4.4, the analysis of the CTP modules was slightly refined. For the CTP528 (high resolution module), the MTF was approximated by the maximum-to-minimum contrast within a specific line pair insert (see equation (5.4.3)). However, due to the higher image resolution obtained with the newly implemented reconstruction approach for iCT in the TIGRE toolbox (see section 5.5.1), the first eight line pair inserts were analysed (instead of only the first three inserts).

In the CTP404 (sensitometry module), ROIs with a size of 6 mm × 6 mm over the innermost 15 slices were defined in all inserts (corresponding to the method used in Ulrich-Pur et al. [138]). Subsequently, for each ROI, the relative error of the mean RSP was calculated as

$$\epsilon_{\mathrm{rel},j} = \frac{\mathrm{RSP}_{\mathrm{meas},j} - \mathrm{RSP}_{\mathrm{ref},j}}{\mathrm{RSP}_{\mathrm{ref},j}}. \tag{5.5.3}$$

Here, the measured average $\mathrm{RSP}_{\mathrm{meas},j}$ for each insert $j$ is compared to its reference value $\mathrm{RSP}_{\mathrm{ref},j}$, which can be found in table 5.4. The relative errors of all six inserts of the module were used to further calculate the mean absolute percentage error (MAPE) as

$$\mathrm{MAPE} = \frac{1}{6}\sum_{j=1}^{6} |\epsilon_{\mathrm{rel},j}|. \tag{5.5.4}$$

The signal-to-noise ratio (SNR) for each insert of the CTP404 was obtained as the ratio between the average RSP in an insert and its standard deviation $\sigma_{\mathrm{meas}}$

$$\mathrm{SNR}_j = \frac{\mathrm{RSP}_{\mathrm{meas},j}}{\sigma_{\mathrm{meas},j}}. \tag{5.5.5}$$

For the CIRS phantom, the reconstruction of the image slice shown in figure 5.5.4 (left) was compared to a RSP reference map[3] of the very same CT slice. The absolute RSP error $\Delta\mathrm{RSP}_i$ of each voxel $i$ is given via the difference between the measured value in a voxel $\mathrm{RSP}_{\mathrm{meas},i}$ and the reference value for the respective voxel $\mathrm{RSP}_{\mathrm{ref},i}$

$$\Delta\mathrm{RSP}_i = \mathrm{RSP}_{\mathrm{ref},i} - \mathrm{RSP}_{\mathrm{meas},i}. \tag{5.5.6}$$

The average absolute error in an ROI is then obtained by dividing the sum of all voxel errors by the respective voxel count $N$ in the respective ROI,

$$\Delta\mathrm{RSP}_{\mathrm{ROI}} = \frac{\sum_{i=1}^{i=N} |\Delta\mathrm{RSP}_i|}{N}. \tag{5.5.7}$$

In contrast to the CTP404, no relative RSP errors were analysed as multiple materials contribute to one ROI (for the CTP404 it was only one material per ROI). If one material with a large relative RSP error contributes to one ROI, the relative error of the whole ROI increases. This is the case if, for example, low-density materials like air contribute to a ROI. It is therefore more significant to state the average absolute RSP errors.

### 5.5.6 Results

The reconstruction results using proton beams (section 5.5.6.1) were published and discussed in Kaser et al. [126]. To demonstrate the performance of the reconstruction workflow for another ion species, iCT data using helium ions beams were created with Monte Carlo simulations and are discussed in section 5.5.6.2.

#### 5.5.6.1 Protons

In figure 5.5.6, the central slices of the reconstructed CTP528 are displayed (results obtained with an ideal data set, see section 5.5.3). On the left, the reconstruction result using the original pre-reconstruction binning method [132] is shown, while on the right side, the result obtained with the improved binning approach (with an object-surrounding cylindrical hull and channel weighting) can be seen. To allow for better visual comparison, the 5 lp/cm insert was highlighted and zoomed in.

Figure 5.5.7, shows the reconstructed central slices (original and improved binning approach) using a non-ideal data set. As compared to figure 5.5.6, the zoomed-in insert appears blurrier. As for the ideal data set, some small differences in the image contrast can already

[3] I would like to thank Paul Sommerer for his contribution in generating the RSP reference map of this phantom.

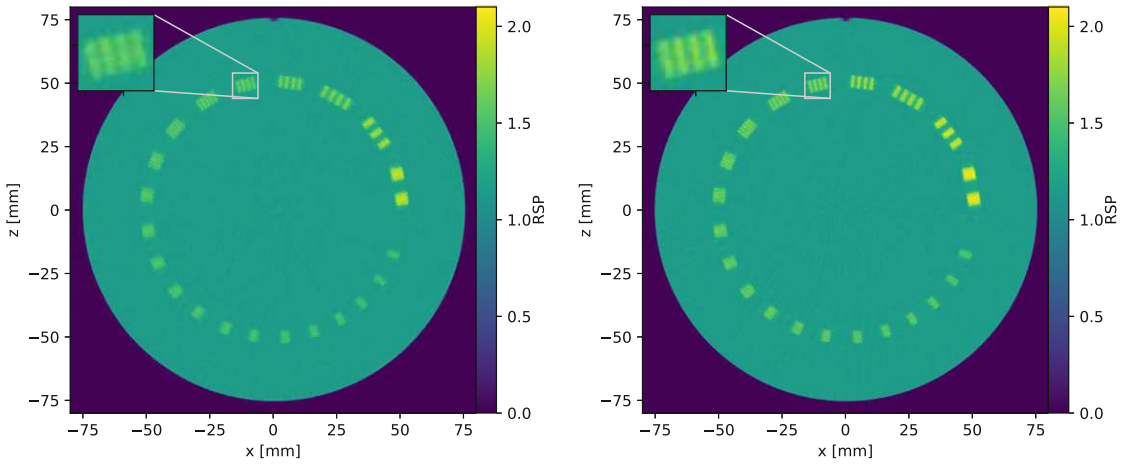


Figure 5.5.6: Central slices of the reconstructed CTP528 (ideal setup and using proton beams). A reconstruction using the original binning approach [132] (left) and the improved approach (right) are shown. The figure was taken from Kaser et al. [126].

be visually observed between the reconstruction using the original binning method and the improved approach with an object-surrounding cylindrical hull and channel weighting.

To analyse the actual line pair contrast of all reconstructions (ideal and non-ideal data set using the original and improved binning approach), the MTF was approximated as described by equation (5.4.3). The resulting profile is displayed in figure 5.5.8. As can be seen, the reconstruction results using the improved binning method with cylindrical hull and channel-weighting yielded higher MTF values than the reconstructions using the original binning method [132]. Regarding the results for the ideal data set in figure 5.5.8 (left), the MTF for the 5 lp/cm insert (which was highlighted in figure 5.5.6) was determined to be ≈13.1% using the original binning approach, while a value of ≈25.8% was obtained for the reconstruction using the improved binning approach. Using the improved approach, the 8 lp/cm insert still yielded a value of ≈12.7%, while the original approach resulted in a value of ≈4.2% for this insert, which is well below the $\mathrm{MTF}_{10\%}$.

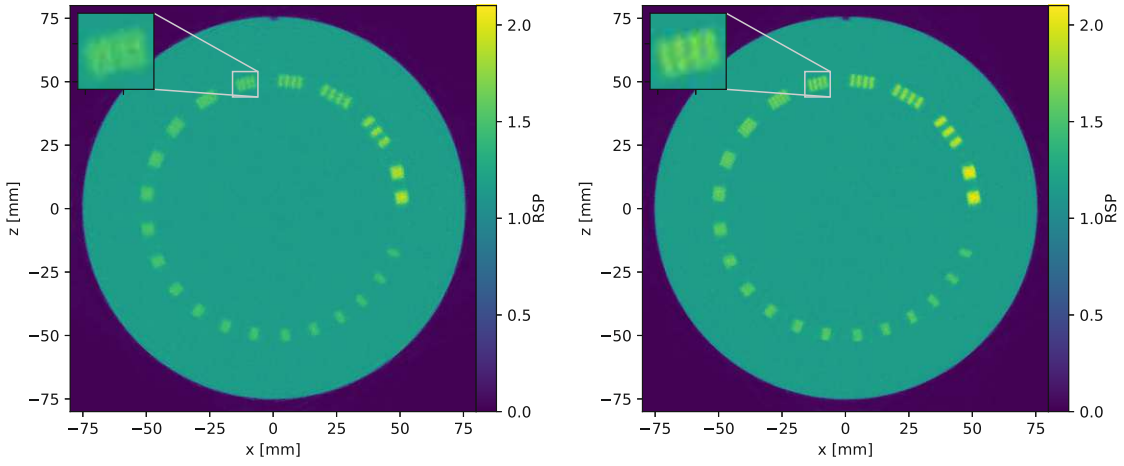


Figure 5.5.7: Central slices of the reconstructed CTP528 (non-ideal setup and using proton beams). A reconstruction using the original binning approach [132] (left) and the improved approach (right) are shown. The figure was taken from Kaser et al. [126].

For the non-ideal data set, approximate MTF values of ≈11.5% and ≈15.8% were obtained for the 5 lp/cm insert. For the subsequent insert (6 lp/cm), the approximate MTF value had already fallen below the threshold of the $\mathrm{MTF}_{10\%}$.

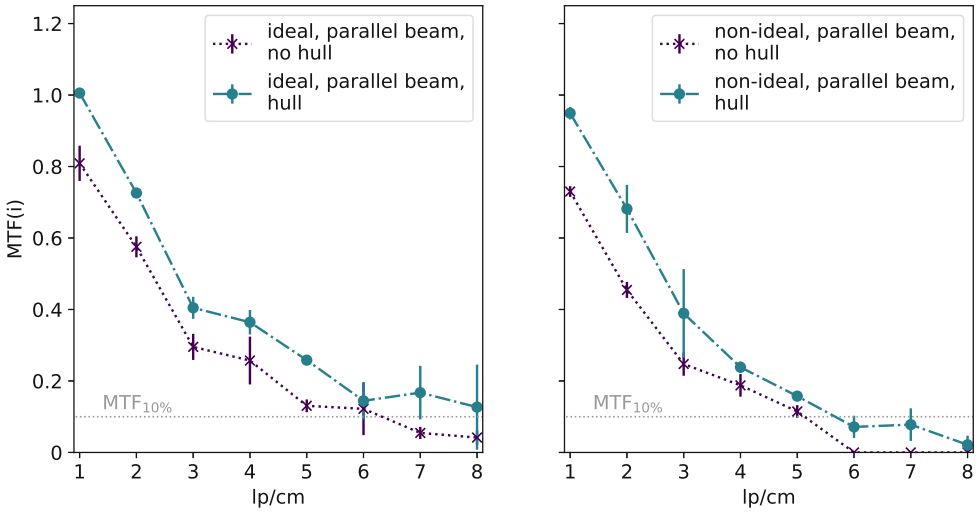


Figure 5.5.8: Approximated MTF for the CTP528 inserts using proton beams for imaging. The resulting line pair contrast (approximate MTF) for each insert $i$ is displayed in purple for the original binning approach [56] and in blue for the improved approach (with object-surrounding cylindrical hull and additional channel weighting). The dotted gray line represents the $MTF_{10\%}$. The figure was taken from Kaser et al. [126] (adapted).

In figure 5.5.9, the central slices of the CTP404 are displayed (using an ideal data set). On the left side, the reconstruction using the original binning method as described by Collins-Fekete et al. [132], is displayed while the reconstruction result on the right side was obtained using the improved approach with cylindrical hull and channel weighting (see section 5.5.1). Visually, only minor differences between the images can be observed. As for the CTP528, a second reconstruction with a non-ideal data set was generated. It is displayed in figure 5.5.10. Again, all phantom inserts can visually be distinguished from the phantom body.

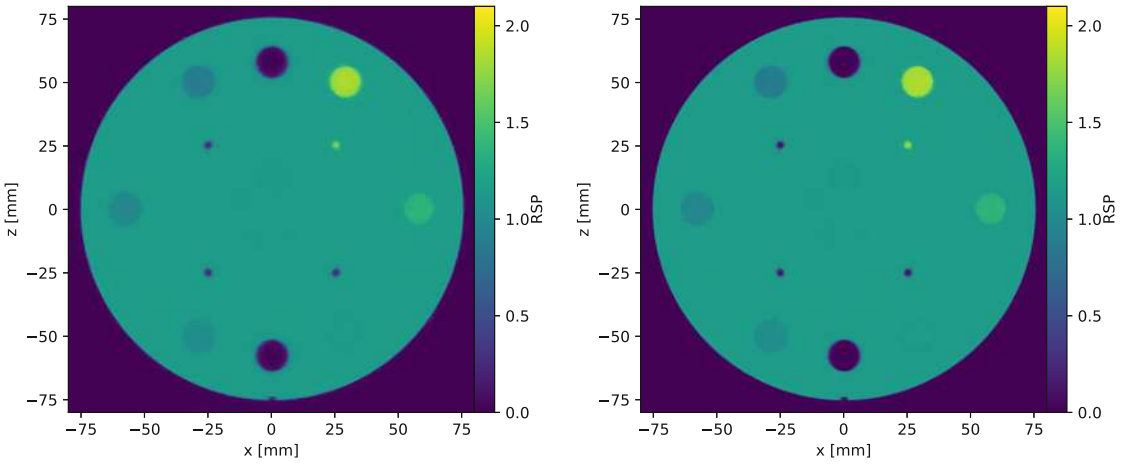


Figure 5.5.9: Central slices of the reconstructed CTP404 (ideal setup and using proton beams). A reconstruction using the original binning approach [132] (left) and the improved approach (right) are shown. The figure was taken from Kaser et al. [126].

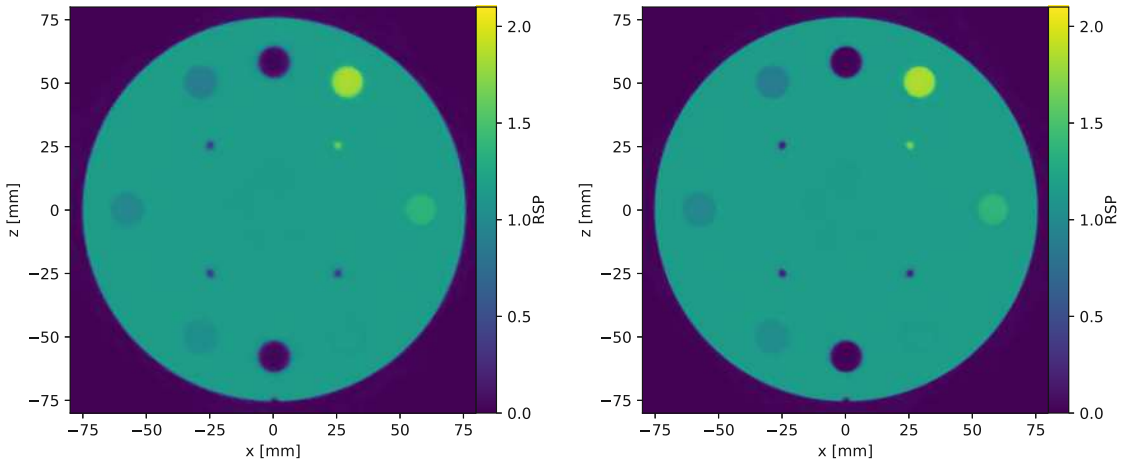


Figure 5.5.10: Central slices of the reconstructed CTP404 (non-ideal setup and using proton beams). A reconstruction using the original binning approach [132] (left) and the improved approach (right) are shown. The figure was taken from Kaser et al. [126].

To analyse the reconstructed RSP in the phantom inserts, the relative RSP errors were calculated for each insert and each reconstruction according to equation (5.5.3). From these errors, the MAPE was calculated as described by equation (5.5.4). The resulting values can be found in table 5.6. For all reconstructions, the MAPE was determined to be below 0.5 %, where the smallest value was recorded for the reconstruction of the ideal data set using the improved binning with object-surrounding cylindrical hull and the additional channel weighting factor (0.14 %). On the other hand, the highest MAPE was observed for the reconstruction of the non-ideal data set using the original binning approach without hull.

Regarding the RSP errors of the single inserts, the Teflon® insert resulted in the highest relative RSP error of the reconstructions using the original binning approach, which was found to be above 1 % (1.28 % for the ideal data set and 1.13 % for the non-ideal data set). For the reconstructions using the improved binning, all relative errors were found to be below 0.5 %. The highest value was observed for the Delrin® insert and the non-ideal data set (0.47 %).

Table 5.6: Relative RSP errors $\epsilon$ in the CTP404 inserts. Reconstruction results obtained with the *original* (orig.) approach followed the method for ion radiography described by Collins-Fekete et al. [132] (without hull) for the pre-reconstruction binning. The *improved* (imp.) method refers to the reconstruction results using an object-surrounding cylindrical hull and channel weighting in the binning process. An ideal and a non-ideal data set were used for the reconstruction, which are marked with the subscript $i$ and $n$, respectively. The values in this table were taken from Kaser et al. [126].

| **Method** | **Acrylic** | **PMP** | **LDPE** | **Teflon®** | **Delrin®** | **Polystyrene** | **MAPE** |
|---|---|---|---|---|---|---|---|
| $\epsilon_{\text{orig.},i}$ | -0.12% | 0.12% | 0.16% | -1.28% | -0.49% | 0.16% | 0.39% |
| $\epsilon_{\text{imp.},i}$ | -0.04% | -0.34% | 0.01% | -0.36% | -0.10% | 0.01% | 0.14% |
| $\epsilon_{\text{orig.},n}$ | 0.02% | 0.80% | 0.35% | -1.13% | -0.41% | 0.05% | 0.46% |
| $\epsilon_{\text{imp.},n}$ | 0.12% | 0.44% | -0.26% | -0.33% | 0.47% | -0.10% | 0.29% |

In table 5.7, the SNR ratio obtained for each insert and each reconstruction, is listed. Furthermore, the average SNR was calculated for each reconstruction. They lie in a similar range (between 230.0 and 263.7) for all reconstructions. However, regarding the SNR of the single insert, some differences can be observed between the reconstructions. For the results obtained with the original binning method [132], SNRs of the single inserts were found to spread between 170.3 and 301.7 for the ideal data set or 167.2 and 327.2 for the non-ideal data

set. For the reconstructions obtained with the improved binning, SNRs between 198.5 and 312.5 (ideal data set) or 215.3 and 324.4 (non-ideal data set) were obtained. Hence, a smaller spread of SNRs was observed for the improved binning option (using an object-surrounding hull and additional channel weighting).

Table 5.7: SNR in the CTP404 inserts. Reconstruction results obtained with the *original* (orig.) approach followed the method for ion radiography described by Collins-Fekete et al. [132] (without hull) for the pre-reconstruction binning. The *improved* (imp.) method refers to the reconstruction results using an object-surrounding cylindrical hull and channel weighting in the binning process. An ideal and a non-ideal data set were used for the reconstruction, which are marked with the subscript $i$ and $n$, respectively. The values in this table were taken from Kaser et al. [126].

| **Method** | **Acrylic** | **PMP** | **LDPE** | **Teflon®** | **Delrin®** | **Polystyrene** | **Avg. SNR** |
|---|---|---|---|---|---|---|---|
| $\mathrm{SNR}_{\mathrm{orig.},i}$ | 301.7 | 219.5 | 192.6 | 170.3 | 245.3 | 250.7 | 230.0 |
| $\mathrm{SNR}_{\mathrm{imp.},i}$ | 283.0 | 309.6 | 198.5 | 257.3 | 221.1 | 312.5 | 263.7 |
| $\mathrm{SNR}_{\mathrm{orig.},n}$ | 308.8 | 236.0 | 210.5 | 167.2 | 300.4 | 327.2 | 258.4 |
| $\mathrm{SNR}_{\mathrm{imp.},n}$ | 217.4 | 215.3 | 227.5 | 324.4 | 256.7 | 246.1 | 247.9 |

As discussed in section 5.5.3.1, a CT scan of an anthropomorphic phantom was used as phantom in the Monte Carlo simulations. A non-ideal data set was reconstructed from 90 projections using both implemented binning methods (original method for high-resolution ion radiography [132] and the improved binning using a cylindrical hull and additional channel weighting). A reconstructed slice of the phantom is displayed for both approaches in figure 5.5.11. Although the cylindrical hull does not represent the accurate convex hull of the phantom, some improvements could be seen in the reconstruction, which were quantified in the following analysis.

By comparing each voxel of the reconstruction with a reference RSP map, the absolute RSP error was calculated as described by equation (5.5.6). The resulting error map is displayed in figure 5.5.12. While the error in homogenous areas appears to be small, larger deviations from the reference value can be observed at transitions between materials. This is expected due to the partial volume effect arising from the finite spatial resolution of the imaging system and the fact that the imaged structures do not perfectly align with the voxel grid used in the reconstruction [131]. For better comparison between both error maps (left: original binning, right: improved binning), two ROIs containing material transitions were highlighted and zoomed in. In both ROIs, the average absolute error was calculated following equation (5.5.7). In $\mathrm{ROI}_A$, the reconstruction using the original binning method yielded an error of 0.099, while the improved approach with cylindrical hull and additional channel weighting resulted in a value of 0.067. In $\mathrm{ROI}_B$, the average RSP errors were determined to be 0.146 and 0.120, respectively.

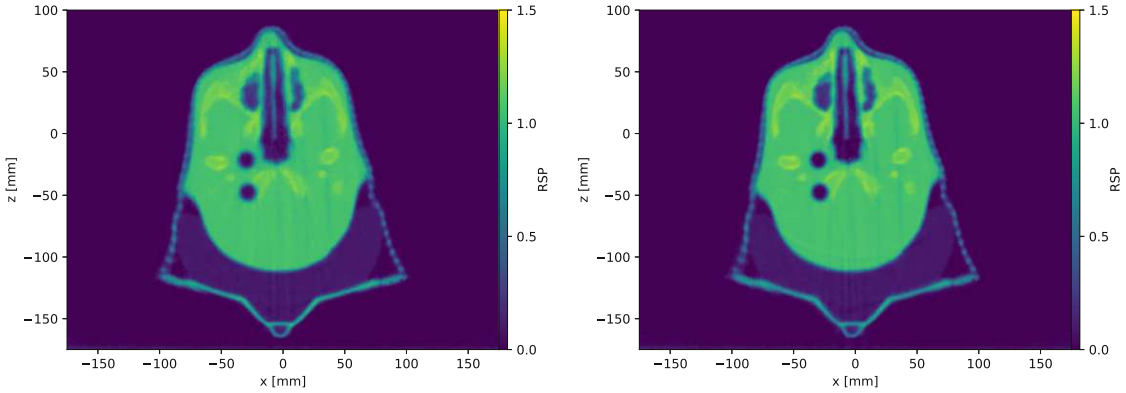


Figure 5.5.11: Reconstructed slice of the CIRS phantom (using 50 protons/mm$^2$). Left: using the original pre-reconstruction binning method [132], right: using the improved pre-reconstruction binning (with an object-surrounding cylindrical hull and channel weighting). The figure was taken from Kaser et al. [126].

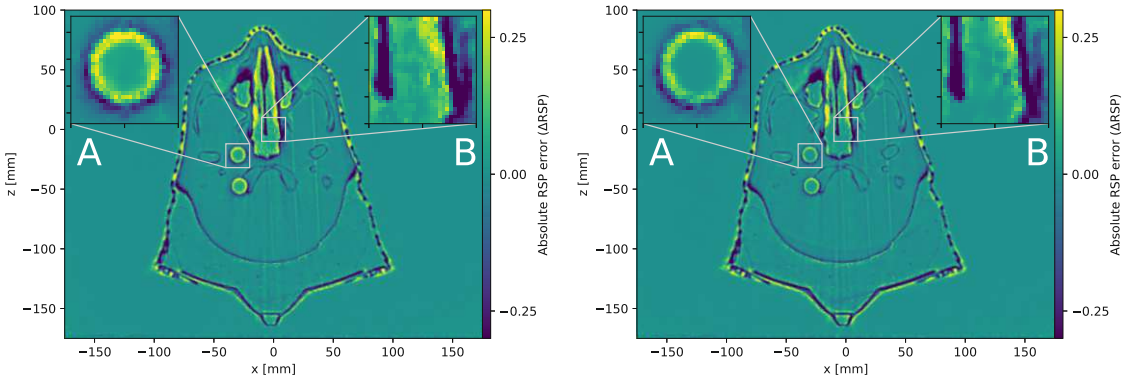


Figure 5.5.12: Absolute RSP error for the reconstruction of the CIRS phantom, as it was obtained by subtraction from a reference RSP map. Left: using the original pre-reconstruction binning method [132], right: using the improved pre-reconstruction binning (with an object-surrounding cylindrical hull and channel weighting). The figure was taken from Kaser et al. [126].

#### 5.5.6.2 Helium ions

Using helium ion beams, an ideal data set (see section 5.5.3) of the two CTP modules was reconstructed as a first test. Figure 5.5.13 shows the reconstructed central slices of the CTP528 using the original approach for the pre-reconstruction binning [132] (without object-surrounding cylindrical hull) and the improved approach (with a hull). For a more detailed view, the 5 lp/cm insert was enlarged. Visually, already some differences in the image contrast can be observed between both reconstructions.

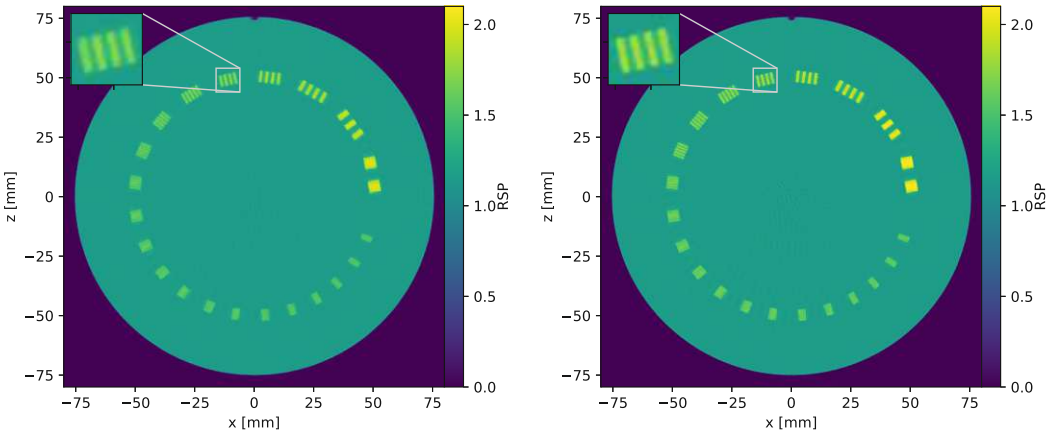


Figure 5.5.13: Central slices of the reconstructed CTP528 (using helium ions). A reconstruction using the original binning approach [132] (left) and the improved approach (right) are shown.

Before calculating the approximate MTF (see equation (5.4.3)), the actual RSP profiles through the line pair inserts of the CTP528 were plotted to highlight the difference in the reconstruction approach using the binning based on the original iRad method (without hull) or the improved approach (with object-surrounding cylindrical hull ad additional channel weighting). It can be observed in all cases that for the improved approach, the RSP profile rises to a value closer to the reference value of aluminium than the profiles obtained for the reconstruction based on the original binning approach.

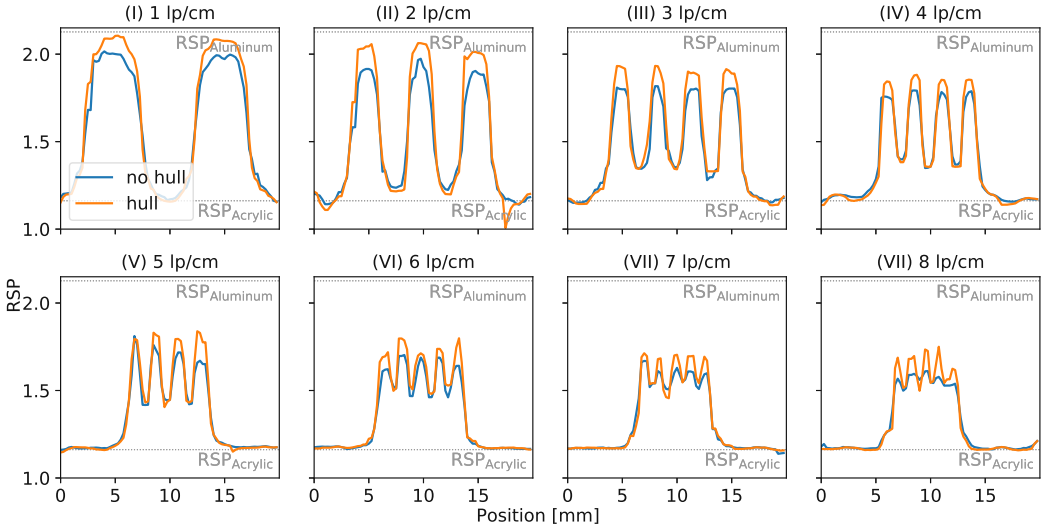


Figure 5.5.14: Line profiles through the first eight line pair inserts of the CTP528 using helium ions for imaging. The blue lines represent the reconstruction result using the original binning approach (without hull) [56], while the orange lines represent the reconstruction results with an object-surrounding hull and improved channel weighting.

The effect can then be verified by again approximating the MTF for the first eight line pair inserts, which is seen in figure 5.5.15. While for the binning approach without a hull (original approach), the subsequent reconstruction yielded an approximate MTF value of 4.7 % for the 8 lp/cm insert, the reconstruction based on the improved binning yielded an approximate MTF value of 17.3 %. For the 7 lp/cm insert, the original approach resulted in a value of ≈10.9 %, which lies above the threshold ($MTF_{10\%}$). However, the improved approach again outperformed this result and yielded an approximate MTF of ≈18 % for this insert.

The results obtained with helium ion beams yielded higher MTF values than obtained with protons (see figure 5.5.8). For the 7 lp/cm insert, an MTF value of ≈7.8% and ≈16.7% were obtained using the original and the improved binning approach, respectively. This effect was expected, as helium ions are expected to suffer less from multiple Coulomb scattering (MCS) than protons due to their higher mass-to-charge ratio.

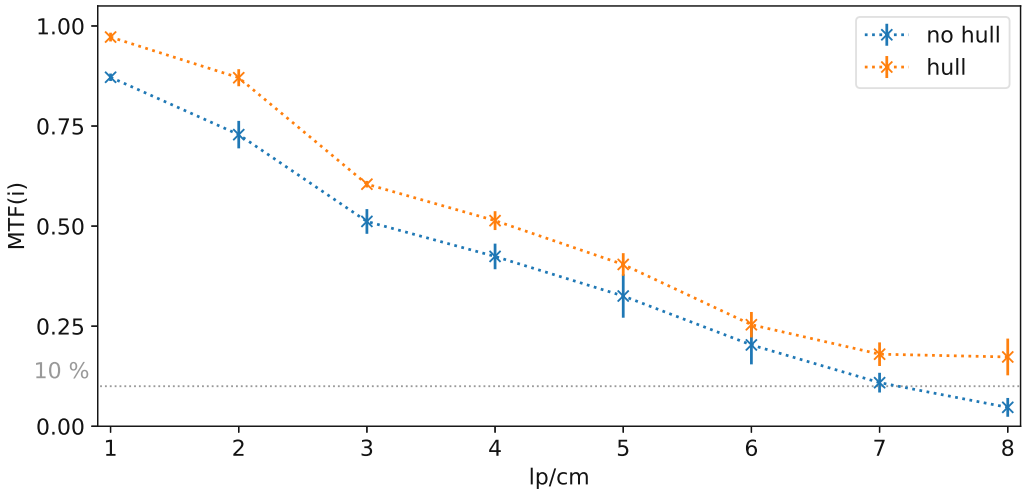


Figure 5.5.15: Approximated MTF for the CTP528 inserts using helium ions for imaging. The resulting line pair contrast (approximate MTF) for each insert $i$ is displayed in blue for the original binning approach [56] and in orange for the improved approach (with object-surrounding cylindrical hull and additional channel weighting). The dotted gray line represents the $MTF_{10\%}$.

The reconstructed central slices of the CTP404 (sensitometry module) can be seen in figure 5.5.16. On the left side of the image, the reconstruction using the original approach for the pre-reconstruction binning (without hull) is shown, while on the right side, the reconstruction using the improved approach (with object-surrounding cylindrical hull and additional channel weighting) is displayed. Although, visually, both reconstructions appear similarly, some differences can be observed when regarding the material inserts in the phantom body. While all inserts can be distinguished from the actual phantom body, the transitions appear slightly more blurry for the reconstruction following the original approach than for the reconstruction with the improved approach. This finding goes well along with the line pair contrast that was analysed with the CTP528 module, where the improved approach was shown to outperform the original approach.

Table 5.8 contains the relative RSP errors (see equation (5.5.3)) for each phantom insert and the resulting MAPE (see equation (5.5.4)). For the result using the original approach for the pre-reconstruction binning, a MAPE of 0.30 % was obtained, which is similar to the value found for an ideal data set using proton beams (see table 5.6). Here, a MAPE of 0.39 % was obtained. Using the improved approach (with object-surrounding cylindrical hull and additional channel weighting) for the pre-reconstruction binning, the MAPE is recorded to be lower than for the original approach. For helium ions, a value of 0.21 % was determined, while the value obtained with proton beams was even a little lower (0.14 %, see table 5.6). For helium ions, all relative RSP errors were found to be below 1 %. The largest error was found for the reconstruction using the original binning approach and the Teflon® insert, where an error of 0.75 % was recorded. For the reconstruction using the improved binning approach (with object-surrounding cylindrical hull and additional channel weighting), the relative RSP error for this insert was found to be 0.47 %.

In table 5.9, the SNR, as calculated with equation (5.5.5), is listed for each insert and the average SNR for all inserts is given per reconstruction. As compared to reconstructions using

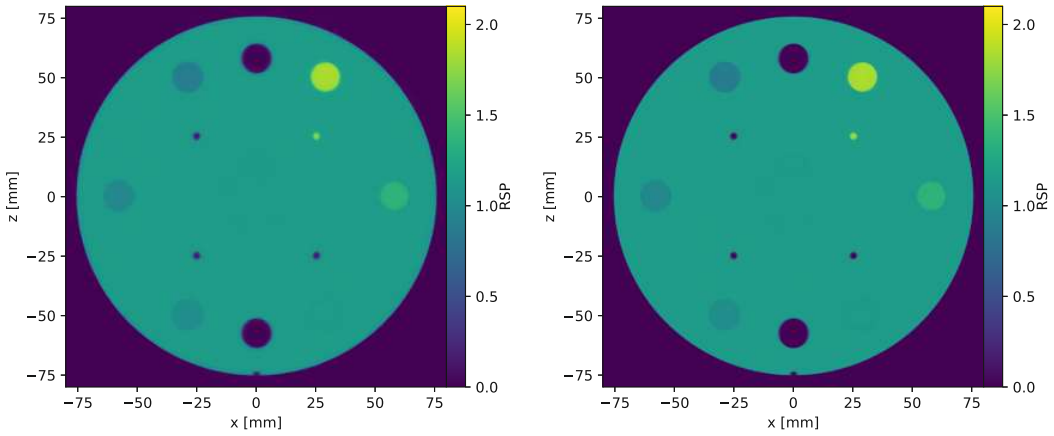


Figure 5.5.16: Central slices of the reconstructed CTP404 (using helium ions). A reconstruction using the original approach [132] (left) and the improved approach (right) are shown.

proton beams (see table 5.7), higher SNRs were recorded. This effect is again correlated to the fact that helium ions beams are affected less from MCS than proton beams and hence follow a more straight path through the object. This is not only reflected by increased spatial resolution (see analysis of the CTP528), but also in a higher SNR. For the reconstructions using helium ion beams, the reconstruction using the improved binning yielded a higher average SNR than the reconstruction using the original binning method (without object-surrounding cylindrical hull).

Table 5.8: Relative RSP errors $\epsilon$ in the CTP404 inserts. Reconstruction results obtained with the *original* (orig.) approach followed the method for ion radiography described by Collins-Fekete et al. [132] (without hull) for the pre-reconstruction binning. The *improved* (imp.) method refers to the reconstruction results using an object-surrounding cylindrical hull and channel weighting in the binning process. An ideal data set was used for the reconstruction, which is marked with the subscript $i$.

| **Method** | **Acrylic** | **PMP** | **LDPE** | **Teflon®** | **Delrin®** | **Polystyrene** | **MAPE** |
|---|---|---|---|---|---|---|---|
| $\epsilon_{\text{orig.},i}$ | 0.03% | 0.53% | 0.33% | -0.75% | -0.02% | 0.17% | 0.30% |
| $\epsilon_{\text{imp.},i}$ | 0.06% | 0.24% | 0.27% | -0.47% | 0.08% | 0.14% | 0.21% |

Table 5.9: SNR in the CTP404 inserts. Reconstruction results obtained with the *original* (orig.) approach followed the method for ion radiography described by Collins-Fekete et al. [132] (without hull) for the pre-reconstruction binning. The *improved* (imp.) method refers to the reconstruction results using an object-surrounding cylindrical hull and channel weighting in the binning process. An ideal data set was used for the reconstruction, which is marked with the subscript $i$.

| **Method** | **Acrylic** | **PMP** | **LDPE** | **Teflon®** | **Delrin®** | **Polystyrene** | **Avg. SNR** |
|---|---|---|---|---|---|---|---|
| $\text{SNR}_{\text{orig.},i}$ | 407.0 | 224.6 | 306.2 | 301.5 | 512.5 | 560.0 | 385.3 |
| $\text{SNR}_{\text{imp.},i}$ | 489.5 | 370.0 | 227.2 | 403.0 | 439.6 | 528.0 | 409.7 |

## 5.6 Discussion

In the first part of this chapter, a preliminary ion computed tomography (iCT) image reconstruction workflow with the tomographic iterative GPU-based reconstruction (TIGRE) toolbox [68], which was originally developed for cone-beam CT (CBCT), was introduced. To use the framework without code modification, a straight line (SL) ion path was assumed. Instead of using the beam's intensity loss (as in x-ray computed tomography (CT)), the ions' energy loss was used to define the projection value. In a very first application of the framework, the Bragg-Kleeman law (see equation (2.1.15)) was exploited so that the reconstruction procedure returned the material parameter $\alpha$, which could then again be used to calculate the relative stopping power (RSP). Position cuts were introduced to remove strongly scattered ions from the data set (see section 5.2.3) to improve spatial resolution and RSP accuracy of the reconstructed image that were generated with the ordered subsets SART (OS-SART) algorithm from Monte Carlo simulated data that modelled the demonstrator setup installed at MedAustron (see section 5.2.4).

As the reconstructions with Monte Carlo data showed promising results, the reconstruction workflow was applied to the real proton computed tomography (pCT) data measured with the iCT demonstrator, and the phantom described in section 4.2.1. In total, 80 projections were acquired and reconstructed to a 3D image, see section 4.3. Relative errors of the average RSP were found to be up to 14.9 % for an aluminium phantom thickness of 2 mm. For increasing phantom thickness (up to 10 mm), the relative error was found to decrease. Position cuts were shown to improve the reconstruction result. For example, the 10 mm stair yielded a relative RSP error of -3.4%, when only standard $3\sigma$ cuts were applied to the reconstruction data. Using an additional position cut of 1 mm resulted in a relative RSP error of -0.7% for that stair.

Finally, the reconstruction workflow with TIGRE was investigated for larger phantoms, see section 5.4. Two Catphan® (CTP) modules were studied as objects-to-be-imaged using Monte Carlo simulations to model an ion imaging setup. Proton beams with an initial energy of 200 MeV were used for the imaging. Due to the thickness of the phantoms, the position cut removed a major fraction of the initial particles (up to 90 percent at the phantom centre). However, with a 2 mm position cut, the first three line pair inserts of the CTP528 (high resolution module) showed an approximate modulation transfer function (MTF) value (corresponding to the line pair contrast) above 10 % using an initial particle fluence of 800 p/mm$^2$. By analysing the RSP distribution in the inserts of the CTP404 (sensitometry module), the position cut was shown to improve RSP accuracy as the deviation from reference values decreased with a stricter cut option. For comparison, the reconstruction workflow was also applied to imaging with helium ions (see section 5.4.5.2). Improved MTF values and RSP accuracy were found in contrast to reconstructions using protons, and fewer particles were rejected by the position cut.

While the initially used particle fluence (800 p/mm$^2$) was in the typical order for iCT (e.g., 900 p/mm$^2$ [65] or 100 p/mm$^2$ Giacometti et al. [127]), an investigation with increased statistics (8000 p/mm$^2$) exceeded these values by far, but could further improve the reconstruction result with proton beams. Overall, position cuts introduce a lower limit for the particle fluence, as further decreasing of the given number would result in holes in the projections. From a clinical perspective, removing a high percentage of the measured data would result in additional dose to the patient. Even if the imaging is performed for material science experiments, the higher dose needed for imaging could still increase measurement time.

As discussed in section 3.4, there exist multiple codes for iCT image reconstruction, which already incorporate a curved ion path estimate in the reconstruction process. However, TIGRE still gave multiple incentives to further investigate the toolbox for ion imaging, as they were identified in Kaser et al. [123]:

- A wide range of algorithms from different families is already implemented in the toolbox.

- TIGRE allows for modular code adaption and extensions. For example, the projection and back projection operators could be modified in the compute unified device architecture (CUDA) language, while a MATLAB header can be kept for the user.
- The previous point allows for a user-friendly toolbox for the (multidisciplinary) imaging community.
- The toolbox is available open-source.
- TIGRE already allows for the use of multi-GPUs for image reconstruction, which further speeds up the reconstruction process.
- For noisy input data or a small amount of projections, TIGRE has already shown promising reconstruction results, as demonstrated for x-ray imaging in [68, 139].

For this reason, a code extension for ion imaging was developed for the toolbox. The implemented methodology (see section 5.5.1) followed the existing binning approach for high resolution ion radiography, as described in Collins-Fekete et al. [132]. This approach allows using the already implemented reconstruction algorithms in TIGRE without further adaption, as the high resolution ion radiographs (iRads) already contain the ion path estimate (optimized cubic spline [56]). Furthermore, a second and slightly refined implementation of the method, which used a cylindrical object-surrounding hull and an additional channel weighting, was developed. Both implementations were published as part of the TIGRE toolbox[4] [126].

An ideal and a non-ideal pCT data set (180 projections) were created with Monte Carlo simulations. As phantoms, the CTP modules high resolution (CTP528) and sensitometry (CTP404) were used (as for the preliminary reconstruction workflow based on position cuts). The particle fluence was set to 225 protons/mm$^2$. Furthermore, an anthropomorphic phantom was implemented as phantom in the simulations. For this phantom, the particle fluence was further reduced to 50 protons/mm$^2$ and only 90 projections were created as reconstruction input.

Compared to the initial reconstruction workflow based on position cuts, the new implementation showed increased spatial resolution for the CTP528. For the reconstruction using an ideal data set, up to 8 lp/cm could be resolved using the improved binning with cylindrical hull and additional channel weighting. Furthermore, the mean absolute percentage error (MAPE) of the reconstructions was found to be below 1% for the inserts of the CTP404. Even though the implemented hull did not represent the accurate convex hull [133, 134] of the anthropomorphic phantom, the reconstruction using the improved approach still yielded an improved result as compared to the original approach (without hull). This could be validated by analysing the average absolute RSP in two regions of interest (ROIs).

To test the code extension for helium ion beams, an ideal data set was created in Monte Carlo simulations for each of the two CTP modules. The data were converted to a 3D RSP map using the new code extension for binning in TIGRE and the already implemented adaptive-steepest-descent-projection onto convex sets (ASD-POCS) for reconstruction. The results, that were presented in section 5.5.6.2, showed that the spatial resolution increased (corresponding to higher MTF values) as compared to the reconstructions using proton beams. The MAPE was found to be similar to the reconstructions using proton beams (in all cases, it was below 0.5 %). However, a higher signal-to-noise ratio (SNR) was observed for helium ions. As helium ions are less affected by multiple Coulomb scattering (MCS) than protons, this effect was expected. Again, using the improved binning with cylindrical hull and additional channel weighting could improve the reconstruction result as compared to using the original binning approach [132]. This can be seen, for example, in figure 5.5.14, where the improved approach was shown to yield more accurate RSP line profiles than reconstructions using the original binning approach to generate input data.

[4] https://github.com/CERN/TIGRE

# CHAPTER 6

# Summary and outlook

## 6.1 Summary

In the scope of this thesis, image processing and reconstruction techniques for ion computed tomography (iCT) were investigated and developed to allow obtaining 2D and 3D images from data measured with an iCT demonstrator system installed at MedAustron. The demonstrator consisted of four 5.12 cm × 2.56 cm double-sided silicon strip detectors (DSSDs) for particle tracking and a scintillator-based range telescope for the residual energy measurement. To understand the physical concepts, the basic principles as well as the advantages and drawbacks of imaging with ions, these aspects were discussed in chapter 2, while software tools were introduced in chapter 3.

Radiographic ion imaging techniques were investigated with the demonstrator and were discussed in chapter 4, where imaging results from three different imaging modalities were shown. Energy-loss radiography is based on the data obtained with the tracking system and the calorimeter of the imaging system, and corresponds to the basis for iCT applications which aim at improving ion therapy treatment planning. Other imaging modalities only rely on the tracker measurement. In that scope, ion scattering radiography and beam attenuation imaging were investigated. The data obtained from the demonstrator were compared to Monte Carlo data and theoretical calculations and showed good agreement with increasing error for smaller phantom thicknesses. Although scattering ion imaging and beam attenuation imaging will likely not be used as a stand-alone modality in the clinic, they might be used in material science, or as a complementary imaging technique along with energy-loss radiography or iCT (as the images could be created from the same data set).

In chapter 5, a reconstruction workflow for iCT was developed in order to obtain a relative stopping power (RSP) map from the projection data obtained with the iCT demonstrator. The open-source tomographic iterative GPU-based reconstruction (TIGRE) toolbox [68] was chosen for reconstruction. Although the toolbox was originally developed for x-ray computed tomography (CT), a straight-line approximation of the ion paths allowed to use the framework for iCT. First tests were done with data obtained from Monte Carlo simulations. In the simulation, the iCT demonstrator system at MedAustron was modelled under ideal and realistic conditions. A cut option was introduced in order to remove strongly scattered ions from the data set. As the first reconstructions from simulated data showed promising results, the reconstruction workflow was used to reconstruct an RSP map from 80 energy-loss radiographs of an aluminium stair profile measured with the iCT demonstrator at MedAustron.

As the demonstrator only allowed to image small objects (due to the size of the tracker planes), Monte Carlo simulations were further used to generate imaging data of larger phan-

toms. The Catphan® (CTP) module CTP528 (high resolution) was implemented in the simulations to investigate the spatial resolution of the reconstructed images by calculating the line pair contrast of its aluminium inserts with decreasing size. The CTP404 (sensitometry module) incorporates multiple inserts made from different materials and was used to analyse the RSP accuracy of the reconstructed images. The results showed the limits of the iCT reconstruction approach with the TIGRE toolbox that was based on a straight-line approach for the ion path. Although, for protons, up to 3 lp/cm could be resolved with a particle fluence of 800 protons/mm$^2$, the implemented data cuts removed the major fraction of particles passing the phantom centre (approx. 90%). For helium ions, the effect was less pronounced, however, data cuts still removed approx. 70% of the ions in the phantom centre.

For an improved iCT reconstruction with TIGRE, a code extension based on the compute unified device architecture (CUDA) language (using C++) for a pre-reconstruction binning was added to the framework. The method, which incorporates curved ion path estimates, followed an existing approach for ion radiography (iRad) [132] and was slightly refined within this work. This allowed to increase the spatial resolution for proton computed tomography (pCT) to 8 lp/cm under ideal conditions, while the particle fluence was decreased to 225 protons/mm$^2$. The RSP mean absolute percentage error (MAPE) of the reconstructions was found to be below 1% in the sensitometry inserts.

Overall, the research performed in the scope of this work allowed for the very first iCT image reconstruction from the data measured with the iCT demonstrator system installed at MedAustron. The reconstruction workflow was further refined and the code was made available to other research groups by making it part of the open-source TIGRE toolbox. In the scope of this work, the iCT demonstrator system at MedAustron was further used to investigate various ion imaging modalities (energy-loss iCT, scattering and beam attenuation radiography). The results of these measurements can be seen as a complement to existing studies, which are often based on Monte Carlo data only. The main findings of this thesis were published in

- S. Kaser et al. "First application of the GPU-based software framework TIGRE for proton CT image reconstruction". In: Physica Medica 84 (2021), pp. 56–64. doi: 10.1016/j.ejmp.2021.03.006 [123].
- S. Kaser et al. "Calculating $1/\beta^2 p^2$ for most likely path estimates for protons and helium ions using an analytical model". In: Physica Medica 89 (2021), pp. 169–175. doi: 10.1016/j.ejmp.2021.08.002 [58].
- S. Kaser et al. "Different radiographic imaging modalities with a proton computed tomography demonstrator". In: Journal of Instrumentation 17.01 (2022), p. C01010. doi: 10.1088/1748-0221/17/01/C01010 [83].
- S. Kaser et al. "Measurements of proton beam attenuation radiographs at a clinical facility". In: Nuclear Instruments and Methods in Physics Research Section A: Accelerators, Spectrometers, Detectors and Associated Equipment 1040 (2022), p. 167069. doi: 10.1016/j.nima.2022.167069 [85].
- S. Kaser et al. "Extension of the open-source TIGRE toolbox for proton imaging". In: Zeitschrift für Medizinische Physik (2022). doi: 10.1016/j.zemedi.2022.08.005 [126].

## 6.2 Outlook

The newly added code extension, which was published as part of the open-source TIGRE toolbox, can be seen as a first step towards the modification of the framework for iCT applications. While the pre-reconstruction binning allows using the already implemented x-ray CT reconstruction algorithms without adaption, further developments could focus on

incorporating the ion path estimates directly in the forward and back projection operators, hence in the reconstruction algorithms themselves. Furthermore, to reach the long-term goal of clinical implementation of iCT, future research will need to focus, among other aspects, on testing reconstruction techniques with experimental data. Updating the iCT demonstrator in terms of technology (improving, for example, the read-out rate) and size will hence become crucial. Currently, a system based on time-of-flight measurements is being investigated [138].

# APPENDIX A

## Additional formulas and analysis results

### A.1 Definition of the scattering matrix elements

According to Schulte et al. [53], the elements of the scattering matrices used in equation (2.4.4) for the calculation of the most likely path (MLP) of an ion are defined as

$$\sigma^2_{t_i}(w_{i-1}, w_i) = E_0^2 \left(1 + 0.038 \ln \frac{w_i - w_{i-1}}{X_0}\right)^2 \times \int_{w_{i-1}}^{w_i} \frac{(w_i - w)^2}{\beta^2(w) p^2(w)} \frac{1}{X_0} \mathrm{d}w, \tag{A.1.1}$$

$$\sigma^2_{\theta_i}(w_{i-1}, w_i) = E_0^2 \left(1 + 0.038 \ln \frac{w_i - w_{i-1}}{X_0}\right)^2 \times \int_{w_{i-1}}^{w_i} \frac{1}{\beta^2(w) p^2(w)} \frac{1}{X_0} \mathrm{d}w, \tag{A.1.2}$$

$$\sigma^2_{t_i\theta_i}(w_{i-1}, w_i) = E_0^2 \left(1 + 0.038 \ln \frac{w_i - w_{i-1}}{X_0}\right)^2 \times \int_{w_{i-1}}^{w_i} \frac{w_i - w}{\beta^2(w) p^2(w)} \frac{1}{X_0} \mathrm{d}w, \tag{A.1.3}$$

with $i = 1, 2$ and the empirical constants $E_0 = 13.6 MeV/c$ and 0.038 that were introduced by Lynch and Dahl [20]. $X_0$ corresponds to the radiation length of the investigated material, which is often assumed to be water ($X_0 = 36.1\,\mathrm{cm}$) [53].

### A.2 Analytical evaluation of $\int_{w_0}^{w_1} \frac{w^n}{\beta(w)^2 p(w)^2} dw$

According to Kaser et al. [58], the value of equation (2.4.5) can be calculated by the following analytical approximations (option B in section 2.4.1)

$$\begin{aligned} \int_{w_0}^{w_1} \frac{1}{\beta(w)^2 p(w)^2} \mathrm{d}w \approx \\ \left[ \frac{7\alpha}{128} \left( \frac{64\alpha^{5/7} E_{\mathrm{rest}}}{2\alpha^{4/7} E_{\mathrm{rest}} \tilde{w} + \tilde{w}^5} + \frac{40\alpha^{1/7} \tilde{w}^3}{2\alpha^{4/7} E_{\mathrm{rest}} + \tilde{w}^4} \right. \right. \\ \left. \left. + \left(\frac{2}{E_{\mathrm{rest}}}\right)^{1/4} \left[ 22 \left(\arctan_- - \arctan_+\right) - 11 \left(\ln_- - \ln_+\right) \right] \right) \right]_{w_0}^{w_1} \end{aligned} \tag{A.2.1}$$

$$\int_{w_0}^{w_1} \frac{w}{\beta(w)^2 p(w)^2} \mathrm{d}w \approx$$
$$\left[\frac{7\alpha}{384}\left(\frac{96\alpha^{1/7}R_0}{\tilde{w}} - 384\alpha^{5/7}E_{\mathrm{rest}}\tilde{w}^2 + \frac{24\alpha^{1/7}\left(-4\alpha^{8/7}E_{\mathrm{rest}}^2 + R_0\tilde{w}\right)\tilde{w}^2}{2\alpha^{4/7}E_{\mathrm{rest}} + \tilde{w}^4}\right.\right.$$
$$+64\alpha^{1/7}\tilde{w}^6 + 432\sqrt{2}\alpha E_{\mathrm{rest}}^{3/2}\arctan\left[\frac{\tilde{w}^2}{\sqrt{2}\alpha^{2/7}\sqrt{E_{\mathrm{rest}}}}\right] \tag{A.2.2}$$
$$\left.\left.+\left(\frac{2}{E_{\mathrm{rest}}}\right)^{1/4}\left[66\ R_0(\arctan_- - \arctan_+) - 33\ R_0(\ln_- - \ln_+)\right]\right)\right]_{w_0}^{w_1}$$

$$\int_{w_0}^{w_1} \frac{w^2}{\beta(w)^2 p(w)^2} \mathrm{d}w \approx$$
$$\left[\frac{7\alpha^{8/7}R_0^2}{4\tilde{w}} + 84\alpha^{20/7}E_{\mathrm{rest}}^3\tilde{w} + \frac{7\alpha^{8/7}\left(-4\alpha^{8/7}E_{\mathrm{rest}}^2 + R_0\tilde{w}\right)^2\tilde{w}}{16\left(2\alpha^{4/7}E_{\mathrm{rest}} + \tilde{w}^4\right)}\right.$$
$$-14\alpha^{12/7}E_{\mathrm{rest}}R_0\tilde{w}^2 - 7\alpha^{16/7}E_{\mathrm{rest}}^2\tilde{w}^5 + \frac{7}{3}\alpha^{8/7}R_0\tilde{w}^6 \tag{A.2.3}$$
$$+\frac{14}{9}\alpha^{12/7}E_{\mathrm{rest}}\tilde{w}^9 - \frac{7}{13}\alpha^{8/7}\tilde{w}^{13} + \frac{63\alpha^2E_{\mathrm{rest}}^{3/2}R_0\arctan\left[\frac{\tilde{w}^2}{\sqrt{2}\alpha^{2/7}\sqrt{E_{\mathrm{rest}}}}\right]}{2\sqrt{2}}$$
$$\left.+2\xi_+(\arctan_- - \arctan_+) + \xi_-(\ln_- - \ln_+)\right]_{w_0}^{w_1}$$

with $\alpha = 0.00241$ and $p = 1.75$. For better readability, the following functions were used,

$$\tilde{w} = (R_0 - w)^{1/7}, \tag{A.2.4}$$

$$\ln_\pm = \ln\left[\sqrt{2}\alpha^{2/7}\sqrt{E_{\mathrm{rest}}} \pm 2^{3/4}\alpha^{1/7}E_{\mathrm{rest}}^{1/4}\tilde{w} + \tilde{w}^2\right], \tag{A.2.5}$$

$$\arctan_\pm = \arctan\left[1 \pm \frac{2^{1/4}\tilde{w}}{\alpha^{1/7}E_{\mathrm{rest}}^{1/4}}\right], \tag{A.2.6}$$

$$\xi_\pm = \frac{7\alpha\left(200\sqrt{2}\alpha^2E_{\mathrm{rest}}^{7/2} \pm 11R_0^2\right)}{64\ 2^{3/4}E_{\mathrm{rest}}^{1/4}}. \tag{A.2.7}$$

## A.3 Analysis details of the stair profile simulation

In section 5.2.4, reconstruction results from two Geant4 simulations modelling the iCT demonstrator under idealized and realistic conditions were shown. The following plots show the influence of a position cut on the reconstruction result in more detail. Pixels in the central slice of the reconstruction were sorted into categories depending on the relation between reconstructed RSP and the expected reference value RSP (approximately 2.08, as obtained with an R80 measurement). Four thresholds were selected, which leads to five Voxel categories:

- Voxel value above 90 % $\mathrm{RSP_{ref}}$
- Voxel value above 70 % $\mathrm{RSP_{ref}}$
- Voxel value above 50 % $\mathrm{RSP_{ref}}$

- Voxel value above 30 % $\mathrm{RSP_{ref}}$
- Voxel value below 30 % $\mathrm{RSP_{ref}}$

These categories show if the RSP of a voxel within the phantom area is underestimated or the RSP is overestimated in voxels outside the phantom area. To distinguish whether a voxel lies inside or outside the phantom area, the actual phantom location and shape is marked with a dotted white line in the plots.

### A.3.1 Ideal data set

In figure A.3.1, the reconstruction results using the ideal data set, and 180 projections are displayed. Regarding the area outside the phantom, a clear improvement of the 1 mm position cut can be observed: without any position cut, the majority of voxels adjoining the phantom area exceed a value of 30 % $\mathrm{RSP_{ref}}$ and could mistakenly be interpreted as part of the phantom. With the position cut, the RSP of the adjoining voxels lies below 30 % $\mathrm{RSP_{ref}}$ in almost all cases. Within the phantom area, the RSP in the edge voxels is mostly underestimated (below 90 % $\mathrm{RSP_{ref}}$). This effect is similar for the reconstruction with and without position cut. In the phantom center, the reconstructed RSP lies above 90 % $\mathrm{RSP_{ref}}$.

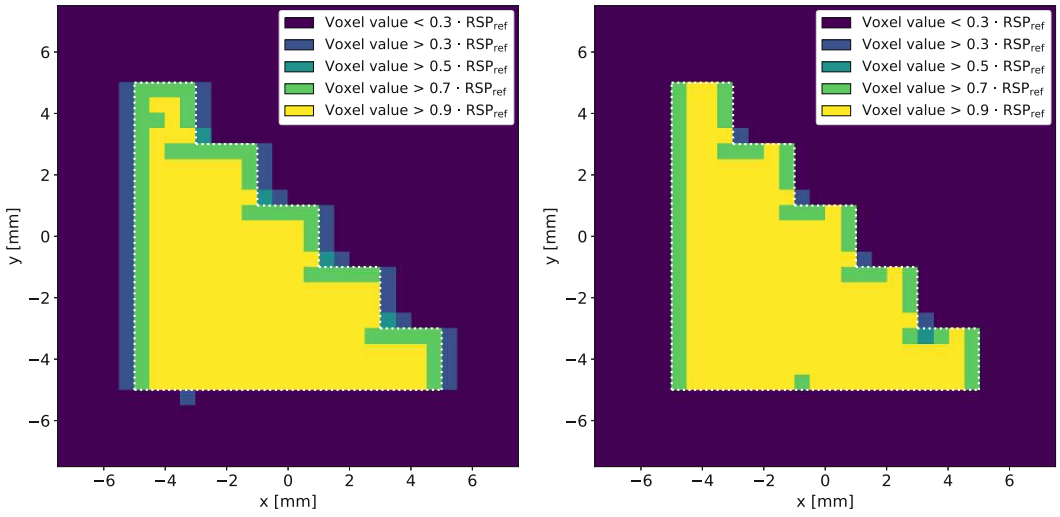


Figure A.3.1: Reconstructions of the ideal data set (180 projections). Pixels were sorted into categories depending on the relation between measured RSP and the expected reference value $\mathrm{RSP_{ref}}$. A white dotted line marks the actual phantom location, which is known from the simulation parameters. Left: no position cut used. Right: 1 mm position cut used.

Similar effects can be seen for the reconstructions using only 90 projections as input data (see figure A.3.2).

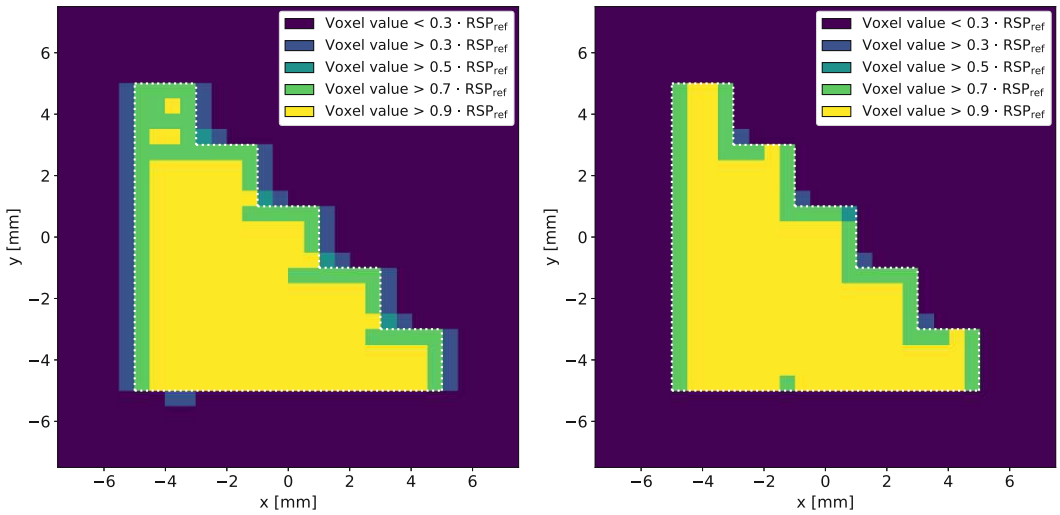


Figure A.3.2: Reconstructions of the ideal data set (90 projections). Pixels were sorted into categories depending on the relation between measured RSP and the expected reference value $\mathrm{RSP}_{\mathrm{ref}}$. A white dotted line marks the actual phantom location, which is known from the simulation parameters. Left: no position cut used. Right: 1 mm position cut used.

### A.3.2 Realistic data set

In the reconstructions from the realistic data set, the rotary table is visible in form of increased RSPs in the area below the actual phantom. In figure A.3.3, the reconstructions from 180 projections (without and with the use of a 1 mm position cut) are displayed, while figure A.3.4 shows the reconstruction results from 90 projections. In both cases, the effect of the 1 mm position cut is apparent: while in the reconstruction without position cut, the voxels surrounding the phantom area shows an increased RSP (and could therefore mistakenly be interpreted as part of the phantom), this effect is decreased for the reconstructions using a position cut. In the phantom center, an RSP above 90 % of the reference value was found in with only few exceptions. However, edge voxels showed a lower RSP than expected (for reconstructions with and without position cut). Only minor differences between the reconstructions from 90 and 180 projections can be detected.

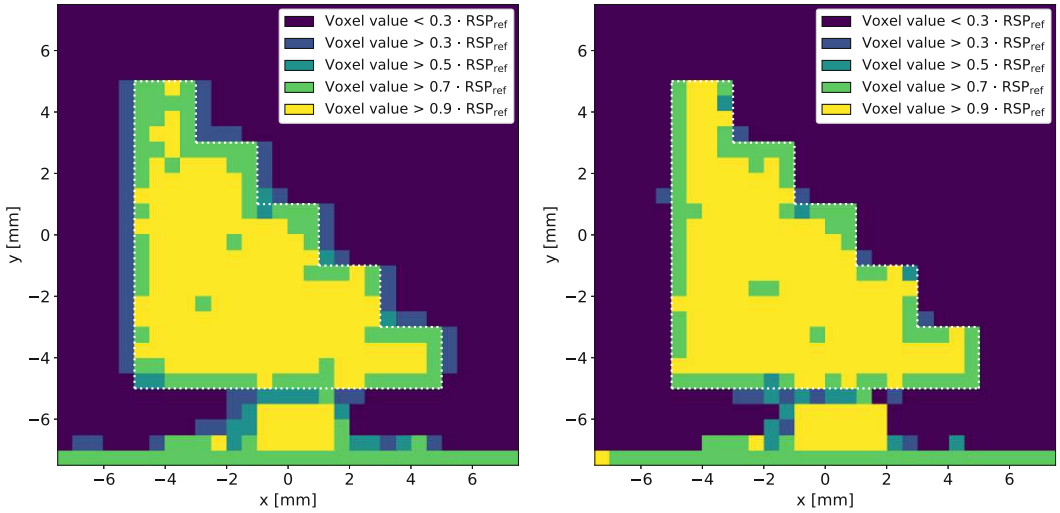


Figure A.3.3: Reconstructions of the realistic data set (180 projections). Pixels were sorted into categories depending on the relation between measured RSP and the expected reference value $\mathrm{RSP}_{\mathrm{ref}}$. A white dotted line marks the actual phantom location, which is known from the simulation parameters. Left: no position cut used. Right: 1 mm position cut used.

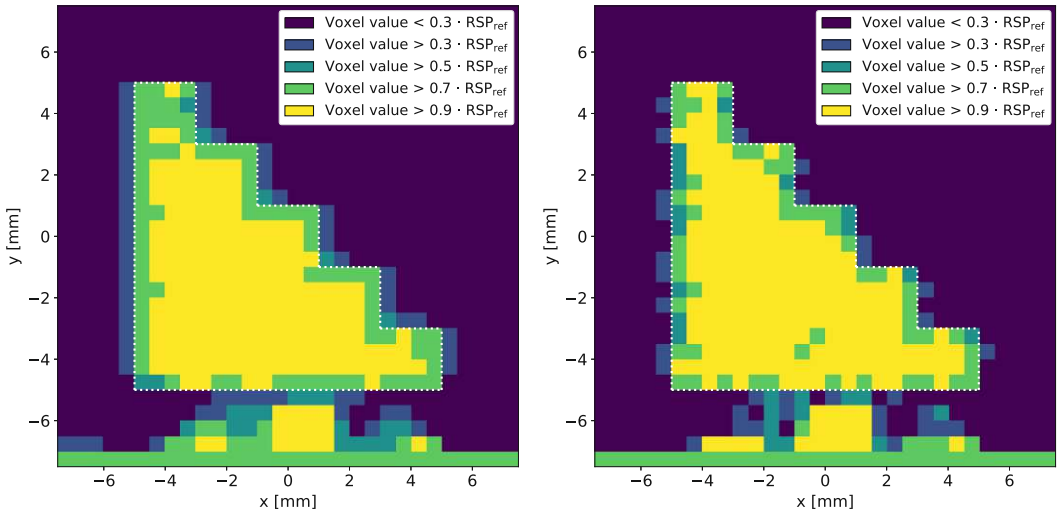


Figure A.3.4: Reconstructions of the realistic data set (90 projections). Pixels were sorted into categories depending on the relation between measured RSP and the expected reference value $\mathrm{RSP}_{\mathrm{ref}}$. A white dotted line marks the actual phantom location, which is known from the simulation parameters. Left: no position cut used. Right: 1 mm position cut used.

# APPENDIX B

## Example code for the TIGRE toolbox extension

The following code[1] demonstrates the process of invoking the binning process to obtain a high-resolution proton radiography (pRad) with the TIGRE toolbox. The geometry definition corresponds to the procedure described in Biguri et al. [68] but has an additional variable (`geo.DSID`), which corresponds to the location of the upstream detector used in pCT/pRad applications using single-particle tracking. After geometry and beam energy definition, the data is loaded. Finally, for invoking the binning procedure, the function `pCTCubicSpline_mex()` is called.

```
%--------------------------------------------------------------------------
%--------------------------------------------------------------------------
% This file is part of the TIGRE Toolbox
%
% Copyright (c) 2015, University of Bath and
%                     CERN-European Organization for Nuclear Research
%                     All rights reserved.
%
% License:            Open Source under BSD.
%                     See the full license at
%                     https://github.com/CERN/TIGRE/blob/master/LICENSE
%
% Contact:            tigre.toolbox@gmail.com
% Codes:              https://github.com/CERN/TIGRE/
% Coded by:           Stefanie Kaser
%--------------------------------------------------------------------------
%% pCT geometry definition

geo.dDetector = [0.25; 0.25]; % Pixel size of optimized pRad in mm.
geo.DSID = 245; % Distance between source and upstream detector.
geo.DSO = 300; % Distance between source and origin (center of rotation).
geo.DSD = 355; % Distance between source and downstream detector.
geo.hull = [0; 0; 0; 0]; % We won't use a convex hull here (all entries are
% set to 0).
geo.sDetector = [20; 20]; % Defines the size (in mm) of the optimized pRad.
geo.mode = 'parallel'; % or 'cone' in case of cone beam geometry
```

[1] Available at https://github.com/CERN/TIGRE/blob/master/MATLAB/Demos/pRad_demo.m

```
%% pCT initial beam energy
eIn = single(100);

%% Load pCT data set.
% The data set corresponds to one radiographic image (pRad) of an Aluminum
% stair profile as used in https://arxiv.org/abs/2106.12890. However, our
% test data set is based on Monte Carlo simulations (GATE:
% doi.org/10.1016/S0920-5632(03)90969-8). The data set contains the
% protons' upstream and downstream positions and directions as well as the
% single proton WEPLs (all in mm).
data = pCTdata();

%% Binning the data into an optimized pRad
% Finally, the single proton data are binned into an optimized pRad.
proj = pCTCubicSpline_mex(data.posIn, data.posOut, data.dirIn, ...
    data.dirOut, data.Wepl, eIn, geo);
% We are only creating one test pRad here. Creating pRads at multiple
% rotation angles would allow to use the collection as input for TIGRE's
% reconstruction algorithms (see d04_SimpleReconstruction.m).

%% Plot the result
imshow(proj, [0, 3], 'InitialMagnification', 500);
```

# Acronyms

**AAD** average absolute deviation. 38, 39

**API** application programming interface. 27, 31

**ART** algebraic reconstruction technique. 24

**ASD-POCS** adaptive-steepest-descent-projection onto convex sets. 24, 30, 62–68, 70, 84

**CBCT** cone-beam CT. 22, 30, 83

**CGLS** conjugate gradient least squares. 30

**CPU** central processing unit. 31

**CS** cubic spline. 20

**CT** computed tomography. 1, 14–17, 21–24, 29, 52, 69, 70, 72, 74, 78, 83, 85, 86, 101

**CTP** Catphan®. 58–70, 72–84, 86, 102, 103, 105

**CUDA** compute unified device architecture. 27, 30, 31, 71, 84, 86

**DAQ** data acquisition. 34, 35, 38, 47

**DRAM** device random-access memory. 31

**DSSD** double-sided silicon strip detector. 34, 41, 42, 46, 51, 52, 85

**FBP** filtered backprojection. 22, 25, 26, 30

**FDK** Feldkamp-Davis-Kress. 23, 30

**FWHM** full-width at half maximum. 39

**GATE** Geant4 application for tomographic emission. 8, 9, 29, 44, 46, 71–73

**GPGPU** general purpose computation on a graphics processing unit. 31

**GPU** graphics processing unit. 30, 31

**HEPHY** Institute of High Energy Physics. iii, 1, 33

**HPC** high performance computer. 30

**HU** Hounsfield unit. 1, 15, 16, 29, 72

**IAEA** International Atomic Energy Agency. 13

**iCT** ion computed tomography. 1–3, 16, 21–27, 29, 33–37, 40, 41, 46, 47, 49–51, 59, 60, 69, 71, 73, 74, 83, 85–87, 90, 101, 102, 105

**IR** irradiation room. 33, 36

**iRad** ion radiography. 1, 24, 36, 70, 80, 84, 86, 102, 103, 105

**LDPE** low density polyethylen. 59, 62, 64, 69, 77, 78, 82

**LET** linear (restricted) energy transfer. 13

**LHC** large hadron collider. 29

**LINAC** linear accelerator. 11

**lp** line pair. 59

**MAPE** mean absolute percentage error. 74, 77, 81, 82, 84, 86

**MCS** multiple Coulomb scattering. 5, 16, 24, 25, 34, 37, 41, 42, 46, 47, 81, 82, 84

**ML** maximum likelihood. 69

**MLP** most likely path. 17–20, 23, 25, 89, 101

**MPV** most probable value. 57, 58, 102

**MTF** modulation transfer function. 61–64, 68, 73, 75, 76, 80, 81, 83, 84, 102, 103, 105

**OS-SART** ordered subsets SART. 24, 30, 53, 56, 62–68, 83

**PC** personal computer. 30

**PCB** printed circuit board. 51

**PCI** peripheral component interconnect. 31

**pCT** proton computed tomography. 2, 72, 83, 84, 86, 95

**PET** positron emission tomography. 29, 66

**PMMA** polymethylmethacrylat. 35, 38, 39, 47, 101

**PMP** polymethylpentene. 59, 62, 64, 65, 69, 77, 78, 82

**POCS** projection onto convex sets. 24

**pRad** proton radiography. 36, 37, 40–45, 47, 52–56, 70, 71, 95, 101, 102, 105

**PRR30** proton range radiography system. 34, 35

**RBE** relative biological effectiveness. 12, 13

**RMSE** root mean square error. 19

**ROI** region of interest. 37, 39, 44, 45, 53–58, 62, 64–66, 73, 74, 78, 84, 105

**RSP** relative stopping power. 5, 15, 16, 23, 25, 37, 47, 49, 52–69, 71–74, 77–86, 90–93, 102, 105

**SART** simultaneous algebraic reconstruction technique. 23, 24, 30

**SIRT** simultaneous iterations reconstruction technique. 30

**SL** straight line. 2, 16, 17, 20–22, 37, 69, 83

**SNR** signal-to-noise ratio. 74, 77, 78, 81, 82, 84, 105

**SOBP** spread-out Bragg peak. 12

**SP** stopping power. 1, 4, 5, 7, 13, 14, 19, 21, 22, 44, 51, 52, 61

**SPECT** single-photon emission computed tomography. 29

**TIGRE** tomographic iterative GPU-based reconstruction. 2, 27, 30, 51–53, 62, 69–73, 83–86, 95, 101, 102

**TLU** trigger and logic unit. 35

**TU Wien** Technische Universität Wien. iii, 1, 33

**WEPL** water-equivalent path length. 14, 16, 20, 23, 61, 69, 70, 73, 102

**WET** water-equivalent thickness. 13, 14, 20, 34, 36, 37, 47, 49, 56, 69, 105

**WHO** World Health Organization. 8

# List of Figures

# List of Tables

# Bibliography



[1] Allan Macleod Cormack. "Representation of a function by its line integrals, with some radiological applications". In: *Journal of applied physics* 34.9 (1963), pp. 2722–2727. DOI: 10.1063/1.1729798.

[2] AM Koehler. "Proton radiography". In: *Science* 160.3825 (1968), pp. 303–304. DOI: 10.1126/science.160.3825.303.

[3] Wilhelm Conrad Röntgen. "Über eine neue Art von Strahlen". In: *Sitzungsber Phys Med Ges Wurtzburg* 9 (1895), pp. 132–141.

[4] Johann Heinrich Lambert. *Photometria sive de mensura et gradibus luminis, colorum et umbrae*. sumptibus vidvae E. Klett, typis CP Detleffsen, 1760.

[5] August Beer. "Bestimmung der absorption des rothen Lichts in farbigen Flüssigkeiten". In: *Ann. Physik* 162 (1852), pp. 78–88.

[6] Hans Bethe. "Zur Theorie des Durchgangs schneller Korpuskularstrahlen durch Materie". In: *Annalen der Physik* 397.3 (1930), pp. 325–400. DOI: 10.1002/andp.19303970303.

[7] Felix Bloch. "Zur Bremsung rasch bewegter Teilchen beim Durchgang durch Materie". In: *Annalen der Physik* 408.3 (1933), pp. 285–320.

[8] Wayne D Newhauser and Rui Zhang. "The physics of proton therapy". In: *Physics in Medicine & Biology* 60.8 (2015), R155. DOI: 10.1088/0031-9155/60/8/R155.

[9] Reinhard Schulte et al. "Conceptual design of a proton computed tomography system for applications in proton radiation therapy". In: *IEEE Transactions on Nuclear Science* 51.3 (2004), pp. 866–872. DOI: 10.1109/TNS.2004.829392.

[10] Uwe Schneider et al. "First proton radiography of an animal patient". In: *Medical Physics* 31.5 (2004), pp. 1046–1051. DOI: 10.1118/1.1690713.

[11] Uwe Schneider, Eros Pedroni, and Antony Lomax. "The calibration of CT Hounsfield units for radiotherapy treatment planning". In: *Physics in Medicine & Biology* 41.1 (1996), p. 111. DOI: 10.1088/0031-9155/41/1/009.

[12] S Meyer et al. "Dosimetric accuracy and radiobiological implications of ion computed tomography for proton therapy treatment planning". In: *Physics in Medicine & Biology* 64.12 (2019), p. 125008. DOI: 10.1088/1361-6560/ab0fdf.

[13] Lennart Volz et al. "The impact of secondary fragments on the image quality of helium ion imaging". In: *Physics in Medicine & Biology* 63.19 (2018), p. 195016. DOI: 10.1088/1361-6560/aadf25.

[14] Wolfgang Demtröder. *Experimentalphysik 4. Kern-, Teilchen- und Astrophysik*. Springer, 2010. Chap. 4.

[15] Helmut Paul. "The mean ionization potential of water, and its connection to the range of energetic carbon ions in water". In: *Nuclear Instruments and Methods in Physics Research Section B: Beam Interactions with Materials and Atoms* 255.2 (2007), pp. 435–437. DOI: 10.1016/j.nimb.2006.12.034.

[16] Tia Plautz et al. "200 MeV Proton Radiography Studies With a Hand Phantom Using a Prototype Proton CT Scanner". In: *IEEE Transactions on Medical Imaging* 33.4 (2014), pp. 875–881. DOI: 10.1109/TMI.2013.2297278.

[17] MJ Berger et al. "International Commission on Radiation Units and Measurements (Bethesda, Maryland) ICRU Report 49". In: *Journal of the International Commission on Radiation Units and Measurements* (1993). DOI: 10.1093/jicru/os25.2.report49.

[18] RM Sternheimer and RF Peierls. "General expression for the density effect for the ionization loss of charged particles". In: *Physical Review B* 3.11 (1971), p. 3681. DOI: 10.1103/PhysRevB.3.3681.

[19] N Arbor et al. "Monte Carlo comparison of x-ray and proton CT for range calculations of proton therapy beams". In: *Physics in Medicine & Biology* 60.19 (2015), p. 7585. DOI: 10.1088/0031-9155/60/19/7585.

[20] Gerald R Lynch and Orin I Dahl. "Approximations to multiple Coulomb scattering". In: *Nuclear Instruments and Methods in Physics Research Section B: Beam Interactions with Materials and Atoms* 58.1 (1991), pp. 6–10. DOI: 10.1016/0168-583X(91)95671-Y.

[21] Cécile Bopp. "The proton as a dosimetric and diagnostic probe". PhD thesis. Université de Strasbourg, 2014.

[22] CT Quiñones, JM Létang, and S Rit. "Filtered back-projection reconstruction for attenuation proton CT along most likely paths". In: *Physics in Medicine & Biology* 61.9 (2016), p. 3258. DOI: 10.1088/0031-9155/61/9/3258.

[23] Thomas Bortfeld. "An analytical approximation of the Bragg curve for therapeutic proton beams". In: *Medical physics* 24.12 (1997), pp. 2024–2033. DOI: 10.1118/1.598116.

[24] William Donahue, Wayne D Newhauser, and James F Ziegler. "Analytical model for ion stopping power and range in the therapeutic energy interval for beams of hydrogen and heavier ions". In: *Physics in Medicine & Biology* 61.17 (2016), p. 6570. DOI: 10.1088/0031-9155/61/17/6570.

[25] Waldemar Ulmer and Evangelos Matsinos. "Theoretical methods for the calculation of Bragg curves and 3D distributions of proton beams". In: *The European Physical Journal Special Topics* 190.1 (2010), pp. 1–81. DOI: 10.1140/epjst/e2010-01335-7.

[26] William Henry Bragg and Richard Kleeman. "XXXIX. On the $\alpha$ particles of radium, and their loss of range in passing through various atoms and molecules". In: *The London, Edinburgh, and Dublin Philosophical Magazine and Journal of Science* 10.57 (1905), pp. 318–340.

[27] Rui Zhang et al. "Water equivalent thickness values of materials used in beams of protons, helium, carbon and iron ions". In: *Physics in Medicine & Biology* 55.9 (2010), p. 2481. DOI: 10.1088/0031-9155/55/9/004.

[28] Niels Bohr. "LX. On the decrease of velocity of swiftly moving electrified particles in passing through matter". In: *The London, Edinburgh, and Dublin Philosophical Magazine and Journal of Science* 30.178 (1915), pp. 581–612. DOI: 10.1080/14786441008635432.

[29] PV Vavilov. "Ionization losses of high-energy heavy particles". In: *Soviet Phys. JETP* 5 (1957).

[30] Lev Davidovich Landau. "On the energy loss of fast particles by ionization". In: *J. Phys.* 8 (1944), pp. 201–205.

[31] Sébastien Jan et al. "GATE: a simulation toolkit for PET and SPECT". In: *Physics in Medicine & Biology* 49.19 (2004), p. 4543. DOI: 10.1088/0031-9155/49/19/007.

[32] World Health Organization. *Cancer Key Facts*. https://www.who.int/news-room/fact-sheets/detail/cancer. [Online; accessed 14-April-2022]. 2022.

[33] Ferlay J, Ervik M, Lam F, Colombet M, Mery L, Piñeros M, et al. *Global Cancer Observatory: Cancer Today*. https://gco.iarc.fr/today. [Online; accessed 14-April-2022]. 2020.

[34] Hyuna Sung et al. "Global cancer statistics 2020: GLOBOCAN estimates of incidence and mortality worldwide for 36 cancers in 185 countries". In: *CA: a cancer journal for clinicians* 71.3 (2021), pp. 209–249. DOI: 10.3322/caac.21660.

[35] Marco Durante and Harald Paganetti. "Nuclear physics in particle therapy: a review". In: *Reports on Progress in Physics* 79.9 (2016), p. 096702. DOI: 10.1088/0034-4885/79/9/096702.

[36] PTCOG. *Patient Statistics*. https://www.ptcog.ch/index.php/ptcog-patient-statistics. [Online; accessed 14-April-2022]. 2022.

[37] Hans-Peter Wieser et al. "Development of the open-source dose calculation and optimization toolkit matRad". In: *Medical physics* 44.6 (2017), pp. 2556–2568. DOI: 10.1002/mp.12251.

[38] PTCOG. *Facilities in Operation*. https://www.ptcog.ch/index.php/facilities-in-operation. [Online; accessed 14-April-2022]. 2022.

[39] QGIS Development Team. *QGIS Geographic Information System*. QGIS Association. 2022. URL: https://www.qgis.org.

[40] Markus Stock et al. "The technological basis for adaptive ion beam therapy at MedAustron: status and outlook". In: *Zeitschrift für Medizinische Physik* 28.3 (2018), pp. 196–210. DOI: 10.1016/j.zemedi.2017.09.007.

[41] L Grevillot, M Stock, and S Vatnitsky. "Evaluation of beam delivery and ripple filter design for non-isocentric proton and carbon ion therapy". In: *Physics in Medicine & Biology* 60.20 (2015), p. 7985. DOI: 10.1088/0031-9155/60/20/7985.

[42] Harald Paganetti. "Proton relative biological effectiveness–uncertainties and opportunities". In: *International journal of particle therapy* 5.1 (2018), pp. 2–14. DOI: 10.14338/IJPT-18-00011.1.

[43] WK Weyrather and G Kraft. "RBE of carbon ions: experimental data and the strategy of RBE calculation for treatment planning". In: *Radiotherapy and Oncology* 73 (2004), S161–S169. DOI: 10.1016/S0167-8140(04)80041-0.

[44] Daniel Habermehl et al. "The relative biological effectiveness for carbon and oxygen ion beams using the raster-scanning technique in hepatocellular carcinoma cell lines". In: *PLoS One* 9.12 (2014), e113591. DOI: 10.1371/journal.pone.0113591.

[45] Hermann Fuchs. "Development and Validation of Helium Ion Beam Dose Calculation". PhD thesis. Medical University of Vienna, 2014.

[46] Harald Paganetti et al. "Relative biological effectiveness (RBE) values for proton beam therapy". In: *International Journal of Radiation Oncology* Biology* Physics* 53.2 (2002), pp. 407–421. DOI: 10.1016/s0360-3016(02)02754-2.

[47] AF Resch et al. "Quantification of the uncertainties of a biological model and their impact on variable RBE proton treatment plan optimization". In: *Physica Medica* 36 (2017), pp. 91–102. DOI: 0.1016/j.ejmp.2017.03.013.

[48] *Absorbed Dose Determination in External Beam Radiotherapy*. Technical Reports Series 398. Vienna: INTERNATIONAL ATOMIC ENERGY AGENCY, 2001. ISBN: 92-0-102200-X. URL: https://www.iaea.org/publications/5954/absorbed-dose-determination-in-external-beam-radiotherapy.

[49] Rui Zhang and Wayne D Newhauser. "Calculation of water equivalent thickness of materials of arbitrary density, elemental composition and thickness in proton beam irradiation". In: *Physics in Medicine & Biology* 54.6 (2009), p. 1383. DOI: 10.1088/0031-9155/54/6/001.

[50] Wolfgang Birkfellner. *Applied medical image processing: a basic course*. CRC Press, 2016.

[51] M Yang et al. "Comprehensive analysis of proton range uncertainties related to patient stopping-power-ratio estimation using the stoichiometric calibration". In: *Physics in Medicine & Biology* 57.13 (2012), pp. 4095–4115. DOI: 10.1088/0031-9155/57/13/4095.

[52] DC Williams. "The most likely path of an energetic charged particle through a uniform medium". In: *Physics in Medicine & Biology* 49.13 (2004), p. 2899. DOI: 10.1088/0031-9155/49/13/010.

[53] RW Schulte et al. "A maximum likelihood proton path formalism for application in proton computed tomography". In: *Medical physics* 35.11 (2008), pp. 4849–4856. DOI: 10.1118/1.2986139.

[54] Nils Krah, Jean-Michel Létang, and Simon Rit. "Polynomial modelling of proton trajectories in homogeneous media for fast most likely path estimation and trajectory simulation". In: *Physics in Medicine & Biology* 64.19 (2019), p. 195014. DOI: 10.1088/1361-6560/ab3d0b.

[55] Charles-Antoine Collins-Fekete et al. "A theoretical framework to predict the most likely ion path in particle imaging". In: *Physics in Medicine & Biology* 62.5 (2017), p. 1777. DOI: 10.1088/1361-6560/aa58ce.

[56] Charles-Antoine Collins Fekete et al. "Developing a phenomenological model of the proton trajectory within a heterogeneous medium required for proton imaging". In: *Physics in Medicine & Biology* 60.13 (2015), p. 5071. DOI: 10.1088/0031-9155/60/13/5071.

[57] Dongxu Wang, T Rockwell Mackie, and Wolfgang A Tomé. "Bragg peak prediction from quantitative proton computed tomography using different path estimates". In: *Physics in Medicine & Biology* 56.3 (2011), p. 587. DOI: 10.1088/0031-9155/56/3/005.

[58] Stefanie Kaser et al. "Calculating $1/\beta 2p2$ for most likely path estimates for protons and helium ions using an analytical model". In: *Physica Medica* 89 (2021), pp. 169–175. DOI: 10.1016/j.ejmp.2021.08.002.

[59] Tianfang Li et al. "Reconstruction for proton computed tomography by tracing proton trajectories: A Monte Carlo study". In: *Medical physics* 33.3 (2006), pp. 699–706. DOI: 10.1118/1.2171507.

[60] Dongxu Wang, T Rockwell Mackie, and Wolfgang A Tomé. "On the use of a proton path probability map for proton computed tomography reconstruction". In: *Medical physics* 37.8 (2010), pp. 4138–4145. DOI: 10.1118/1.3453767.

[61] C Civinini et al. "Proton Computed Tomography: iterative image reconstruction and dose evaluation". In: *Journal of Instrumentation* 12.01 (2017), p. C01034. DOI: 10.1088/1748-0221/12/01/C01034.

[62] Ronald Newbold Bracewell and A. C. Riddle. "Inversion of fan-beam scans in radio astronomy". In: *The Astrophysical Journal* 150 (1967), p. 427.

[63] Lee A Feldkamp, Lloyd C Davis, and James W Kress. "Practical cone-beam algorithm". In: *Josa a* 1.6 (1984), pp. 612–619.

[64] GN Ramachandran and AV Lakshminarayanan. "Three-dimensional reconstruction from radiographs and electron micrographs: application of convolutions instead of Fourier transforms". In: *Proceedings of the National Academy of Sciences* 68.9 (1971), pp. 2236–2240. DOI: 10.1073/pnas.68.9.2236.

[65] Simon Rit et al. "Filtered backprojection proton CT reconstruction along most likely paths". In: *Medical physics* 40.3 (2013), p. 031103. DOI: 10.1118/1.4789589.

[66] G Poludniowski, NM Allinson, and PM Evans. "Proton computed tomography reconstruction using a backprojection-then-filtering approach". In: *Physics in Medicine & Biology* 59.24 (2014), p. 7905. DOI: 10.1088/0031-9155/59/24/7905.

[67] Scott Penfold and Yair Censor. "Techniques in iterative proton CT image reconstruction". In: *Sensing and Imaging* 16.1 (2015), pp. 1–21. DOI: 10.1007/s11220-015-0122-3.

[68] Ander Biguri et al. "TIGRE: a MATLAB-GPU toolbox for CBCT image reconstruction". In: *Biomedical Physics & Engineering Express* 2.5 (2016), p. 055010. DOI: 10.1088/2057-1976/2/5/055010.

[69] Lucas L Geyer et al. "State of the art: iterative CT reconstruction techniques". In: *Radiology* 276.2 (2015), pp. 339–357. DOI: https://doi.org/10.1148/radiol.2015132766.

[70] Junguo Bian et al. "Investigation of iterative image reconstruction in low-dose breast CT". In: *Physics in Medicine & Biology* 59.11 (2014), p. 2659. DOI: 10.1088/0031-9155/59/11/2659.

[71] Atul Padole et al. "CT radiation dose and iterative reconstruction techniques". In: *AJR Am J Roentgenol* 204.4 (2015), W384–W392. DOI: 10.2214/AJR.14.1324.

[72] Anders H Andersen and Avinash C Kak. "Simultaneous algebraic reconstruction technique (SART): a superior implementation of the ART algorithm". In: *Ultrasonic imaging* 6.1 (1984), pp. 81–94. DOI: 10.1016/0161-7346(84)90008-7.

[73] Ge Wang and Ming Jiang. "Ordered-subset simultaneous algebraic reconstruction techniques (OS-SART)". In: *Journal of X-ray Science and Technology* 12.3 (2004), pp. 169–177.

[74] Emil Y Sidky and Xiaochuan Pan. "Image reconstruction in circular cone-beam computed tomography by constrained, total-variation minimization". In: *Physics in Medicine & Biology* 53.17 (2008), p. 4777. DOI: 10.1088/0031-9155/53/17/021.

[75] Richard Gordon, Robert Bender, and Gabor T Herman. "Algebraic reconstruction techniques (ART) for three-dimensional electron microscopy and X-ray photography". In: *Journal of theoretical Biology* 29.3 (1970), pp. 471–481. DOI: 10.1016/0022-5193(70)90109-8.

[76] Kenneth M Hanson. "POPART-performance optimized algebraic reconstruction technique". In: *Visual Communications and Image Processing'88: Third in a Series*. Vol. 1001. International Society for Optics and Photonics. 1988, pp. 318–327.

[77] KM Hanson. "Optimization of the constrained Algebraic Reconstruction Technique for the performance of a variety of visual Tasks". In: *Progress in Clinical and Biological Research*. 1991.

[78] Jean Saudinos et al. "Nuclear scattering applied to radiography". In: *Physics in Medicine & Biology* 20.6 (1975), p. 890.

[79] J.C. Duchazeaubeneix et al. "Proton nuclear scattering radiography". In: *IEEE Transactions on Nuclear Science* NS-30.1 (1983).

[80] Hendrik Jansen and Paul Schütze. "Feasibility of track-based multiple scattering tomography". In: *Applied Physics Letters* 112.14 (2018), p. 144101. DOI: 10.1063/1.5005503.

[81] Tia Plautz et al. "200 MeV proton radiography studies with a hand phantom using a prototype proton CT scanner". In: *IEEE transactions on medical imaging* 33.4 (2014), pp. 875–881. DOI: 10.1109/TMI.2013.2297278.

[82] F Ulrich-Pur et al. "Imaging with protons at MedAustron". In: *NIM A* (2020), p. 164407. DOI: 10.1016/j.nima.2020.164407.

[83] S Kaser et al. "Different radiographic imaging modalities with a proton computed tomography demonstrator". In: *Journal of Instrumentation* 17.01 (2022), p. C01010. DOI: 10.1088/1748-0221/17/01/C01010.

[84] Nils Krah et al. "Scattering proton CT". In: *Physics in Medicine & Biology* 65.22 (2020), p. 225015. DOI: 10.1088/1361-6560/abbd18.

[85] Stefanie Kaser et al. "Measurements of proton beam attenuation radiographs at a clinical facility". In: *Nuclear Instruments and Methods in Physics Research Section A: Accelerators, Spectrometers, Detectors and Associated Equipment* (2022), p. 167069. DOI: 10.1016/j.nima.2022.167069.

[86] Dominik Dannheim et al. "Corryvreckan: a modular 4D track reconstruction and analysis software for test beam data". In: *JINST* 16.03 (2021), P03008. DOI: 10.1088/1748-0221/16/03/P03008.

[87] Leland Lavele Carter and Edmond Darrell Cashwell. *Particle-transport simulation with the Monte Carlo method*. Tech. rep. Los Alamos Scientific Lab., N. Mex.(USA), 1975. DOI: 10.2172/4167844.

[88] Sea Agostinelli et al. "GEANT4—a simulation toolkit". In: *Nuclear instruments and methods in physics research section A: Accelerators, Spectrometers, Detectors and Associated Equipment* 506.3 (2003), pp. 250–303. DOI: 10.1016/S0168-9002(03)01368-8.

[89] D Strulab et al. "GATE (Geant4 Application for Tomographic Emission): a PET/SPECT general-purpose simulation platform". In: *Nuclear Physics B-Proceedings Supplements* 125 (2003), pp. 75–79. DOI: 10.1016/S0920-5632(03)90969-8.

[90] Bruce Faddegon et al. "The TOPAS tool for particle simulation, a Monte Carlo simulation tool for physics, biology and clinical research". In: *Physica Medica* 72 (2020), pp. 114–121. DOI: 10.1016/j.ejmp.2020.03.019.

[91] Wilfried Schneider, Thomas Bortfeld, and Wolfgang Schlegel. "Correlation between CT numbers and tissue parameters needed for Monte Carlo simulations of clinical dose distributions". In: *Physics in Medicine & Biology* 45.2 (2000), p. 459. DOI: 10.1088/0031-9155/45/2/314.

[92] Rene Brun and Fons Rademakers. "ROOT—An object oriented data analysis framework". In: *Nuclear instruments and methods in physics research section A: accelerators, spectrometers, detectors and associated equipment* 389.1-2 (1997), pp. 81–86. DOI: 10.1016/S0168-9002(97)00048-X.

[93] René Brun et al. *ROOT User's Guide*. [Online; accessed 18-May-2022]. URL: https://root.cern.ch/root/htmldoc/guides/users-guide/ROOTUsersGuide.html.

[94] Wim Van Aarle et al. "The ASTRA Toolbox: A platform for advanced algorithm development in electron tomography". In: *Ultramicroscopy* 157 (2015), pp. 35–47. DOI: 10.1016/j.ultramic.2015.05.002.

[95] Stefan Van der Walt et al. "scikit-image: image processing in Python". In: *PeerJ* 2 (2014), e453. DOI: 10.7717/peerj.453.

[96] Kris Thielemans et al. "STIR: software for tomographic image reconstruction release 2". In: *Physics in Medicine & Biology* 57.4 (2012), p. 867. DOI: 10.1088/0031-9155/57/4/867.

[97] Simon Rit et al. "The Reconstruction Toolkit (RTK), an open-source cone-beam CT reconstruction toolkit based on the Insight Toolkit (ITK)". In: *Journal of Physics: Conference Series*. Vol. 489. 1. IOP Publishing. 2014, p. 012079. DOI: 10.1088/1742-6596/489/1/012079.

[98] Michael Schacht Hansen and Thomas Sangild Sørensen. "Gadgetron: an open source framework for medical image reconstruction". In: *Magnetic resonance in medicine* 69.6 (2013), pp. 1768–1776. DOI: 10.1002/mrm.24389.

[99] Simon Rit. *Proton CT reconstruction code*. https://github.com/SimonRit/PCT. [Online; accessed 23-May-2022].

[100] DC Hansen. *Proton CT reconstruction code*. https://github.com/dchansen/protonCT. [Online; accessed 23-May-2022].

[101] Blake Schultze. *Proton CT reconstruction code*. https://github.com/BlakeSchultze/pCT_Reconstruction. [Online; accessed 23-May-2022].

[102] Wei Qiu, David Titley-Péloquin, and Manuchehr Soleimani. "Blockwise conjugate gradient methods for image reconstruction in volumetric CT". In: *Computer methods and programs in biomedicine* 108.2 (2012), pp. 669–678. DOI: 10.1016/j.cmpb.2011.12.002.

[103] Ander Biguri. "Iterative reconstruction and motion compensation in computed tomography on GPUs". PhD thesis. University of Bath, 2018.

[104] *CUDA Toolkit Documentation*. [Online; accessed 19-May-2022]. URL: https://docs.nvidia.com/cuda/.

[105] *OpenCL*. [Online; accessed 19-May-2022]. URL: https://www.khronos.org/opencl/.

[106] Alexander Burker. "Ion Imaging at MedAustron". PhD thesis. TU Wien, 2022.

[107] Felix Ulrich-Pur. "Advancing Ion Computed Tomography by Incorporating Time-Of-Flight and 4D Tracking". PhD thesis. TU Wien, 2022.

[108] Michael Benedikt and Albin Wrulich. "MedAustron—Project overview and status". In: *The European Physical Journal Plus* 126.7 (2011), pp. 1–11. DOI: 10.1140/epjp/i2011-11069-9.

[109] Felix Ulrich-Pur et al. "Commissioning of low particle flux for proton beams at MedAustron". In: *Nuclear Instruments and Methods in Physics Research Section A: Accelerators, Spectrometers, Detectors and Associated Equipment* 1010 (2021), p. 165570. DOI: 10.1016/j.nima.2021.165570.

[110] Michael Benedikt et al. *Overview of the MedAustron design and technology choices*. Tech. rep. 2010. URL: https://cds.cern.ch/record/1272158.

[111] PJ Bryant et al. *Proton-ion medical machine study (PIMMS), 2*. Tech. rep. 2000. URL: https://cds.cern.ch/record/449577.

[112] Alexander Burker et al. "Imaging with ion beams at MedAustron". In: *Nuclear Instruments and Methods in Physics Research Section A: Accelerators, Spectrometers, Detectors and Associated Equipment* 958 (2020), p. 162246. DOI: 10.1016/j.nima.2019.05.087.

[113] Felix Ulrich-Pur et al. "A proton computed tomography demonstrator for stopping power measurements". In: *arXiv preprint arXiv:2106.12890* (2021). Accepted in: IOP Conference Series.

[114] M Bucciantonio et al. "Development of a fast proton range radiography system for quality assurance in hadrontherapy". In: *Nuclear Instruments and Methods in Physics Research Section A: Accelerators, Spectrometers, Detectors and Associated Equipment* 732 (2013), pp. 564–567. DOI: 10.1016/j.nima.2013.05.110.

[115] Paolo Baesso, David Cussans, and Joel Goldstein. "The AIDA-2020 TLU: a flexible trigger logic unit for test beam facilities". In: *Journal of Instrumentation* 14.09 (2019), P09019. DOI: 10.1088/1748-0221/14/09/P09019.

[116] Particle data group: Atomic and Nuclear Properties of Materials. Accessed: 2021-08-09. URL: http://pdg.lbl.gov/2019/AtomicNuclearProperties/.

[117] FS Dietrich et al. "Proton reaction cross sections measured in the BNL/AGS E943 experiment". In: *Journal of Nuclear Science and Technology* 39.sup2 (2002), pp. 269–271. DOI: 10.1080/00223131.2002.10875091.

[118] Experimental Nuclear Reaction Data. *EXFOR*. Accessed: 2022-03-01. URL: https://www-nds.iaea.org/exfor.

[119] Gregory Michalak et al. "A comparison of relative proton stopping power measurements across patient size using dual-and single-energy CT". In: *Acta Oncologica* 56.11 (2017), pp. 1465–1471. DOI: 10.1080/0284186X.2017.1372625.

[120] Stefanie Kaser. "Geant4 simulations for ion CT image reconstruction". MA thesis. TU Wien, 2019.

[121] M. Bucciantonio et al. "Development of a fast proton range radiography system for quality assurance in hadrontherapy". In: *Nucl. Instr. and Meth. A* 732 (2013), pp. 564–567. ISSN: 0168-9002. DOI: 10.1016/j.nima.2013.05.110.

[122] Giuseppe Antonio Pablo Cirrone et al. "Monte Carlo evaluation of the Filtered Back Projection method for image reconstruction in proton computed tomography". In: *Nuclear Instruments and Methods in Physics Research Section A: Accelerators, Spectrometers, Detectors and Associated Equipment* 658.1 (2011), pp. 78–83. DOI: 10.1016/j.nima.2011.05.061.

[123] Stefanie Kaser et al. "First application of the GPU-based software framework TIGRE for proton CT image reconstruction". In: *Physica Medica* 84 (2021), pp. 56–64. DOI: 10.1016/j.ejmp.2021.03.006.

[124] Georg Schramm et al. "Proceedings of the 16th Virtual International Meeting on Fully 3D Image Reconstruction in Radiology and Nuclear Medicine". In: *arXiv preprint arXiv:2110.04143* (2021).

[125] The Phantom Laboratory. *Catphan 600® Manual*. Accessed: 2022-06-15. 2015. URL: \url{https://www.phantomlab.com/catphan-600}.

[126] Stefanie Kaser et al. "Extension of the open-source TIGRE toolbox for proton imaging". In: *Zeitschrift für Medizinische Physik* (2022). DOI: 10.1016/j.zemedi.2022.08.005.

[127] Valentina Giacometti et al. "Software platform for simulation of a prototype proton CT scanner". In: *Medical Physics* 44.3 (2017), pp. 1002–1016. DOI: https://doi.org/10.1002/mp.12107.

[128] MJ Berger et al. *Stopping-power and range tables for electrons, protons, and helium ions, NIST Standard Reference Database 124*. 2017. DOI: 10.18434/T4NC7P.

[129] Pauli Virtanen et al. "SciPy 1.0: fundamental algorithms for scientific computing in Python". In: *Nature methods* 17.3 (2020), pp. 261–272. DOI: 10.1038/s41592-019-0686-2.

[130] Joao Seco et al. "Characterizing the modulation transfer function (MTF) of proton/carbon radiography using Monte Carlo simulations". In: *Medical physics* 40.9 (2013), p. 091717. DOI: https://doi.org/10.1118/1.4819816.

[131] Marine Soret, Stephen L Bacharach, and Irene Buvat. "Partial-volume effect in PET tumor imaging". In: *Journal of nuclear medicine* 48.6 (2007), pp. 932–945. DOI: 10.2967/jnumed.106.035774.

[132] Charles-Antoine Collins-Fekete et al. "A maximum likelihood method for high resolution proton radiography/proton CT". In: *Physics in Medicine & Biology* 61.23 (2016), p. 8232. DOI: 10.1088/0031-9155/61/23/8232.

[133] Blake Schultze et al. "Performance of hull-detection algorithms for proton computed tomography reconstruction". In: *Contemporary Mathematics* 636 (2015), pp. 211–224. DOI: 10.1090/conm/636/12739.

[134] Blake Schultze et al. "Reconstructing highly accurate relative stopping powers in proton computed tomography". In: *2015 IEEE Nuclear Science Symposium and Medical Imaging Conference (NSS/MIC)*. IEEE. 2015, pp. 1–3. DOI: 10.1109/NSSMIC.2015.7582218.

[135] Benjamin Kirchmayer. "Performance improvements and analysis of image reconstruction techniques in proton computed tomography". MA thesis. Wien, 2021.

[136] Feriel Khellaf et al. "A comparison of direct reconstruction algorithms in proton computed tomography". In: *Physics in Medicine & Biology* 65.10 (2020), p. 105010. DOI: https://doi.org/10.1088/1361-6560/ab7d53.

[137] CIRS, Norfolk, VA, USA. *Phantom Patient for Stereotactic End-to-End Verification*. Accessed: 23.03.2022. 2022. URL: https://www.cirsinc.com/products/radiation-therapy/phantom-patient-for-stereotactic-end-to-end-verification/.

[138] Felix Ulrich-Pur et al. "Feasibility study of a proton CT system based on 4D-tracking and residual energy determination via time-of-flight". In: *Physics in Medicine & Biology* 67.9 (2022), p. 095005. DOI: 10.1088/1361-6560/ac628b.

[139] Sepideh Hatamikia et al. "Optimization for customized trajectories in cone beam computed tomography". In: *Medical Physics*. (2020). DOI: https://doi.org/10.1002/mp.14403.